University of Sussex

Experimental Techniques for Cold Chemistry and Molecular Spectroscopy in an Ion Trap

Kevin Thomas Sheridan

Submitted for the degree of Doctor of Philosophy

University of Sussex

December 2012

Declaration

I hereby declare that this thesis has not been and will not be submitted in whole or in part to another University for the award of any other degree.

Signature:

Kevin Thomas Sheridan

UNIVERSITY OF SUSSEX

Kevin Thomas Sheridan, Doctor of Philosophy

Experimental Techniques for Cold Chemistry and Molecular Spectroscopy in an Ion Trap

Summary

A range of experimental techniques for application in reaction studies between ionic and neutral atoms/molecules and high resolution spectroscopy experiments with sympathetically cooled molecular ions are presented.

A novel ion trap loading scheme using the photo-ionisation of atoms generated by the pulsed laser ablation of a solid calcium target has been characterised. We have identified the range of ablation laser fluences that must be used in order to produce a flux of neutral calcium atoms, which is a prerequisite for isotope selective ion trap loading.

Calcium ions are trapped and laser cooled in a linear radio-frequency ion trap. We have developed a spectroscopy scheme that allows the entire fluorescence spectrum of trapped ions to be rapidly collected with high precision while maintaining a low ion temperature and good ion localisation throughout interrogation. The scheme has been demonstrated by measuring the saturation intensity of the calcium ion $4S_{1/2} \rightarrow 4P_{1/2}$ transition.

We have developed a novel scheme to measure the secular motion of trapped ions and demonstrated the application of the technique to ion-neutral collision reaction experiments. Employing pulsed excitation and Doppler velocimetry, we have measured the centre-of-mass mode frequency of single ions as well as large ion crystals with a frequency precision better than 2×10^{-3} within an interrogation time on the order of seconds. This method has been used to measure the mass of ions and observe charge exchange collisions between trapped calcium isotopes. In particular, we have measured the $^{44}Ca^{+} + ^{40}Ca \rightarrow ^{40}Ca^{+} + ^{44}Ca$ reaction cross section and demonstrated the single-event resolution of the technique.

Finally, we have developed a novel all-optical broadband scheme for exciting, amplifying and measuring the secular motion of ions in the trap. Oscillation induced by optical excitation has been coherently amplified to control and measure the ion's secular motion. Requiring only a single interrogation laser, the ion's oscillation amplitude can be precisely controlled. The application of this technique to non-destructive spectroscopy of trapped molecular ions is discussed.

Acknowledgements

This thesis describes experimental work carried out in the laboratory of Matthias Keller between January 2010 and December 2012 at the University of Sussex. This work would not have been possible without the guidance and support provided by both Matthias Keller and Wolfgang Lange. Matthias has an unparalleled experimental skill and is a never-ending source of exciting ideas. Wolfgang was truly unique and gave limitless inspiration to everyone around him. I have been extremely lucky to have had such talented and generous mentors.

I am grateful for the contributions made to this work by the post-doctoral researchers and doctoral students of the Ion Trap Cavity QED and Molecular Physics Group. Peter Blythe, Anders Mortensen, Dan Crick, Lizzie Brama, Nic Seymour-Smith, Andrew Riley-Watson, Alex Wilson, Hiroki Takahashi, Fedja Orucevic, Valentina Ruseva, Jennifer Hide, Kari Härkönen, Carlos Delgado, Amy Gardner, Jack Morphew, Markus Vogt, Stephen Begley, William Groom, Ezra Kassa and Sahar Hejazi were excellent colleagues and friends who not only taught me everything I know about experimental physics but also made the lab a fun place to work. Special thanks is due to Alan Butler, whose expertise facilitated the success of countless experimental designs.

Finally, I am forever grateful to my family for always encouraging and supporting me. I would never have gotten here without Aurélia and her limitless support. When you're at my side I feel that I can accomplish anything!

Contents

Chapter 1

Introduction

The study of chemical reactions and molecular spectroscopy under precisely controlled conditions is an important and fascinating application of ion traps. Ion traps provide an ideal medium for studying cold chemical reactions and high resolution molecular spectroscopy since trapped ions can be highly localised, laser cooled to low temperatures and stored for extended durations [1, 2].

Cold chemical reaction experiments aim to create an environment where reactions occur at temperatures on the order of mK or lower. This temperature regime can be routinely achieved in ion trapping experiments. At low temperatures, quantum effects become influential in chemical reaction processes due to the long de Broglie wavelengths of the slowly moving particles [2]. Probing this regime provides an understanding of reaction processes at very low collision energies but also develops the fundamental understanding of chemical reactions occurring at the full range of reaction energies and temperatures [3, 4, 5, 6]. Low temperature ions are highly localised when confined in an ion trap and can be used as targets for collision reactions with beams of neutral atoms or molecules. The result of collision reaction experiments can be determined by observing any change in the composition of the ion crystal following each reaction. Typically, this involves measuring the change in mass of the ion crystal, or observing the altered spatial configuration of the trapped ions.

In addition to providing the low temperatures and good localisation necessary for cold collision reaction experiments, the long storage time of trapped ions enables molecular spectroscopy experiments with unprecedented accuracy [7, 8]. Spectroscopy of cold molecular ions is employed to test fundamental principles of physics [9, 10, 11, 12], search for the time variation of the fundamental constants of nature [13, 14, 15] and measure the electron electric dipole moment [16]. Destructive spectroscopic techniques, such as

resonance enhanced multi-photon dissociation, alter the composition of the trapped ion crystal which can be detected following the interrogation [17, 18, 19].

A powerful tool for studying cold molecular ions within ion traps is sympathetic cooling. Although advances have been made in the laser cooling of molecular ions [20, 21, 22], the lack of closed level schemes precludes the technique in most cases. However, the laser cooling of atomic ions is a well established technique [23, 24] and trapped molecular ions can be cooled through Coulomb interactions with laser cooled atomic ions. Upon achieving a sufficiently low temperature, a group of cooled atomic and molecular ions condenses into a crystal structure known as a 'Coulomb crystal' [25, 26, 27, 28]. Ions within the crystal can be individually probed with lasers or used as a highly localised target for collision reactions. Molecular ions, ranging from light diatomics [29, 30, 31] up to heavy biomolecular ions [32], have been trapped and sympathetically cooled alongside laser cooled atomic ions. A variety of chemical reactions have been efficiently studied using the sympathetic cooling technique [28, 33, 34, 35] and recent advances in the study of cold ion-neutral reactions [36, 2, 37, 38, 39] has underscored the importance of the technique.

Since the sympathetically cooled ions do not fluoresce, they manifest as 'dark' ions within the crystal and can therefore be distinguished as holes in the crystalline structure when viewed with a CCD camera. Some information about the charge-to-mass ratio of the dark ions can be ascertained from their location in the crystal with respect to the centre of the trapping potential [40, 30]. Another method for identifying dark ions within the crystal is by exploiting the relationship between the ion crystal COM-mode oscillation frequency and the average charge-to-mass ratio of the crystal. The ion's motional modes may be resonantly excited resulting in a modulation of the atomic ion fluorescence signal. By measuring the modulated fluorescence, the oscillation frequencies of the ion crystal can be determined [41, 42, 43, 44]. This has been performed by applying narrowband excitation to a two component ion crystal consisting of a single molecular ion and a single laser cooled atomic ion [45, 35]. Recent work has shown that probing with pulsed electric fields can yield high precision mass measurements of large ion crystals containing hundreds of ions without compromising the configuration of individual ions within the crystal [46]. Chapters 6 and 7 in this thesis describe the principle of this technique and its application to low-energy ion-neutral collision experiments.

Information about the internal or external state of the trapped sympathetically cooled ions can be obtained by mapping their state information onto the observable state of the laser cooled atomic ions. This concept has its roots in the field of quantum logic

spectroscopy [47, 48, 49, 50, 51]. The internal state of a molecular ion can be probed by an off-resonant laser, which drives the COM-mode motion of the ion crystal through a dipole force only if the state being probed is occupied [52]. This can be detected by measuring the fluorescence modulation of the atomic ion. If the duration of the molecular ion's exposure to the off-resonant probe laser is appropriately limited, the oscillatory motion of the ion crystal can be seeded without altering the internal state of the molecule. In effect, the internal state of the molecular ion can be measured non-destructively. Chapter 8 describes a technique for coherently amplifying small amplitude oscillations which are seeded by changes in the light pressure force on the ion [53]. This technique may be an essential component of a non-destructive molecular ion state readout scheme [52, 54] as discussed in chapter 9.

Throughout this thesis experimental techniques are presented that can be applied to the study of reactions between ionic and neutral atoms/molecules and high resolution molecular ion spectroscopy experiments. Chapter 2 covers the theoretical basics required to describe the trapping and laser cooling of atomic ions. Then, chapter 3 describes a novel ion trap loading technique using pulsed laser ablation [55]. The system is characterised and the ablation laser fluence range that must be used in order to produce a flux of ground-state neutral calcium atoms, which is a prerequisite of isotope selective ion trap loading, is identified. The high repeatability of the ion loading technique lends itself to applications in chemical reaction experiments where high experimental repetition rates are an asset. Chapter 4 gives the details of the experimental ion trap and the laser systems used for all ion trapping experiments throughout the remainder of the thesis. Chapter 5 introduces a spectroscopy scheme that allows the entire fluorescence spectrum of trapped ions to be rapidly collected with high precision while maintaining a low ion temperature and good ion localisation throughout interrogation. The scheme has been demonstrated by measuring the saturation intensity of the calcium ion $4S_{1/2} \rightarrow 4P_{1/2}$ transition. The experimental results have been used to characterise the scheme we employ to laser cool calcium ions. Chapter 6 describes a novel technique for measuring changes in the mass of multi-component trapped ion crystals with single particle precision and chapter 7 presents the application of the technique to the measurement of charge exchange reactions. Finally, chapter 8 presents a novel scheme for exciting, amplifying and measuring the secular motion of ions in the trap. The technique can be employed in a novel non-destructive molecular state detection scheme discussed in chapter 9.

The work presented in this thesis resulted in the following publications:

- K. Sheridan, W. Lange and M. Keller, **All optical ion generation for ion trap loading**, *Applied Physics B* 105, 755-761 (2011).
- Kevin Sheridan and Matthias Keller, **Weighing of trapped ion crystals and its applications**, *New Journal of Physics* 13, 123002 (2011).
- K. Sheridan, N. Seymour-Smith, A. Gardner and M. Keller, **All-optical broadband excitation of the motional state of trapped ions**, *European Physical Journal D* 66, 289 (2012).

Chapter 2

Trapping and cooling calcium ions

2.1 Linear Paul trap

Ion traps are a powerful experimental tool in atomic, molecular and optical physics allowing detailed exploration into the interactions between atoms and molecules at the single particle level. The unparalleled control and storage of ions provided by ion traps offers a medium for state-of-the-art experiments.

The ion trap that we employ is a linear rf Paul trap and resembles a quadrupole mass filter with the addition of an electrostatic confinement along the guide axis. In this section we will describe how the ion trap allows for the trapping and localisation of ions in free space for extended durations.

As a consequence of Earnshaw's theorm, it is not possible to confine a charged particle solely with static potentials. As a result, a time varying electric field must be employed. In our trap, ions are confined in the radial plane by a two-dimensional rf-quadrupole potential created by four blade shaped electrodes. An additional static potential is applied to confine the ions in the third spatial dimension. Fig. 2.1 shows a three-dimensional model of the trap electrodes used in the linear Paul trap. Ions are confined in the trapping region located between the electrodes. The rf-voltage

$$U(t) = \frac{1}{2}\mathrm{U_{rf}}\cos(\Omega_{\mathrm{rf}} \cdot t) \tag{2.1}$$

is applied to two diagonally opposed rf-electrodes, where Ω_{rf} is the frequency and $\mathrm{U_{rf}}$ is the amplitude. A rf-voltage -$U(t)$ is applied to the other two rf-electrodes. For the proper electrode geometry, this combination of voltages creates a two-dimensional quadrupole potential suitable for confining ions in the radial plane of the trap. The potential acts

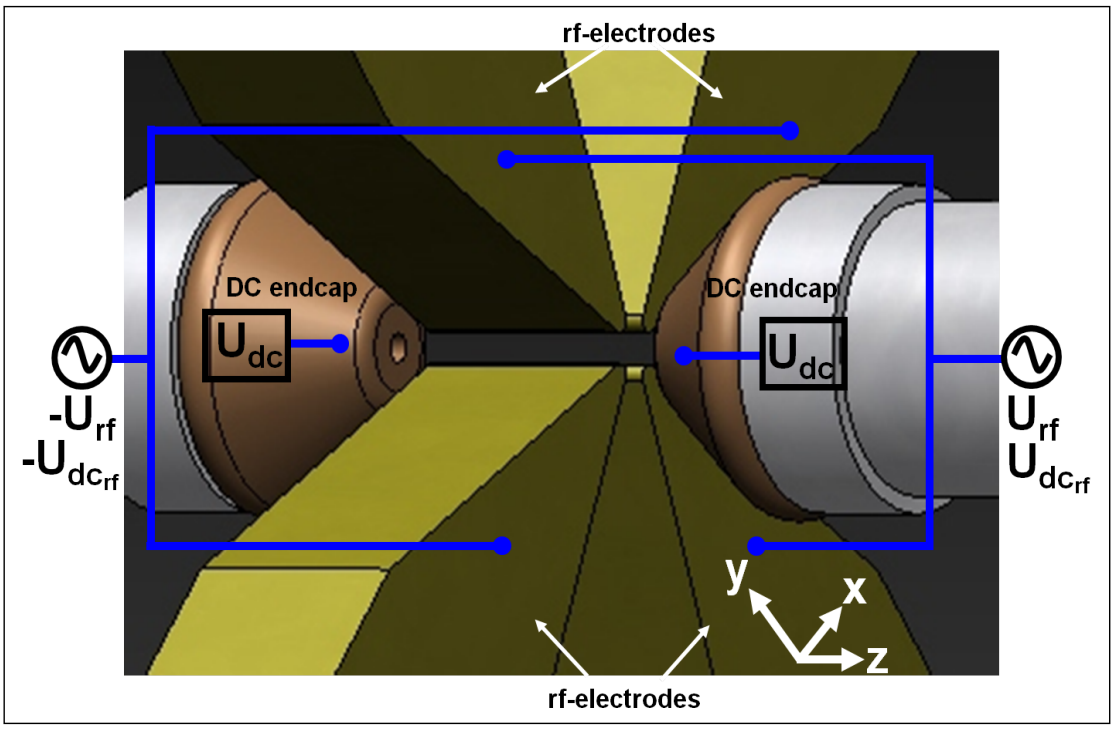

Figure 2.1: A three-dimensional model of the trap electrodes used in the linear Paul trap. The rf-voltage $U(t)$ and the DC voltage $\mathrm{U}_{\mathrm{dc_{rf}}}$ are applied to two diagonally opposed rf-electrodes and $-U(t)$ and $-\mathrm{U}_{\mathrm{dc_{rf}}}$ are applied to the other two rf-electroes. A two-dimensional rotating saddle potential confines the ion in the radial (x-y) plane of the trap. Ions are confined in the axial (z) direction by applying a static DC-voltage to the two endcap electrodes.

like a rotating saddle, which confines the ion along the x-direction during half a cycle and along the y-direction during the second half of the cycle. A dc-voltage U_{dc} is applied to the two endcap electrodes to confine the particle in the z-direction, referred to as the trap axis. The electric potential in the radial plane of the trap depends on the rf-voltages and the dc-voltages that are applied to the rf-electrodes:

$$\phi(x,y,t) = U(t)\eta\left(\frac{x^2-y^2}{r_0^2}\right) - \frac{1}{2}\eta \mathrm{U}_{\mathrm{dc_{rf}}}\left(\frac{x^2-y^2}{r_0^2}\right), \tag{2.2}$$

where r_0 is the distance from the trap centre to each rf-electrode, η is a constant that accounts for the geometry of the electrodes and $\mathrm{U}_{\mathrm{dc_{rf}}}$ is a DC voltage applied to the rf-electrodes. The equations of motion of the ion in the x and y-directions are:

$$\ddot{x} + \frac{Q}{m}\frac{\partial\phi(x,y,t)}{\partial x} = 0 \tag{2.3}$$

and

$$\ddot{y} + \frac{Q}{m}\frac{\partial\phi(x,y,t)}{\partial y} = 0, \tag{2.4}$$

where m is the mass of the ion and Q is the ion's electric charge. The equations of motion of the ion can be rewritten in the form of the Mathieu equation for the x and

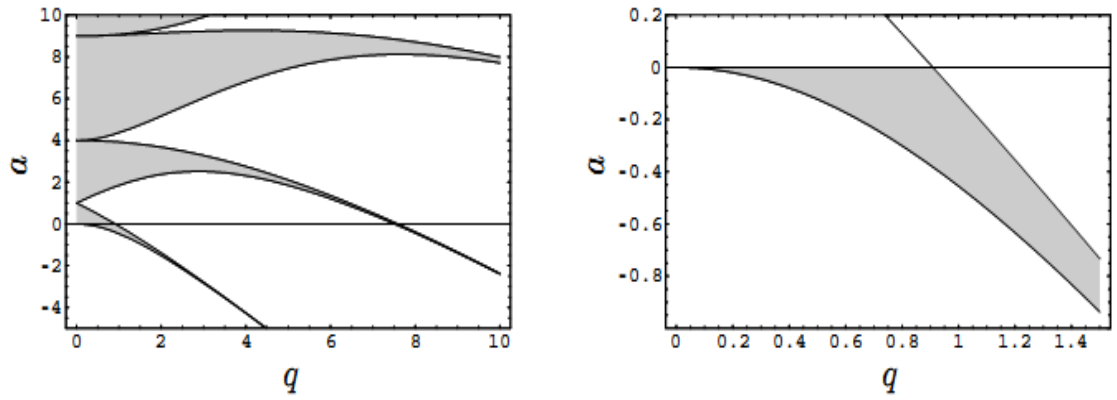

Figure 2.2: *Left*: Stable solutions to Equ. 2.5 and Equ. 2.6 are achieved for the grey shaded regions in q-a space. *Right*: The region of q-a space that gives stable trapping of ions in the linear Paul trap.

y-directions[56]:

$$\frac{d^2x}{d\tau^2} + (a - 2q\cos(2\tau))x = 0, \tag{2.5}$$

$$\frac{d^2y}{d\tau^2} + (a - 2q\cos(2\tau))y = 0, \tag{2.6}$$

where we have made the substitutions:

$$\tau = \frac{\Omega_{\mathrm{rf}}t}{2}, \;\; q = \frac{2Q\mathrm{U}_{\mathrm{rf}}}{m\Omega_{\mathrm{rf}}^2 r_0^2}, \;\; a = \frac{-4\eta Q\mathrm{U}_{\mathrm{dc_{rf}}}}{m\Omega_{\mathrm{rf}}^2 r_0^2}. \tag{2.7}$$

Stable solutions to Equ. 2.5 and Equ. 2.6 exist for a small range of q and a values. The region in q-a space that allows for stable trapping of an ion in the linear Paul trap is shown in Fig. 2.2. The stability conditions of the q and a parameters give a limit to the charge-to-mass ratio (Q/m) of a trappable ion. For small values of q and a the solutions to the Matthieu equation can be approximated by:

$$x(t) = x_0\,(1 - q\cos(\Omega_{\mathrm{rf}}\cdot t))\cos(\omega_{\mathrm{r}}\cdot t), \tag{2.8}$$

$$y(t) = y_0\,(1 - q\cos(\Omega_{\mathrm{rf}}\cdot t))\cos(\omega_{\mathrm{r}}\cdot t), \tag{2.9}$$

where the radial secular frequency has been introduced and is given by:

$$\omega_{\mathrm{r}} = \frac{\sqrt{q^2/2 \pm a}}{2}\Omega_{\mathrm{rf}}. \tag{2.10}$$

Equ. 2.8 and Equ. 2.9 describe the oscillation of the ion in the radial plane at two separate superimposed frequencies. The 'secular' motion is relatively slow with a frequency ω_{r}, which is linearly proportional to the rf-voltage U_{rf} for small values of the a parameter. The ion's 'micromotion' is a fast oscillation with frequency equal to the rf-drive frequency Ω_{rf}. Fig. 2.3 shows the ion's displacement during one cycle of the secular motion for a

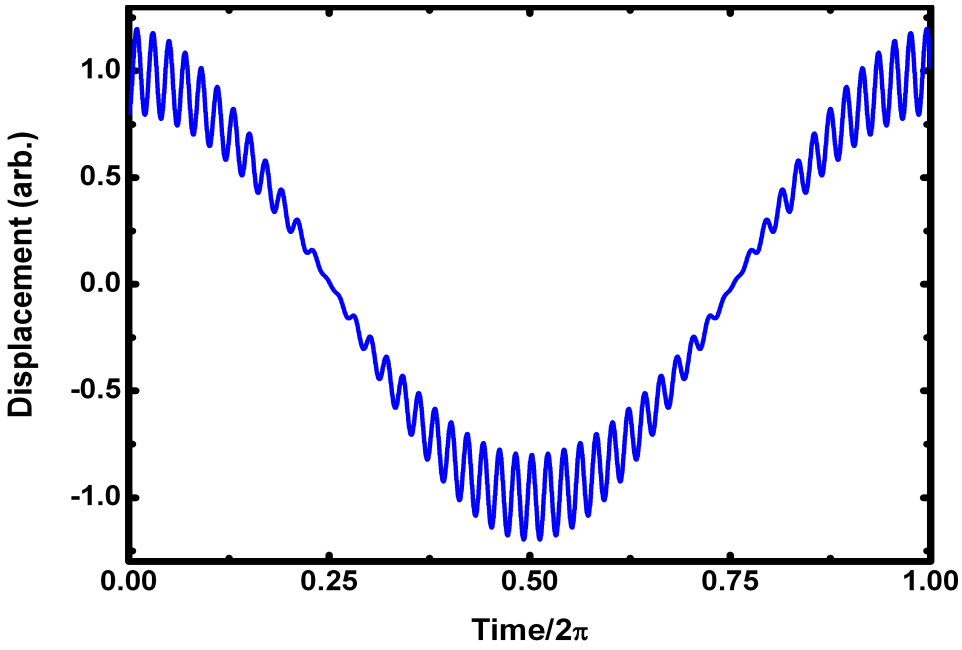

Figure 2.3: The ion's displacement from the trap centre during one cycle of the secular motion for a secular oscillation amplitude of 1, $q = 0.2$ and $\Omega_{\mathrm{rf}} = 50 \cdot \omega_{\mathrm{r}}$. The fast micromotion oscillations are superimposed onto the slow secular motion. The ion's micromotion amplitude is proportional to its displacement from the trap centre and can be minimised by localising the ion at the centre.

secular oscillation amplitude of 1, a q parameter of 0.2 and an rf-frequency of $50 \cdot \omega_{\mathrm{r}}$. The amplitude of the driven micromotion oscillations are proportional to the ion's displacement from the trap centre and to the magnitude of the rf-voltage, where $\mathrm{U_{rf}} \propto q$. It is clear from Fig. 2.3 that the ion's micromotion can be minimised by localising it at the centre of the rf-potential.

The static trapping potential created by applying the voltage $\mathrm{U_{dc}}$ to the endcap electrodes is given by:

$$\phi(x, y, z) = \eta \mathrm{U_{dc}} \frac{z^2}{z_0^2} - \frac{1}{2} \eta \mathrm{U_{dc}} \left(\frac{x^2 + y^2}{z_0^2} \right). \tag{2.11}$$

The equation of motion of the ion in the axial direction is

$$\ddot{z} + \frac{2\eta \mathrm{U_{dc}}}{z_0^2} \frac{Q}{m} z = 0, \tag{2.12}$$

where m is the mass of the ion and Q is the ion's electric charge. Equ. 2.12 describes simple harmonic motion with the ion's axial position evolving in time according to

$$z(t) = z_0 \cos(\omega_{\mathrm{z}} \cdot t), \tag{2.13}$$

where the axial secular frequency of the ion has been introduced and is given by

$$\omega_z = \sqrt{\frac{2\eta Q \mathrm{U_{dc}}}{m z_0^2}}. \tag{2.14}$$

The ion's axial secular frequency is proportional to both the square root of the voltage applied to the endcap electrodes U_{dc} and the square root of the ion's charge-to-mass ratio.

By averaging out the high frequency micromotion from Equ. 2.8 and Equ. 2.9 we can approximate the ion as a three-dimensional harmonic oscillator confined within a 'pseudo-potential' well with the form:

$$\phi(x,y,z) = \frac{1}{2}(\omega_r'^2 x^2 + \omega_r'^2 y^2 + \omega_z^2 z^2), \tag{2.15}$$

where

$$\omega_r' = \sqrt{\omega_r^2 - \frac{\eta Q U_{dc}}{2mz_0^2}}. \tag{2.16}$$

In this approximation, the ion's three-dimensional motion in the trap can be described by a set of simple equations:

$$x(t) = x_0 \cos(\omega_r' \cdot t), \tag{2.17}$$

$$y(t) = y_0 \cos(\omega_r' \cdot t), \tag{2.18}$$

$$z(t) = z_0 \cos(\omega_z \cdot t). \tag{2.19}$$

2.2 Atom-light interactions

Calcium ions trapped in the potential described in Sec. 2.1 can be further localised and cooled through their interaction with Doppler cooling lasers. Furthermore, we can manipulate the secular motion of the ion with the Doppler cooling lasers. By collecting the ion's fluorescence during interrogation, the ion's oscillation frequency and therefore its charge-to-mass ratio can be precisely determined. In order to properly describe these measurements, it is necessary to firstly characterise the interaction of the atomic system with the laser field. After developing a two-level model of atom-light interaction, the calcium three-level system is discussed. This is followed by a discussion of an alternative level scheme involving five levels. Then, the laser forces on the ion are introduced and Doppler cooling is defined. Finally, the use of Doppler velocimetry to map the ion's oscillatory motion onto its fluorescence is described.

2.2.1 Two-level system

We firstly consider a model consisting of a closed two-level atomic system interacting with a single laser as shown by the level diagram in Fig. 2.4. Although a closed two-level system does not exist in the calcium ion, this model will provide results which are essential for

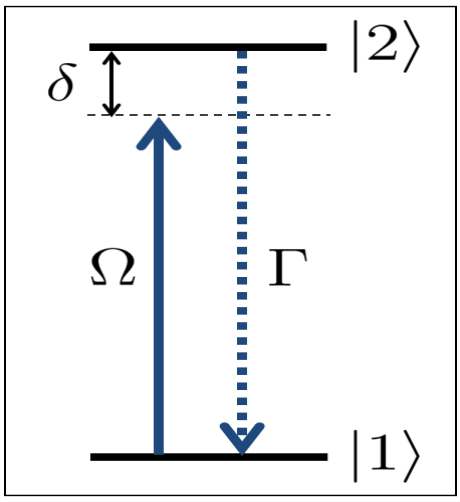

Figure 2.4: A two-level atomic system consisting of ground state $|1\rangle$ and excited state $|2\rangle$ interacting with a classical electromagnetic wave detuned from resonance by δ. Ω is the Rabi frequency of the dipole transition $|1\rangle \rightarrow |2\rangle$ (solid arrow) and Γ is the spontaneous decay rate of the excited state (dashed arrow).

understanding realistic and more complicated schemes. The laser is approximated by a classical monochromatic electromagnetic wave and the system is described by the density matrix:

$$\rho = \begin{bmatrix} |C_1|^2 & C_1 C_2^* \\ C_2 C_1^* & |C_2|^2 \end{bmatrix}, \tag{2.20}$$

where the diagonal elements $|C_n|^2$ describe the populations of the ground ($n = 1$) and excited ($n = 2$) atomic energy states and the off-diagonal elements are the coherence terms. The time evolution of each element in the density matrix describes the time evolution of the system. This can be expressed by

$$\frac{d\rho(t)}{dt} = \frac{i}{\hbar}\left[\rho(t), \hat{H}\right], \tag{2.21}$$

where

$$\hat{H} = \hat{H}_A + \hat{H}_I \tag{2.22}$$

is the Hamiltonian of the system formed by the Hamiltonian of the non-interacting atom ($\hat{H_A}$) and the interaction between the atom and the radiation field ($\hat{H_I}$). The interaction Hamiltonian is given by

$$\hat{H}_I = -\vec{\mu}_{12} \cdot \vec{E}, \tag{2.23}$$

where $\vec{\mu}_{12}$ is the transition dipole matrix element of the two-level atomic system and the laser field is a classical electromagnetic wave.

To account for the effects of spontaneous emission in the system, we need to include an additional term in Equ. 2.21 to describe the decay. The time evolution of the density

matrix is then given by the master equation:

$$\frac{d\rho(t)}{dt} = \frac{i}{\hbar}\left[\rho(t), \hat{H}\right] + \Lambda\rho, \tag{2.24}$$

where

$$\Lambda\rho = -\frac{\Gamma}{2}\Big[\sigma_+\sigma_-\rho - 2\sigma_-\rho\sigma_+ + \rho\sigma_+\sigma_-\Big], \tag{2.25}$$

Γ is the spontaneous decay rate and σ_+ and σ_- are the atomic raising and lowering operators. The time evolution of each element of the density matrix for the system, including spontaneous emission, is given by the optical Bloch equations:

$$\begin{aligned}
\frac{d}{dt}\rho_{22} &= -i\frac{\Omega}{2}e^{-i\delta t}\rho_{12} + i\frac{\Omega}{2}e^{i\delta t}\rho_{21} - \Gamma\rho_{22} = -\frac{d}{dt}\rho_{11}, &(2.26)\\
\frac{d}{dt}\rho_{21} &= -i\frac{\Omega}{2}e^{-i\delta t}(\rho_{11} - \rho_{22}) - \frac{\Gamma}{2}\rho_{21} = \frac{d}{dt}\rho^*_{12}, &(2.27)
\end{aligned}$$

where $\delta = \omega_l - \omega_{12}$ is the detuning of the interaction laser and $\Omega = (\vec{\mu}_{12}\cdot\vec{E_0})/\hbar$ is the Rabi frequency [57, 58, 59]. These equations are simplified by making the substitutions $\tilde{\rho}_{12} = \rho_{12}e^{-i\delta t}$ and $\tilde{\rho}_{21} = \rho_{21}e^{i\delta t}$ to give:

$$\begin{aligned}
\frac{d}{dt}\rho_{22} &= -i\frac{\Omega}{2}\tilde{\rho}_{12} + i\frac{\Omega}{2}\tilde{\rho}_{21} - \Gamma\rho_{22} = -\frac{d}{dt}\rho_{11}, &(2.28)\\
\frac{d}{dt}\tilde{\rho}_{21} &= i\frac{\Omega}{2}(\rho_{11} - \rho_{22}) - \frac{\Gamma}{2}\tilde{\rho}_{12} - i\delta\tilde{\rho}_{12} = \frac{d}{dt}\tilde{\rho}^*_{12}. &(2.29)
\end{aligned}$$

Using conservation of population ($\rho_{11} + \rho_{22} = 1$) and the relation $\tilde{\rho}_{12} = \tilde{\rho}^*_{21}$, the excited state population in the steady state (where $\frac{d}{dt}\rho \to 0$) can be expressed by

$$\rho_{22} = \frac{s/2}{1 + s + (2\delta/\Gamma)^2}, \tag{2.30}$$

where the saturation parameter $s = 2\Omega^2/\Gamma^2$ has been introduced. The saturation parameter can also be defined in terms of the interaction laser intensity I by

$$s = I/I_{\text{sat}}, \tag{2.31}$$

where

$$I_{\text{sat}} = \frac{2\pi hc\Gamma}{\lambda^3} \tag{2.32}$$

is the saturation intensity of the transition [60, 61]. Fig. 2.5 shows the excited state population as a function of the laser detuning for three values of s. According to Equ. 2.30, the fluorescence spectrum of the atom is a Lorentzian function. For an on-resonance interaction laser ($\delta = 0$), the excited state population reaches its peak value of $s/(2+2s)$. For an intense interaction laser ($s \gg 1$), the excited state population saturates to 1/2.

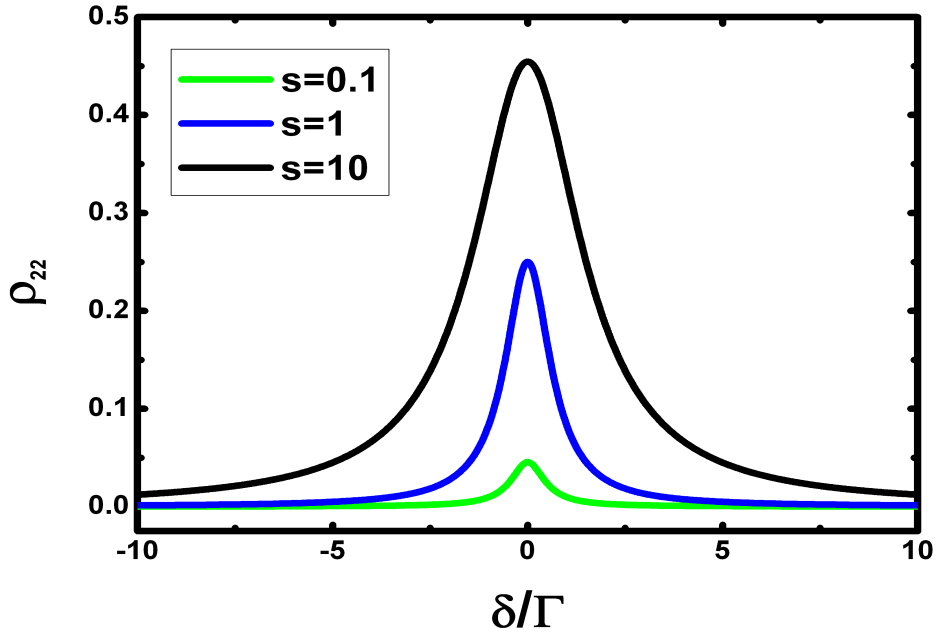

Figure 2.5: The excited state population of the two-level system (Equ. 2.30) is plotted as a function of the laser detuning for three values of the saturation parameter s. As s is increased, the excited state population approaches a maximum value of 1/2.

The scattering rate of the atom in the laser field is given by the product of the excited state population and the spontaneous decay rate:

$$\gamma_{\text{scatt}} = \Gamma \cdot \rho_{22} = \frac{s\Gamma/2}{1+s+(2\delta/\Gamma)^2} = \left(\frac{s}{1+s}\right)\frac{\Gamma/2}{1+(2\delta/\Gamma')^2}, \tag{2.33}$$

where

$$\Gamma' = \Gamma\sqrt{1+s} \tag{2.34}$$

is the power broadened linewidth of the atom. Therefore, as the interaction laser intensity is increased, the effective width of the spectral line (Γ') increases. In addition, for $s \gg 1$ the scattering rate saturates to a value of $\Gamma/2$.

2.2.2 Three-level calcium system

The two-level atom-light interaction model can be expanded by adding an additional atomic energy state and an additional laser to the system. The resulting three-level system can be used to describe a commonly implemented scheme for Doppler cooling calcium ions. Fig. 2.6 shows the calcium Λ-system, which consists of three atomic energy states. The $4S_{1/2} \rightarrow 4P_{1/2}$ transition is addressed by the Doppler cooling laser at 397 nm with detuning $\delta_D = \omega_{SP} - \omega_D$, where ω_D is the angular frequency of the laser and ω_{SP} is the frequency of the transition. The $4P_{1/2}$ upper cooling state rapidly decays to the

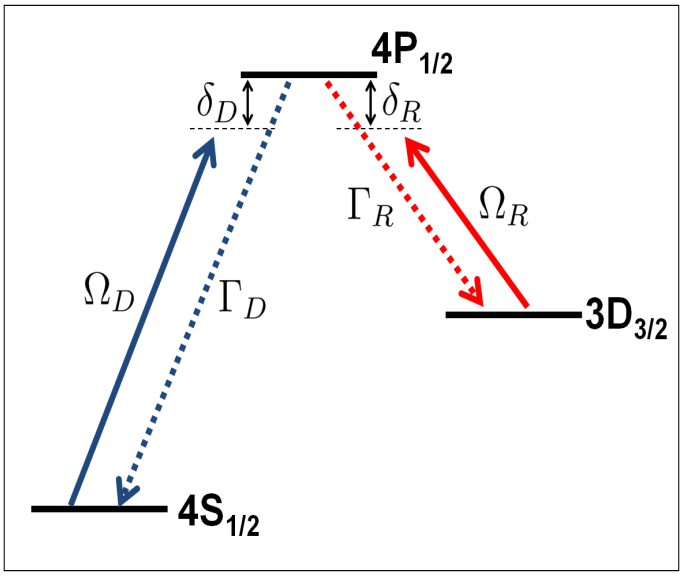

Figure 2.6: The calcium ion Λ-system consisting of the $4S_{1/2}$ ground state, $4P_{1/2}$ excited state and meta-stable $3D_{3/2}$-state interacting with a pair of lasers. The Doppler cooling laser at 397 nm addresses the $4S_{1/2}\rightarrow 4P_{1/2}$ transition with detuning δ_D and the re-pump laser at 866 nm addresses the $3D_{3/2}\rightarrow 4P_{1/2}$ transition with detuning δ_R. The excited state decays to both the $4S_{1/2}$-state and the $3D_{3/2}$-state at rates Γ_D and Γ_R respectively. The lifetime of the $3D_{3/2}$-state is much longer than that of the $4P_{1/2}$-state, therefore spontaneous decay from the $3D_{3/2}$-state is neglected.

$4S_{1/2}$-state at a rate of approximately $\Gamma_D = 2\pi \times 21$ MHz. However, there is a 1/16 chance per cycle of the $4P_{1/2}$-state decaying through spontaneous emission to the metastable $3D_{3/2}$-state [62]. In order to avoid trapping population in the $3D_{3/2}$-state, a re-pump laser must be employed. The re-pump laser at 866 nm addresses the $3D_{3/2}\rightarrow 4P_{1/2}$ transition with a detuning $\delta_R = \omega_{DP} - \omega_R$.

Modeling the lasers as classical electromagnetic waves, the Hamiltonian of the Λ-system can be expressed as

$$\hat{H} = \hat{H}_A + \hat{H}_D + \hat{H}_R, \tag{2.35}$$

where

$$\hat{H}_D = -\vec{\mu}_{SP} \cdot \vec{E}_D \tag{2.36}$$

and

$$\hat{H}_R = -\vec{\mu}_{DP} \cdot \vec{E}_R \tag{2.37}$$

describe the interaction of each laser with the ion. There are five independent equations

for the time evolution of the density matrix describing the system, and these are given by:

$$\frac{d}{dt}\rho_{11} = i\frac{\Omega_D}{2}(\tilde{\rho}_{13} - \tilde{\rho}_{31}) + \Gamma_D \cdot \rho_{33}, \tag{2.38}$$

$$\frac{d}{dt}\rho_{22} = i\frac{\Omega_R}{2}(\tilde{\rho}_{23} - \tilde{\rho}_{32}) + \Gamma_R \cdot \rho_{33}, \tag{2.39}$$

$$\frac{d}{dt}\tilde{\rho}_{12} = i\left[(\delta_R - \delta_D)\tilde{\rho}_{12} + \frac{\Omega_R}{2}\tilde{\rho}_{13} - \frac{\Omega_D}{2}\tilde{\rho}_{32}\right], \tag{2.40}$$

$$\frac{d}{dt}\tilde{\rho}_{13} = i\left[\frac{\Omega_D}{2}(\rho_{11} - \rho_{33}) + \frac{\Omega_R}{2}\tilde{\rho}_{12} - \delta_D \cdot \tilde{\rho}_{13}\right] - \frac{\Gamma_D + \Gamma_R}{2}\tilde{\rho}_{13}, \tag{2.41}$$

$$\frac{d}{dt}\tilde{\rho}_{23} = i\left[\frac{\Omega_R}{2}(\rho_{22} - \rho_{33}) + \frac{\Omega_D}{2}\tilde{\rho}_{21} - \delta_R \cdot \tilde{\rho}_{23}\right] - \frac{\Gamma_D + \Gamma_R}{2}\tilde{\rho}_{23}, \tag{2.42}$$

$$\tag{2.43}$$

where $\Omega_D = (\vec{\mu}_{SP} \cdot \vec{E}_D)/\hbar$ and $\Omega_R = (\vec{\mu}_{DP} \cdot \vec{E}_R)/\hbar$ are the Rabi frequencies of the $4S_{1/2} \rightarrow 4P_{1/2}$ and $3D_{3/2} \rightarrow 4P_{1/2}$ dipole transitions [63, 64]. The steady-state solution for the population of the excited state is [63]

$$\rho_{33} = \frac{4(\delta_D - \delta_R)^2\Omega_D^2\Omega_R^2(\Gamma_D + \Gamma_R)}{Z}, \tag{2.44}$$

where

$$\begin{aligned} Z = {} & 8(\delta_D - \delta_R)^2\Omega_D^2\Omega_R^2(\Gamma_D + \Gamma_R) + 4(\delta_D - \delta_R)^2(\Gamma_D + \Gamma_R)^2(\Omega_D^2\Gamma_R + \Omega_R^2\Gamma_D) \\ & + 16(\delta_D - \delta_R)^2(\delta_D^2\Omega_R^2\Gamma_D + \delta_R^2\Omega_D^2\Gamma_R) \\ & - 8\delta_D(\delta_D - \delta_R)\Omega_R^4\Gamma_D + 8\delta_R(\delta_D - \delta_R)\Omega_D^4\Gamma_R \\ & + (\Omega_D^2 + \Omega_R^2)^2(\Omega_D^2\Gamma_R + \Omega_R^2\Gamma_D). \end{aligned} \tag{2.45}$$

The excited state population is plotted in Fig. 2.7 as a function of the 397 nm laser detuning for on-resonance re-pumping ($\delta_R = 0$) and fixed laser powers. At the centre of the spectrum the excited state population drops to zero. This is due to the coherent trapping of population in a superposition of the $4S_{1/2}$ and $3D_{3/2}$ states and occurs when $\delta_D = \delta_R$. This 'dark' state, when the rate of atomic fluorescence drops to zero, is a characteristic feature of the closed three-level system and presents complications in the context of laser cooling where a stable scattering rate is required.

We have plotted the excited state population as a function of both the Doppler cooling laser saturation parameter and the re-pump laser saturation parameter, where $s = 2\Omega^2/\Gamma^2$. The result is shown in Fig. 2.8. In contrast to the two-level system, the exited state population does not saturate as the Doppler cooling laser power is increased. Instead, it decreases and likewise the photon scattering rate decreases. Moreover, the maximum excited state population is significantly lower than in the two-level system. It would

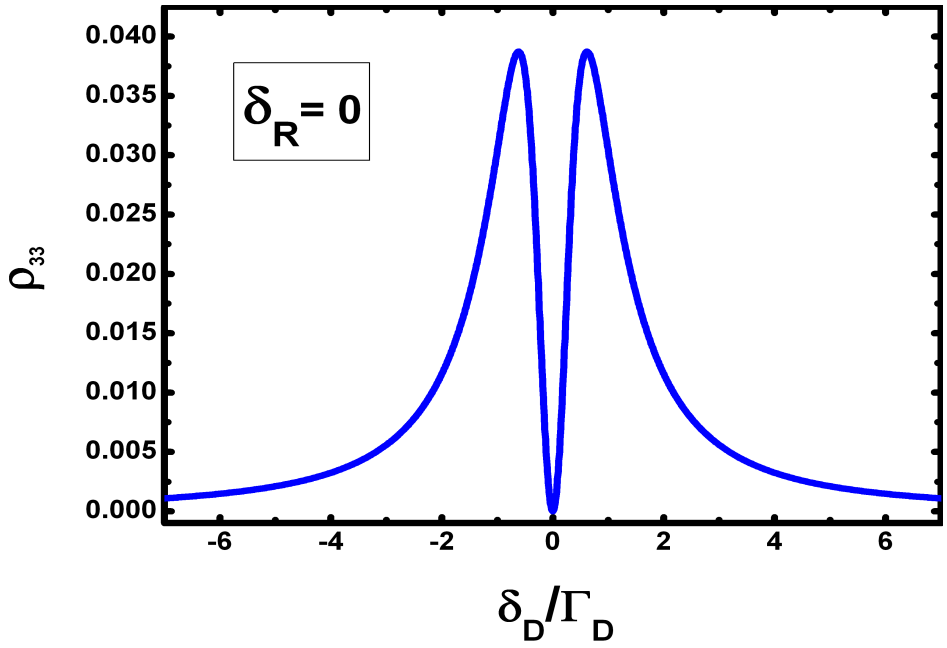

Figure 2.7: The excited state population of the calcium ion Λ-system (Equ. 2.44) is plotted as a function of the Doppler cooling laser detuning for an on-resonance re-pump laser ($\delta_R = 0$).

be advantageous to modify this scheme so that a larger excited state population can be achieved. As a result, the scattering rate would be larger and the Doppler cooling efficiency would be improved.

2.2.3 Five-level calcium system

In order to improve Doppler cooling efficiency, we implement a cooling scheme that better approximates the ideal two-level system and avoids the effects of coherent population trapping that are characteristic of the Λ-system [62, 66]. The cooling scheme is shown by the level diagram in Fig. 2.9. In this scheme, the ion is re-pumped out of the $3D_{3/2}$-state by applying a laser on the $3D_{3/2} \rightarrow 4P_{3/2}$ transition at 850 nm. The population is subsequently returned to the ground state through the decay of the $4P_{3/2}$-state, at a rate of approximately $2\pi \times 21.5$ MHz. In this way, the $4S_{1/2}$-state is decoupled from the $3D_{3/2}$-state and coherent population trapping is avoided. As with the $4P_{1/2}$-state, the $4P_{3/2}$-state has a decay channel to the $3D_{3/2}$-state, occurring at a rate of approximately $2\pi \times 0.18$ MHz, but it also has an additional decay channel to the $3D_{5/2}$-state, which occurs at a rate of approximately $2\pi \times 1.56$ MHz. Therefore, another re-pump laser must be applied to the system to drive the $3D_{5/2} \rightarrow 4P_{3/2}$ transition at 854 nm. Coherent population trapping can still occur in this scheme, with population trapped in the superposition of the $3D_{3/2}$ and $3D_{5/2}$-states for $\delta_{850} = \delta_{854}$. We therefore require that $\delta_{850} \neq \delta_{854}$.

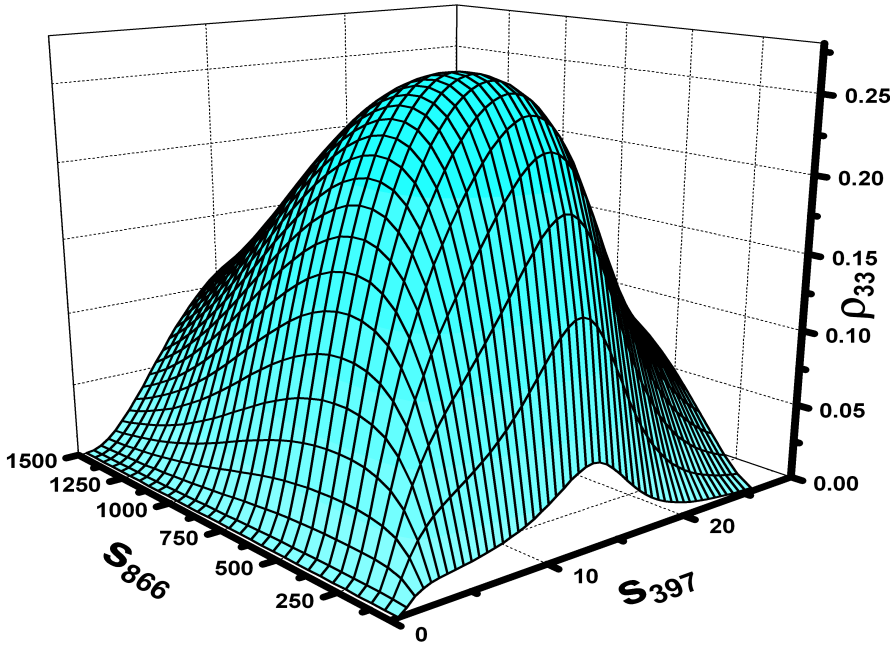

Figure 2.8: The population of the $4P_{1/2}$-state as a function of the Doppler cooling laser saturation parameter (s_{397}) and the re-pump laser saturation parameter (s_{866}). The 866 nm laser detuning is -20 MHz and the 397 nm laser detuning is -5 MHz.

Since we can ignore the effects of coherent population trapping, the system can be modelled using rate equations, which describe the time evolution of the population of each state in the system. In terms of the Einstein A and B coefficients, the rate equations can be expressed as

$$\frac{d}{dt}N_{S_1}(t) = A_{P_2S_1}N_{P_2}(t) + A_{P_1S_1}N_{P_1}(t) + B_{S_1P_1}\rho_{397}(\nu)\Big[N_{P_1}(t) - N_{S_1}(t)\Big], \tag{2.46}$$

$$\frac{d}{dt}N_{P_1}(t) = -A_{P_1S_1}N_{P_1}(t) - A_{P_1D_1}N_{P_1}(t) + B_{S_1P_1}\rho_{397}(\nu)\Big[N_{S_1}(t) - N_{P_1}(t)\Big], \tag{2.47}$$

$$\frac{d}{dt}N_{D_1}(t) = A_{P_1D_1}N_{P_1}(t) + A_{P_2D_1}N_{P_2}(t) + B_{D_1P_2}\rho_{850}(\nu)\Big[N_{P_2}(t) - N_{D_1}(t)\Big], \tag{2.48}$$

$$\frac{d}{dt}N_{D_2}(t) = A_{P_2D_2}N_{P_2}(t) + B_{D_2P_2}\rho_{854}(\nu)\Big[N_{P_2}(t) - N_{D_2}(t)\Big], \tag{2.49}$$

$$\begin{aligned}\frac{d}{dt}N_{P_2}(t) = &-A_{P_2S_1}N_{P_2}(t) - A_{P_2D_2}N_{P_2}(t) - A_{P_2D_1}N_{P_2}(t) \\ &+ B_{D_1P_2}\rho_{850}(\nu)\Big[N_{D_1}(t) - N_{P_2}(t)\Big] + B_{D_2P_2}\rho_{854}(\nu)\Big[N_{D_2}(t) - N_{P_2}(t)\Big],\end{aligned} \tag{2.50}$$

where A_{ij} is the Einstein A coefficient for spontaneous emission from state i to state j, B_{ij} is the Einstein B coefficient for absorption from state i to state j as well as stimulated emission from state j to state i and $\rho(\nu)$ is the spectral energy density of the laser field. The states are abreviated: $4S_{1/2} = S_1$, $3D_{3/2} = D_1$, $3D_{5/2} = D_2$, $4P_{1/2} = P_1$ and $4P_{3/2} = P_2$. In the steady state, and using the conservation of population, the population of the $4P_{1/2}$

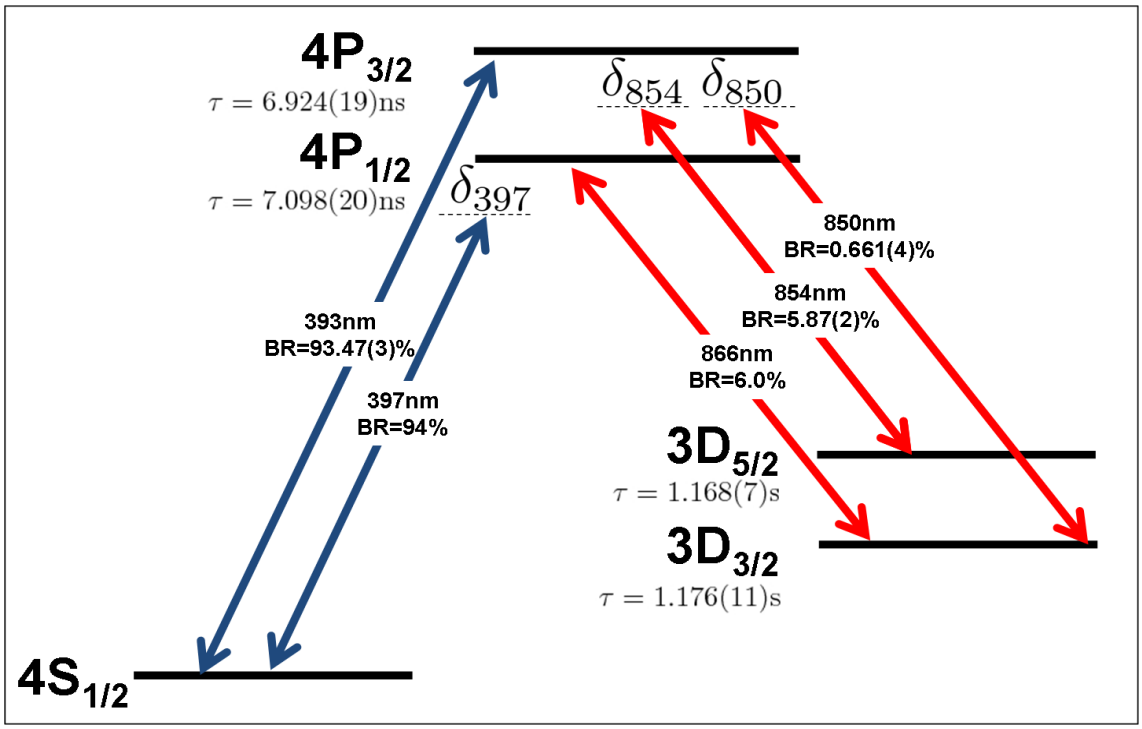

Figure 2.9: ^{40}Ca-ion level scheme showing the transitions used for Doppler cooling. Calcium ions can be Doppler cooled using the $4S_{1/2} \rightarrow 4P_{1/2}$ transition at 397 nm with the addition of appropriate re-pump lasers tuned to 850 nm and 854 nm. The lifetimes (τ) of each level, the transition branching ratios (BR) and approximate wavelengths are shown. Transition branching ratios and state lifetimes are taken from [62, 65].

upper cooling state is

$$N_{P_1} = \Bigg[\frac{A_{P_1D_1}}{B_{D_1P_2}\rho_{850}(\nu)}\left(1+\frac{A_{P_2D_1}}{A_{P_2S_1}}\right)+\frac{A_{P_1D_1}}{A_{P_2S_1}}\left(3+\frac{A_{P_2D_2}}{B_{D_2P_2}\rho_{854}(\nu)}\right) + \frac{A_{P_1S_1}}{B_{S_1P_1}\rho_{397}(\nu)}\left(1+\frac{A_{P_1D_1}}{A_{P_1S_1}}\right)+2\Bigg]^{-1}. \tag{2.51}$$

For high intensity re-pump lasers $B_{D_1P_2}\rho_{850}(\nu) \rightarrow \infty$ and $B_{D_2P_2}\rho_{854} \rightarrow \infty$, and the $4P_{1/2}$-state population can be expressed in terms of the 397 nm laser intensity as

$$N_{P_1} = \left[3\cdot\left(\frac{\Gamma_{866}}{\Gamma_{393}}\right)+\frac{2}{s}\left(1+\frac{\Gamma_{866}}{\Gamma_{397}}\right)+2\right]^{-1}, \tag{2.52}$$

where $s = I_{397}/I_{sat} = \big(2\cdot B_{S_1P_1}\rho_{397}(\nu)\big)/A_{S_1P_1}$ is the saturation parameter of the $4S_{1/2} \rightarrow 4P_{1/2}$ transition and $\Gamma_\lambda = A_{ji}$ are the spontaneous decay rates. For $s \gg 1$, the $4P_{1/2}$-state population is given by:

$$N_{P_1} = \left[3\cdot\left(\frac{\Gamma_{866}}{\Gamma_{393}}\right)+2\right]^{-1} = 0.457. \tag{2.53}$$

Following the same procedure, the steady state population of the $4P_{3/2}$-state for high intensity re-pump lasers and for $s \gg 1$ is given by:

$$N_{P_2} = \left(\frac{\Gamma_{866}}{\Gamma_{393}}\right)\cdot\left[3\cdot\left(\frac{\Gamma_{866}}{\Gamma_{393}}\right)+2\right]^{-1} = 0.029, \tag{2.54}$$

and the total population in the two excited states is

$$N_{P_1} + N_{P_2} = 0.457 + 0.029 = 0.486. \tag{2.55}$$

The maximum population of the upper cooling transitions is therefore lower than in the case of the two-level system but significantly higher than in the case of the Λ-system. As a result, we expect the scheme to provide more efficient Doppler cooling compared to the Λ-system. In addition, the scheme is free from the effects of coherent population trapping if we ensure $\delta_{850} \neq \delta_{854}$. As a consequence of re-pumping with the $4P_{3/2}$-state, the effective lifetime of the $4P_{1/2}$-state is longer than in the two-level system model. The increased $4P_{1/2}$-state lifetime corresponds to a lower effective decay rate and therefore the saturation intensity, given by Equ. 2.32 for the two-level system, is lower for the five-level system. We have confirmed this effect by measuring the saturation intensity and the results of the experiment are discussed in chapter 5

2.2.4 Laser force on the ion

The laser field exerts a force on the ion through the absorption of photons. Each absorbed photon exerts momentum $\hbar\vec{k}$ to the ion, where $\vec{k}$ is the propagation direction of the laser. Due to the linear Doppler effect, absorption of photons from the laser field will depend on the ion's velocity component in the propagation direction of the laser. This results in a Doppler shift of the laser detuning from δ to $(\delta+\vec{v}\cdot\vec{k})$. For an ion counter-propagating with the laser, the shifted laser detuning becomes $(\delta+v_k k)$. The force on the ion due to photon absorption can be expressed as the product of the scattering rate and the momentum of the photon:

$$\vec{F} = \gamma_{\text{scatt}} \cdot \hbar\vec{k}. \tag{2.56}$$

In the two-level system model, γ_{scatt} is given by Equ. 2.33 and the force on the ion is

$$\vec{F} = \hbar\vec{k}\frac{s\Gamma/2}{1+s+\left(\frac{(\delta+v_k k)}{\Gamma/2}\right)^2}, \tag{2.57}$$

where the laser detuning term δ now includes a contribution from the ion's collinear velocity v_k and the laser field is assumed to be weak such that $\Gamma' \approx \Gamma$.

The energy gained by the ion after absorbing a photon is radiated through spontaneous emission after an average time $\tau = 1/\Gamma$ following the absorption event. The emitted photon exerts a recoil kick to the ion with a momentum equal in magnitude to the momentum gained during absorption. Each spontaneous emission event increases the ion's kinetic

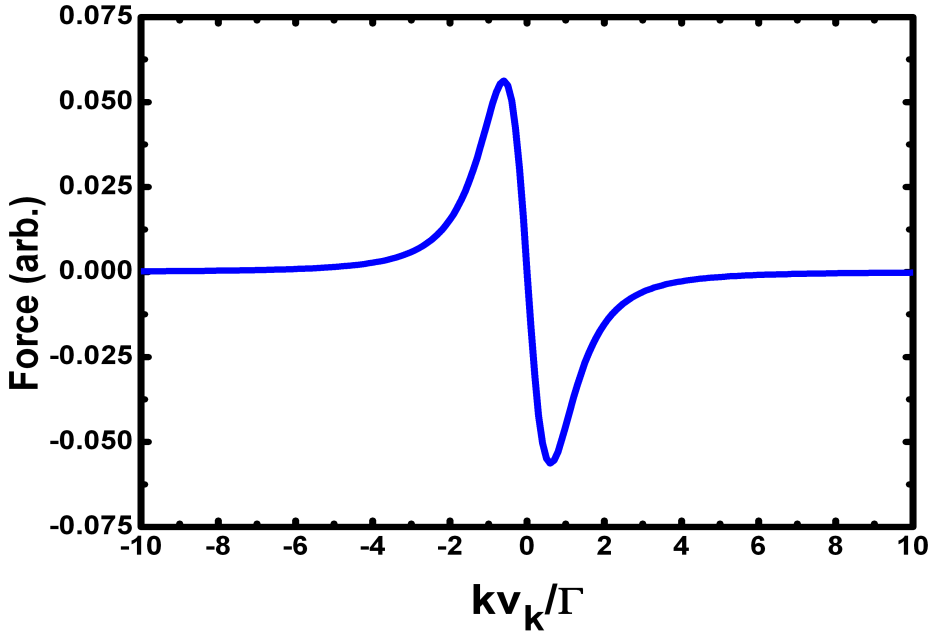

Figure 2.10: The laser force on the ion from a pair of counter-propagating laser beams as a function of the ion's velocity. The constant light pressure force on the ion is zero and the net force is $2\beta v_k$. For small ion velocities, the approximately linear restoring force keeps the ion at rest when the laser detuning is negative. A laser detuning of $-\Gamma/2$ is selected to maximise the slope of the linear region.

energy by $(\hbar k)^2/2m$ and this occurs at a rate of γ_{scatt} giving a total heating rate of $\gamma_{\text{scatt}} \cdot (\hbar k)^2/2m$. However, the spontaneous emission of photons is an isotropic process with photon propagation directions covering the full solid angle. After many scattering events the total momentum imparted to the ion through spontaneous emission averages to zero. Therefore, the net force on the ion is determined entirely by the propagation direction of the interaction laser and the atom's velocity as described by Equ. 2.57.

For an ion with small velocity colinear with the laser, Equ. 2.57 can be approximated by the first two terms of a Taylor expansion around $v_k = 0$:

$$\vec{F}(v_k) = \vec{F}_0 - \beta v_k, \tag{2.58}$$

where

$$\vec{F}_0 = \hbar\vec{k} \cdot \frac{s\Gamma/2}{1 + s + \left(\frac{\delta}{\Gamma/2}\right)^2} \tag{2.59}$$

and

$$\beta = -\frac{4\hbar k^2 \delta}{\Gamma} \cdot \frac{s}{\left[1 + s + \left(\frac{\delta}{\Gamma/2}\right)^2\right]^2}. \tag{2.60}$$

In this approximation the total force on the ion is made up of a constant light pressure force ($\vec{F}_0$) directed along the propagation direction of the laser and a force that depends

on the ion's velocity collinear with the laser beam (βv_k). The velocity dependent term can provide a viscous damping force or a driving force depending on the detuning of the interaction laser. For a red-detuned laser ($\delta < 0$) the force opposes the motion of the ion. By adding a second laser to the system, directed counter-propagating with respect to the first laser and with equal intensity and detuning, the constant radiation pressure forces from the two lasers cancel. The result is an approximately linear velocity dependent restoring force applied to the ion around $v_k = 0$. Fig. 2.10 shows the force on the ion as a function of its velocity for a pair of counterpropagating lasers. The slope of the linear restoring force is maximised for a laser detuning of $\delta = -\Gamma/2$.

2.2.5 Doppler cooling

The process described above of applying a velocity dependent restoring force to the ion using red-detuned lasers is called Doppler cooling. The temperature of the ion during Doppler cooling is defined by the equilibrium reached between the rate of laser cooling and the rate of heating due to spontaneous emission events. The heating rate of the ion is equal to $\gamma_{\text{scatt}} \cdot (\hbar k)^2/m$. The rate of cooling is given by $\langle \vec{F} \cdot \vec{v} \rangle = 2\beta \langle v_k^2 \rangle$ when the contribution from both lasers is taken into account. Equating the cooling and heating rates, and setting $\delta = -\Gamma/2$, gives the minimum Doppler cooling temperature:

$$T_{limit} = \frac{\hbar\Gamma}{2k_b}. \tag{2.61}$$

For atoms typically used in ion trapping experiments, this corresponds to a minimum temperature on the order of mK.

Doppler cooling an ion confined in the pseudopotential well described in Sec. 2.1 can be accomplished with a single laser since the trapped ion reverses direction during each half-cycle of its harmonic motion around the trap centre. If the laser propagation vector $\vec{k}$ has a component in all three directions of the ion's motion, the ion can be efficiently cooled in all three spatial dimensions.

2.2.6 Doppler velocimetry

Doppler velocimetry is the mapping of the ion's oscillatory motion onto its fluorescence [41, 43, 44]. This technique has been employed to measure the secular motion of trapped ions in several of the experiments discussed in this thesis.

The ion's secular oscillations in the trapping potential, as described by equations 2.17 - 2.19, result in a time varying Doppler shift during interaction with the Doppler cooling

laser. For a fixed laser frequency, the time varying Doppler shift manifests as a modulation of the ion's fluorescence signal. Thus, by measuring the ion's fluorescence modulation the frequency of the ion's motion can be determined.

For small ion velocities $\vec{v}$ the amplitude modulation of the laser induced fluorescence can be expressed as

$$\mathcal{F} = \Gamma \left. \frac{d\rho_{ee}}{d\delta} \right|_{\delta_0} \vec{k} \cdot \vec{v}, \tag{2.62}$$

with the detuning between the laser and the atomic resonance δ_0, the laser wave vector $\vec{k}$, the spontaneous decay rate Γ and the population of the upper cooling state ρ_{ee}.

The ion's oscillation amplitude is damped as it interacts with the red detuned cooling laser as discussed in Sec. 2.2.4. By exciting the ion's oscillatory motion and recording the fluorescence during damping with the Doppler cooling laser, the secular frequency can be measured with high precision. Due to the proportionality of the ion's secular frequency to its charge-to-mass ratio (see Equ. 2.10 and Equ. 2.14), precise measurements of the secular frequency allow for precision metrology of ions with known electric charge. The application of this technique to chemical reaction studies is the topic of chapters 6 and 7.

Rather than damping the ion with a red detuned laser, the ion's oscillation can be amplified by blue detuning the cooling laser [51, 67]. For a blue detuned laser, the radiation pressure for co-propagating ions exceeds that of the counter-propagating case. This results in an enhancement of the ion's oscillation velocity and thus its amplitude. The increase in modulation amplitude can, for small amplitudes, be described by an exponential increase with amplification time τ by

$$G(\tau) = \exp\left[\frac{\pi h}{m\lambda^2} \left. \frac{dR}{d\delta} \right|_{\delta_0} \tau \right], \tag{2.63}$$

where $R(\delta)$ is the ion's fluorescence rate and δ_0 is the detuning of the interaction laser. Even though this describes the behavior of the coherent motion well, the blue detuning of the laser also induces heating which in turn results in a motional broadening of the fluorescence spectrum. This broadening causes a significant decrease in the gain of the coherent motion.

The oscillation of the ion's velocity results in a periodic change in the laser detuning, in the reference frame of the ion, due to the linear Doppler effect. The resulting fluorescence modulation $\mathcal{F}_m$ can be expressed for small velocities as

$$\mathcal{F}_m(\tau) = \frac{2\pi h \Delta R}{m\omega_0\lambda^2} \left. \frac{dR}{d\delta} \right|_{\delta_0} G. \tag{2.64}$$

Thus, the transfer of the Doppler induced detuning modulation depends on the gradient of the fluorescence spectrum. The detection efficiency can therefore be optimised by tuning the detection laser to the point of steepest slope on the spectral lineshape.

We have demonstrated that small amplitude ion oscillation, seeded by optical forces, can be coherently amplified through the ion's interaction with a blue detuned laser. A novel secular frequency measurement technique based on this idea is the topic of chapter 8 and the application of this technique to the non-destructive state detection of trapped molecular ions is discussed in chapter 9.

Chapter 3

All-optical ion generation for ion trap loading

3.1 Introduction

Commonly, ion traps are loaded using a neutral atomic beam created through effusion from a resistively heated oven and ionised either by electron impact or photo-ionisation in the trap centre. Ion trapping experiments typically aim to load single ions or small numbers of ions and thus a large continuous flux of atoms passing through the trap structure is undesirable. Atoms from the beam may become deposited on the trap electrodes or dielectric surfaces in the set-up, leading to local patch potentials. The build-up of contaminants on the trap electrodes has been shown to significantly increase the heating rate of trapped ions over time [68, 69]. This is particularly pertinent for experiments seeking to cool trapped ions to the motional ground state.

In recent years, the scaling-up of ion traps has been proposed through the creation of microtrap arrays [70, 71, 72]. However, as ion traps become smaller the experimental difficulties presented by the loading process become more critical. Also, combining ion traps with ultra high quality optical cavities [73, 74, 75] poses severe requirements on the loading process as any contamination of the mirror surfaces will deteriorate the cavity quality.

The atomic flux produced by effusive ovens is continuous and cannot be quickly switched off, thus inevitably producing an excess of evaporated atoms. In addition, the presence of a hot oven at typically several hundred degrees Celsius in the close confines of a micro-scale ion trap array may cause damage. The production of atomic beams through

pulsed laser ablation (PLA) eliminates the need for an oven in the experimental design. The ablation of metal surfaces has been studied extensively (see for example [76, 77]) and with the advances of high power pulsed diode lasers the method may become suitable for complete integration in ion chips.

PLA utilises high energy laser pulses that strike a target material and heat a strongly localised region to high temperatures. This creates discrete bunches of atoms leaving the target surface in response to each laser pulse. Together with resonant photo-ionisation, ions can be produced isotope selectively.

Highly efficient ion trap loading has been demonstrated for calcium ablated with Nd:YAG laser pulses in a large trap [78] and for the loading of strontium into a surface trap with a frequency trippled Nd:YAG laser [79]. Employing high energy UV laser pulses resulted in the generation of ions and excited atoms in the ablation process which makes this method less suitable for isotope selective photoionisation. In contrast, Hendricks et al. demonstrated that thermal ablation with a Nd:YAG laser can produce atoms exclusively in the ground state if the fluence is below a threshold around 300 mJ/cm^2.

Combining PLA with an efficient ionisation process provides unparalleled control over ion trap loading. The evaporation of atoms through the ablation may be maintained as long as required to produce the desired number of trapped ions. Thus, after detecting the correct number of ions the ablation process can be stopped instantaneously. By contrast, evaporation during the heat up and cool down phase of an oven leads inevitably to an excess of released atoms. Due to the high temperatures of the ablated atoms, the loading may be less efficient compared to a conventional oven for shallow traps. However, D.R. Leibrandt et al. [79] have demonstrated the loading of a surface trap with a trap depth as low as 40 meV.

In this chapter we present a detailed experimental investigation of this all-optical ion generation technique and we present an analysis of the suitability of PLA for ion trap loading. We directly compare the flux and velocity distributions of atomic beams created by PLA and an effusive oven. By analysing the distribution of the kinetic energy, we evaluate the efficiency of the loading process.

3.2 Experiment

In order to compare the atomic beams created by a resistively heated oven and PLA, the set-up is designed to reproducibly exchange an oven and an ablation target. A schematic

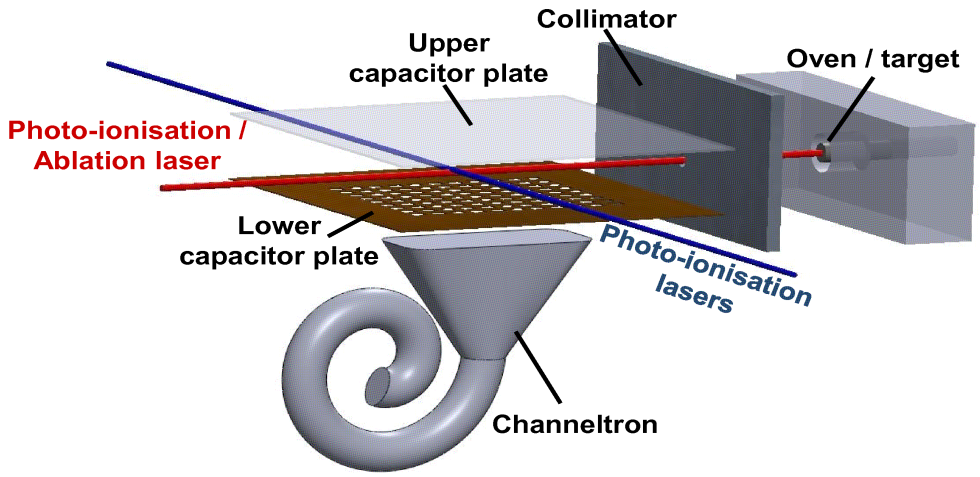

Figure 3.1: Experimental set-up for studying PLA. The atomic flux originating at the calcium source, which is either the resistively heated oven or the calcium target, is collimated into an atomic beam by the 250 μm aperture. The 1064 nm ablation laser beam is directed along the atomic beam axis and normal to the calcium target surface. The photo-ionisation lasers are aligned orthogonal to the atomic beam axis. When the ablation laser is not in use, the photo-ionisation lasers may be split into two paths using a PBS (not shown in the schematic) and aligned both orthogonal and counter-propagating with respect to the atomic beam axis. Calcium atoms are ionised in the region between the capacitor plates and detected at the channeltron.

of the experimental set-up is shown in Fig. 3.1. The oven and ablation target sources can be exchanged without altering any other component of the set-up. Calcium atoms emitted from the source are collimated by an aperture to achieve an atomic beam. Calcium atoms in the beam are ionised 20 mm behind the collimator, above a channeltron ion detector, to measure the flux. The channeltron is mounted below a grounded metal mesh in order to shield the ions from the high voltage that is needed for the operation of the ion detector. The field from a positively charged plane metal plate above the ionisation point accelerates the ionised atoms towards the channeltron.

3.2.1 Vacuum system

The set-up is contained within a vacuum system consisting of a five-way-cross with a high voltage feedthrough port, a sub-D feedthrough port, an ion gauge and a UHV valve. A chamber cap, with several window ports for laser and imaging access, is mounted on top of the five-way-cross and houses the experimental set-up shown in Fig. 3.1. The UHV valve allows for optionally connecting an ion pump or a pumping station consisting of a turbomolecular pump backed by a rotary pump. With the pumping station connected, a typical pressure of 10^{-7} mbar can be achieved within the chamber. This pressure is sufficiently low for studying calcium effusion from the resistively heated source or from the ablated solid calcium target. Windows in the chamber allow laser beams to be aligned orthogonal and counter-propagating with respect to the direction of the calcium atomic flux.

3.2.2 Photo-ionisation

The loading efficiency and isotope selectivity that resonant two-step photo-ionisation offers has made it the preferred technique over electron impact ionisation for the clean loading of ion traps. Loading efficiencies up to five orders of magnitude larger [60, 80] means that a smaller flux of neutral atoms is required, resulting in a decrease in the contamination of the trap electrodes [81].

Photo-ionisation of neutral ground state calcium atoms is a two-photon process with the first photon at 423 nm resonant with the $4S_0 \rightarrow 4P_1$ transition and the second photon with wavelength less than 389 nm providing the energy necessary to ionise the excited state calcium atoms. Fig. 3.2 shows the relevant energy levels of ground state neutral calcium used in the photo-ionisation process.

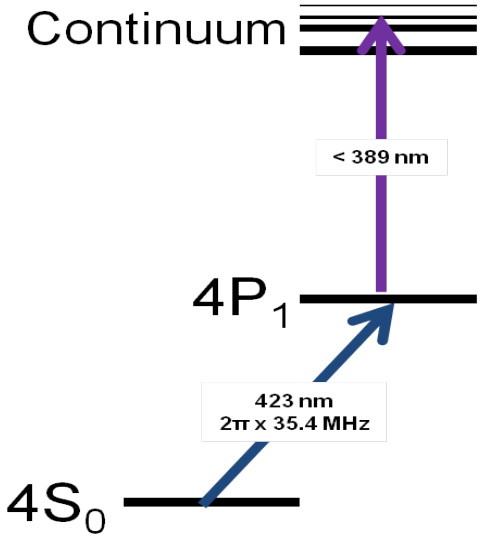

Figure 3.2: Level scheme of neutral calcium atoms showing the states relavent to the two-stage photo-ionisation process. The first photon at 423 nm is resonant with the $S_0 \rightarrow P_1$ transition. The second photon, with a wavelength less than approximately 389 nm, supplies the energy necessary to excite the atom to the continuum.

The first stage photo-ionisation light is supplied by a laser diode[1] with an external cavity in the Littrow configuration. By adjusting the feedback grating as well as the diode current and temperature, the laser is tuned to 423 nm. During typical operation it has an output power of around 4 mW. The elliptical output beam is aligned through an optical isolator and circularised with a cylindrical lens pair. A glass wedge plate is used to deflect around 4% of the beam, which is coupled into a multi-mode fibre and sent to the wavemeter. A portion of the primary beam is coupled into a single-mode polarisation maintaining fibre and sent to the experiment.

The second stage photo-ionisation light is supplied by a laser diode at 375 nm[2]. The laser diode is set-up without an external cavity grating since frequency tuning is not necessary. The laser outputs 10 mW of power for an operating current of 55 mA. The output light is coupled directly into a single-mode polarisation maintaining fibre and sent to the experiment.

Using a polarization beam splitter, the pair of overlapped laser beams are split into two paths. One set of lasers is aligned orthogonal to the atomic beam to minimise Doppler broadening. Another set of photo-ionisation lasers is aligned counter-propagating with respect to the atomic beam by optimising the transmission through the collimator and

[1] Nichia Photonics
[2] Nichia Photonics

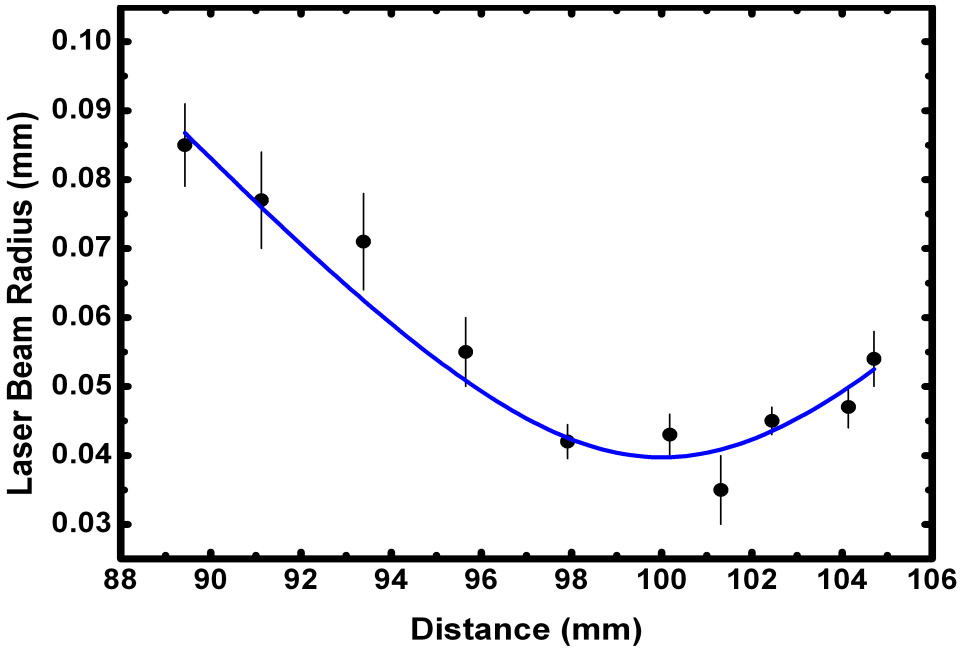

Figure 3.3: The ablation laser beam half width as a function of distance from the focusing lens. Each data point corresponds to a position in the laser beam path. The laser half width and error bars are determined by fitting Equ. 3.1 to the data collected at each position. The equation of a Gaussian laser beam (Equ. 3.2) is fit to the data set (solid line). The measured half width of the ablation laser beam at the focal point is 40(2) μm.

the oven aperture (see Fig. 3.1). Both laser beams have a diameter of 250(15) μm at the interaction region above the channeltron.

3.2.3 Resistively heated oven

The standard way of creating an atomic beam is effusion from a resistively heated oven. The oven used in this experiment is a cylindrical tantalum tube 13 mm long with a diameter of 1 mm packed with calcium metal filings. The front of the tube is left open and directed toward the interaction region above the channeltron. The bottom of the tube is crimped shut. Tantalum wires are spot welded to the top and bottom of the tube to form a circuit. Passing a current (typically between 1 A and 2 A) through the circuit causes the temperature of the tube to increase through resistive heating. For a temperature of several hundred degrees Celsius, an appreciable flux of electrically neutral calcium atoms effuses from the tube into the surrounding vacuum and toward the interaction region. An aluminum plate with a 250 μm hole concentric with the line passing through the centre of the interaction region and the centre of the tantalum tube serves as a collimator for the atomic beam. The calcium beam passing through the collimator has a divergence of smaller than 3°.

3.2.4 Pulsed laser ablation

Alternatively, the atomic beam can be created by PLA of a solid calcium target. The ablation laser used in this experiment is a Q-switched 1064 nm Nd:YAG laser[3]. The laser can operate with repetition rates between 1 Hz and 160 kHz, has an M^2 value less than 1.2 with an average pulse width of 10 ns and a maximum pulse energy of 120 μJ. The collimated ablation laser beam is focused with a single convex lens with 100 mm focal length onto the calcium target. The beam is aligned to pass through the centre of the collimation aperture.

The calcium target is solid calcium metal mounted inside a stainless steel block. The target is a calcium cylinder 3 mm in diameter that fits tightly into a cylindrical hole in the block mount. The calcium cylinder is pressed into the mount. This procedure ensures good thermal contact between the calcium and the surrounding stainless steel. Immediately prior to installing the target into the vacuum chamber, the calcium surface is polished with a file to remove any contaminants. The calcium target mount is electrically isolated, so that a potential difference between the target surface and the collimation aperture plate can be applied. This electric field can be used to prevent charged particles created through the ablation process from passing through the aperture, thus allowing us to analyse the composition of the atomic beam produced through PLA.

The width of the ablation laser at the surface of the calcium target is determined by redirecting the laser with a mirror and measuring the width at a distance equal to the distance from the mirror to the target surface. A razor blade, aligned with cutting edge orthogonal to the propagation direction of the laser beam, is translated in steps through the beam with a micrometer stage while measuring the relative power with a photodiode positioned behind the blade. The laser power as a function of razor blade position is given by

$$P(x) = \frac{P_{tot}}{2}\left[1 - \mathrm{erf}\left(\frac{\sqrt{2}x}{w}\right)\right], \tag{3.1}$$

where P_{tot} is the power of the unobstructed beam, w is the beam waist and $\mathrm{erf}(x)$ is the error function [82]. By fitting equation 3.1 to the data, the width of the laser is determined for a single position in the beam path. This procedure is repeated for a series of positions around the focal point and the result is shown in Fig. 3.3. The equation for the half width of a Gaussian beam as a function of position is given by

$$w(z) = w_0\sqrt{1 + \left(\frac{z}{z_R}\right)^2}, \tag{3.2}$$

[3]Newport BL-10-106Q

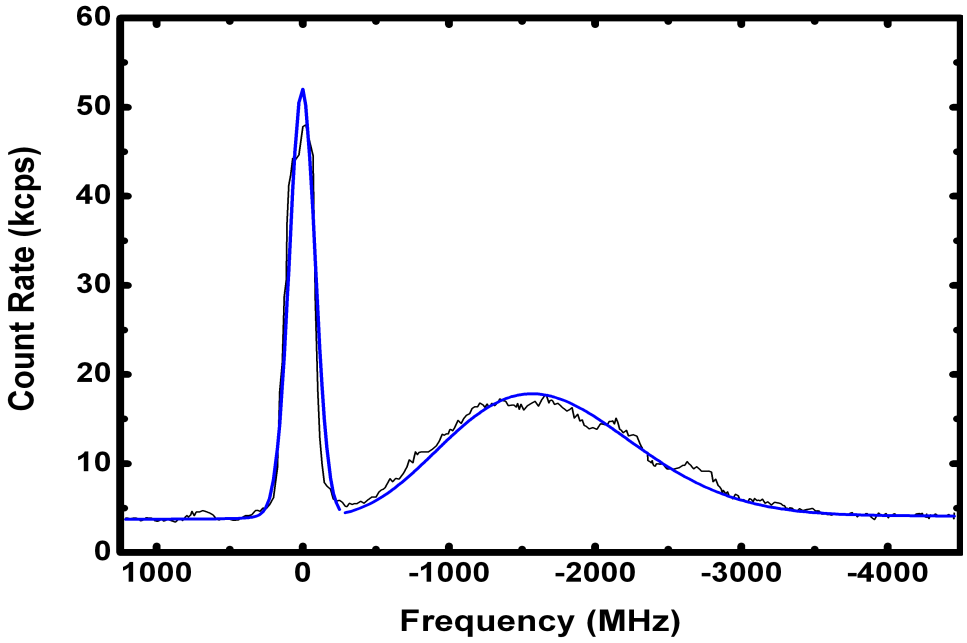

Figure 3.4: Ion count rate as a function of the first stage photo-ionisation laser frequency for an oven current of 1.9 A. The Doppler-free absorption profile is obtained by orthogonal photo-ionisation laser beams while the maximally Doppler broadened profile is obtained by counter-propagating photo-ionisation laser beams. The temperature of the oven is determined by fitting Eq. (3.3) to the Doppler broadened absorption profile relative to the measured resonance of the $^1S_0 \rightarrow {}^1P_1$ transition.

where w_0 is the beam half width at the focus and z_R is the Rayleigh range. Equ. 3.2 is fit to the data and the half width of the ablation laser beam at the focal point is 40(2) μm. For this laser beam spot size, and for a pulse repetition rate of 15 kHz, laser fluences up to 2000 mJ/cm^2 can be achieved.

The direction of the ablation laser beam can be adjusted by a mirror that is controlled by a two-dimensional piezoelectric actuator tilting stage to allow for the scanning of the beam position on the target. Following the procedure reported in [78], small position changes of the ablation laser beam on the target are found to produce a consistent flux of calcium from the target. With the ablation laser beam stationary on the target surface the calcium flux is found to decrease rapidly with time, dropping to an immeasurable level after only a few thousand pulses. It is not clear what causes this effect. Two sine functions, with typical frequencies on the order of 100 Hz and a difference frequency on the order of 10 Hz, are empirically chosen and applied to the two dimensions of the PZT titling stage. This procedure produces a constant flux of calcium over the time scales used in this experiment.

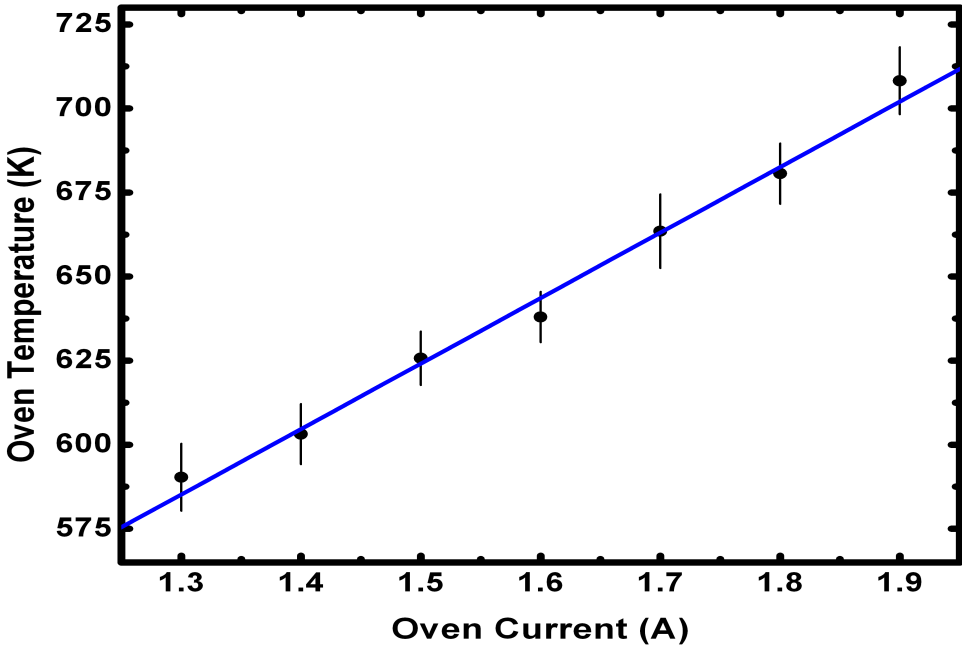

Figure 3.5: Oven temperature as a function of current. Each data point is the mean of a set of several measurements and error bars are the standard deviation. The relationship is linear for the range of currents used in this experiment.

3.2.5 Detection

Calcium atoms photo-ionised in the interaction region are detected at the channeltron. The output signal is converted into TTL pulses and recorded by a computer. A photo-ionisation spectrum can thus be measured by scanning the 423 nm laser wavelength and simultaneously measuring the ion detector count rate. Additionally, the time-of-flight of the atoms from the source to the detection region at a distance of 25(2) mm can be measured by recording the delay between the ablation laser trigger pulses and the ion count signal with a digital multiscaler card with nanosecond resolution[4].

3.3 Results

3.3.1 Resistively heated oven

In order to obtain a measure of the atomic flux effusing from the oven, spectroscopy of the $^1S_0 \rightarrow {}^1P_1$ transition is employed. The orthogonal and counter-propagating photo-ionisation lasers are scanned simultaneously over a 5 GHz range by applying a voltage ramp to the tilting piezoelectric actuator fixed to the 423 nm laser optical feedback grating. Fig. 3.4 shows the photo-ionisation spectrum for an oven current of 1.9 A. The sharp

[4]FastComTech P7888

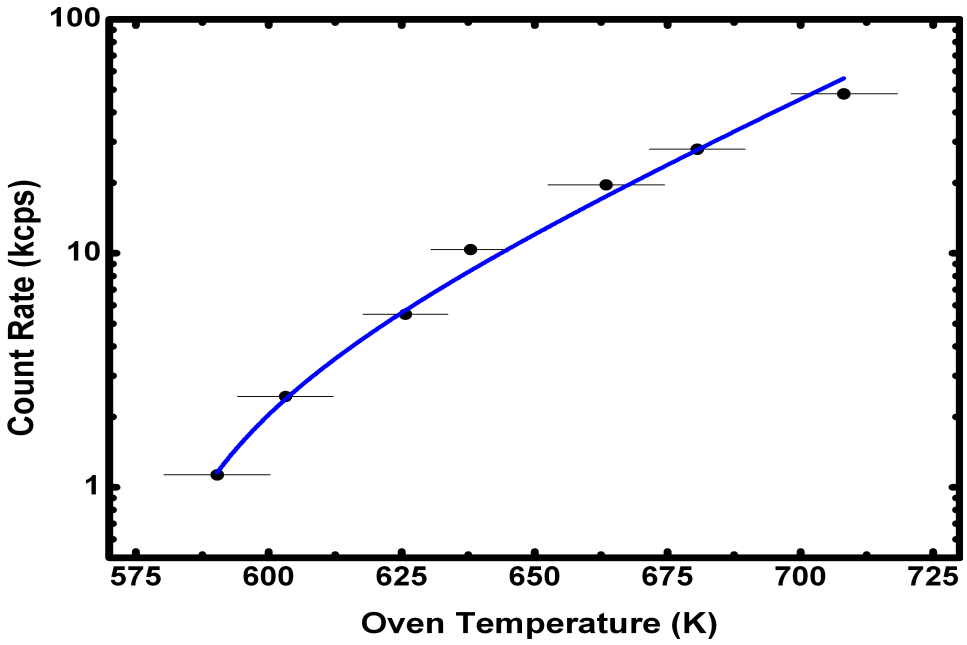

Figure 3.6: Ion count rate as a function of oven temperature. Oven temperatures are determined from the Doppler broadened absorption profile and the count rate is proportional to the area of the minimally broadened ${}^1S_0 \rightarrow {}^1P_1$ transition peak. A function has been fit to the data according to the model presented in [84].

peak at low wavelength is centered at the transition wavelength and originates from the photo-ionisation of atoms by the orthogonally aligned lasers. A Voigt profile is fit to the resonance peak to obtain the width and position. Due to the large laser powers, the width is primarily determined by the saturation broadening of the transition. Doppler broadening of the resonance due to the divergence of the atomic beam is negligible. The broad peak at longer wavelengths in Fig. 3.4 is a result of the interaction of the atoms with the counter-propagating laser. The spectrum represents the velocity spread of the atoms in the atomic beam and can be described by a thermal velocity distribution with the following form:

$$f(\lambda) = N\left(\frac{\lambda}{\lambda_0} - 1\right)^3 \exp\left(-\frac{mc^2(\frac{\lambda}{\lambda_0} - 1)^2}{2k_B T}\right) \tag{3.3}$$

where N is a normalisation constant, λ_0 is the resonance wavelength of the transition (given by the measured centre of the orthogonal resonance peak), m is the mass of the calcium atoms, c is the speed of light and k_B is the Boltzmann constant [83].

The longitudinal temperature of the atoms can be obtained by fitting Equ. (3.3) to the measured spectrum. Fig. 3.5 shows the oven temperatures for currents in the range of 1.3 A up to 1.9 A in which the temperature increases approximately linear with the current.

In order to obtain the flux of atoms, the peak ion count rate is determined from the area of the orthogonal resonance peak. It is shown as a function of oven temperature in Fig. 3.6. The flux of calcium atoms increases with temperature according to the relationship between evaporation rate and temperature [84].

3.3.2 Pulsed laser ablation

In order to measure the velocity distribution of the atomic beam created by PLA, the time-of-flight of the atoms is measured. Fig. 3.7 shows time-of-flight spectra collected for two different laser fluences. The composition of the atomic beam was carefully analysed by applying a voltage to the target in order to suppress the ionic fraction of the beam and by switching the resonant photo-ionisation laser (at 423 nm) to identify the neutral calcium atoms in excited states. Non-ground state atoms can still be ionised through field-ionisation by the electric field from the metal plate above the channeltron or by absorbing a 375 nm photon from the non-resonant photo-ionisation laser. In contrast, ground state atoms will not be ionised in the absence of the resonant laser field at 423 nm. Fig. 3.7(a) shows the spectrum of photo-ionised calcium atoms recorded for an ablation laser fluence of 280(20) mJ/cm^2. The atomic flux produced with this laser fluence consists entirely of ground state atoms. The analysis of several measurements show that atoms arriving in a time window between around 12 μs and 30 μs are all in the ground state. However, atoms arriving at earlier times are either in an excited state or are ions produced in the ablation process. Hence, the ground state atoms can be singled out by their arrival time.

As the ablation laser pulse fluence is increased, excited state atoms are created in addition to the ground state atoms. Hendricks et al. describe the creation of Rydberg atoms for a laser pulse fluence of 300 mJ/cm^2 [78]. The results presented here confirm the creation of non-ground state atoms, both excited state atoms and ions, beginning at a fluence of 315(16) mJ/cm^2. Fig. 3.7(b) shows the time-of-flight spectrum collected for an ablation laser fluence of 480(34) mJ/cm^2. The double peak structure located at arrival times shorter than 12 μs consists of fast ions and slower excited state atoms which are ionised either by the electric field or through absorption of non-resonant photons at 375 nm. The distribution of ground state arrival times is visible between 12 μs and 25 μs. Fig. 3.7(c) shows the same time-of-flight spectrum as in Fig. 3.7(b) but without the resonant 423 nm laser, thus eliminating the ground state component of the total spectrum.

A Maxwell-Boltzmann distribution is fit to each ground state arrival time spectrum in order to determine the temperature of the atoms and their most probable kinetic energy.

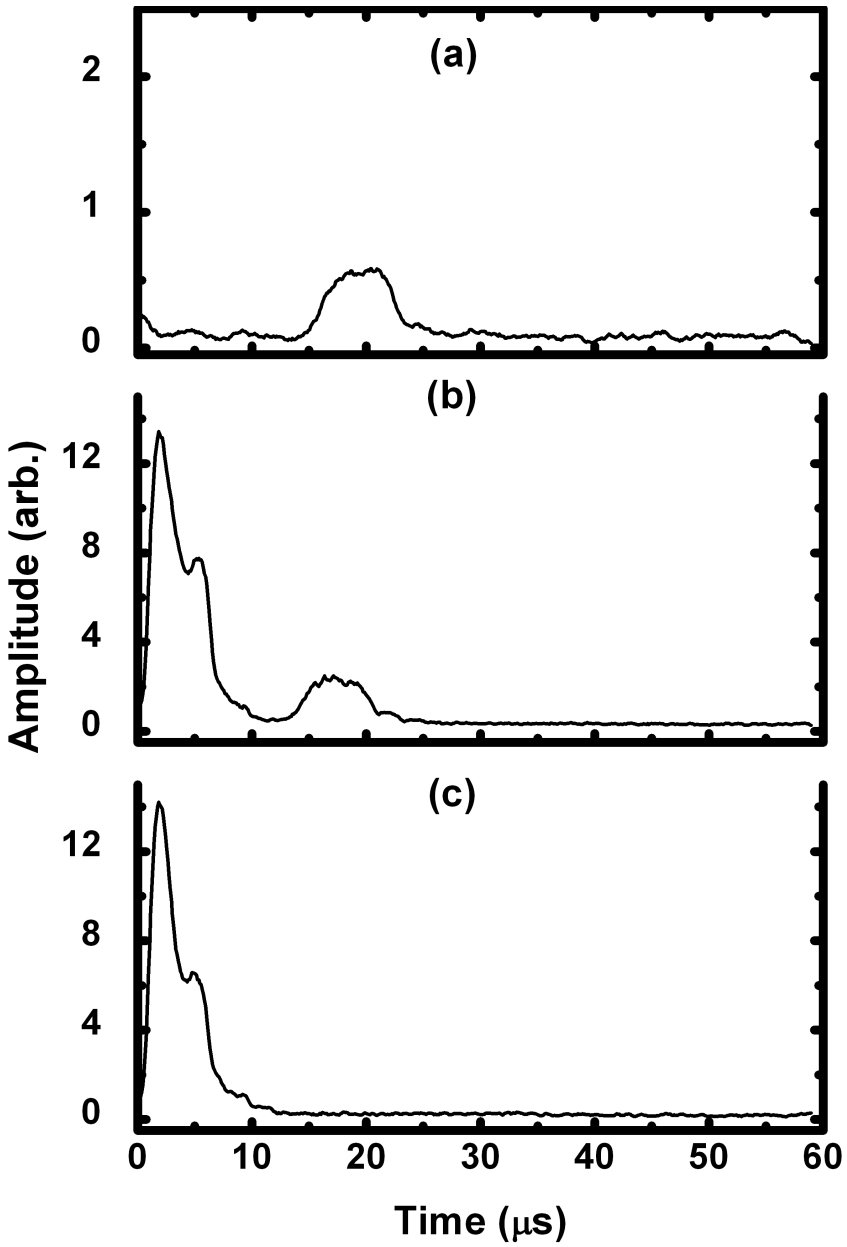

Figure 3.7: **(a)** Spectrum of arrival times for an ablation laser fluence of 280(20) mJ/cm^2 and with the photo-ionisation lasers on. For fluences below 300(22) mJ/cm^2 the signal consists entirely of ground state atoms. **(b)** Spectrum of arrival times recorded for an ablation laser fluence of 480(34) mJ/cm^2. The signal consists of both a ground state peak and a double peak structure consisting of both ions and excited state atoms. **(c)** Spectrum collected for the same parameters as in (b) but with the resonant 423 nm laser switched off. The signal consists of entirely non-ground state atoms.

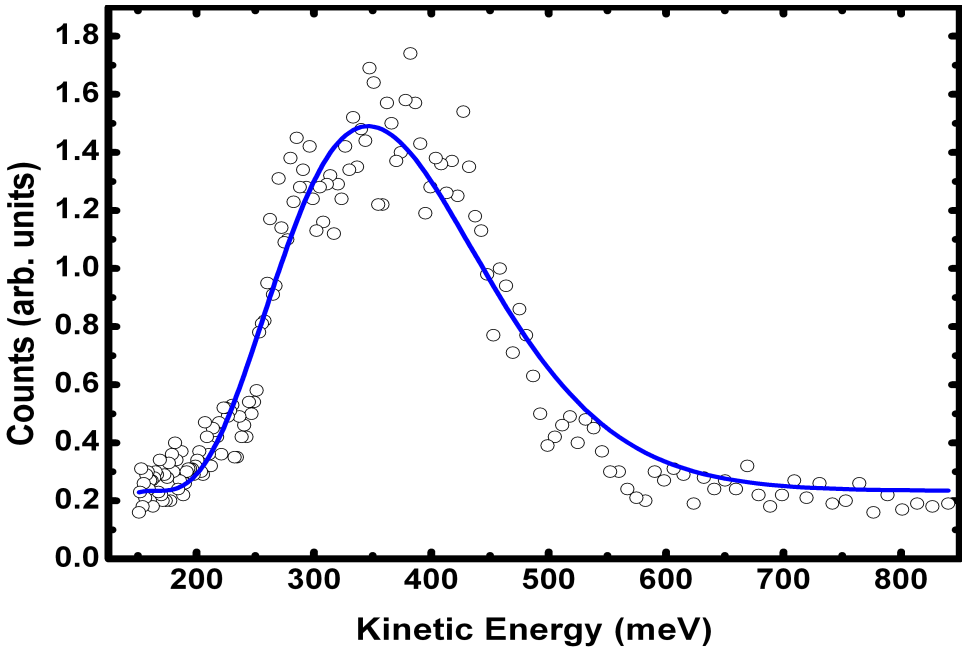

Figure 3.8: Distribution of photo-ionised calcium atoms produced by an ablation laser fluence of 480(34) mJ/cm^2. The time axis is converted to a kinetic energy axis. A Maxwell-Boltzmann distribution is fit to the spectrum and gives a temperature of 2680(67) K corresponding to a most probable speed of 1300(204) m/s and a most probable kinetic energy of 340(77) meV.

Fig. 3.8 shows the fit to a ground state time-of-flight distribution for an ablation laser fluence of 480(34) mJ/cm^2. The relationship between the temperature of the atoms and ablation laser fluence is shown in Fig. 3.9. In the range of fluences used in this work, the beam temperature increases linearly with increasing fluence. The temperatures are typically three to four times higher than for atomic beams created by a resistively heated oven.

Separate measurements were performed to determine the relative fluxes of ground-state and non ground-state particles as a function of ablation laser fluence. From time-of-flight spectra for a range of fluences, the ground-state and non ground-state fluxes are extracted from the total count rates in the time window from 12 μs to 24 μs for the ground-state flux and 0 μs to 12 μs for the non ground-state flux. The background count rate of the channeltron detector is subtracted from each measurement. The ground state and non-ground state count rates as a function of ablation laser fluence are plotted in Fig. 3.10. A non-ground state signal appears at fluences greater than 300(22) mJ/cm^2. The non-ground state signal increases rapidly with fluence and exceeds the ground state signal for fluences larger than 360(25) mJ/cm^2. For larger fluences, ground state atoms still form a portion of the total atomic flux as is illustrated in Fig. 3.7(b). However, the dominant

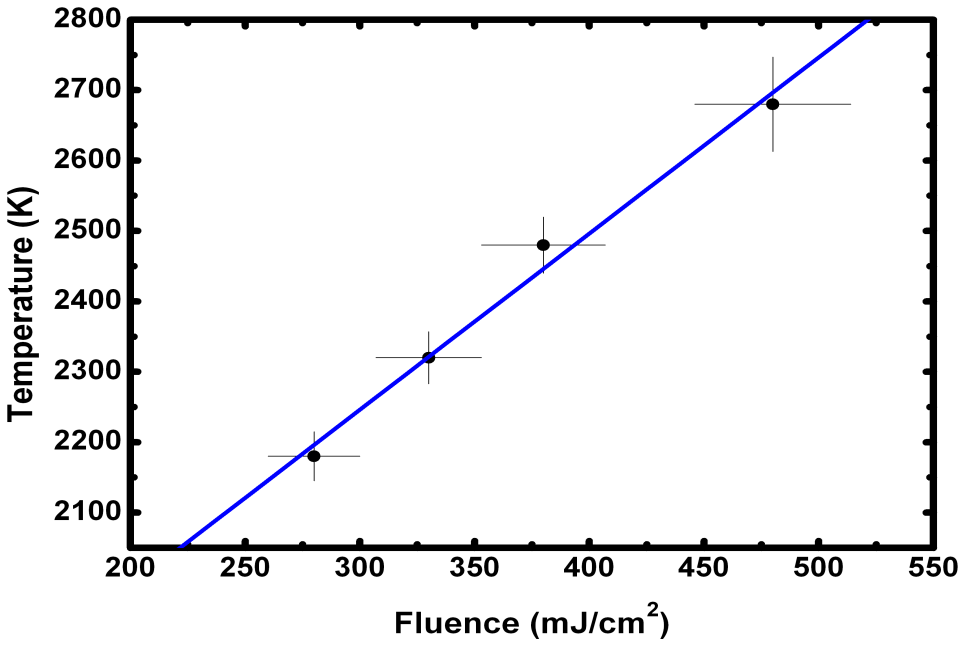

Figure 3.9: Temperature of the ablated atoms as a function of ablation laser pulse fluence. The temperature is measured by fitting a Maxwell-Boltzmann velocity distribution to the spectrum of photo-ionised atoms recorded for each ablation laser fluence. The relationship between temperature and fluence is linear for the range of fluences used in this experiment.

non-ground state fraction precludes isotope selective ion trap loading.

3.4 Comparison of methods

The most important figures of merit for loading ion traps are the generated flux of atoms in the ground state and their kinetic energy. In order to evaluate the flux of atoms generated by the two methods, we calculate the average flux created during a single ablation pulse and compare it with the flux effusing from the oven during the same time span. The flux of ground state calcium atoms produced during each 10 ns ablation laser pulse can only be matched for oven temperatures exceeding 650 K. At a pulse fluence of 300(22) mJ/cm^2 the average ground state atomic flux signal is 28(1) kcps. From Fig. 3.6 and Fig. 3.5, an equivalent flux may be produced by the oven at 680 K. This temperature corresponds to a total thermal load of 3.2 W. In comparison, the thermal load delivered to the target surface by the ablation laser is 230(2) mW, which is more than one order of magnitude smaller. This may be a decisive advantage for use with micro-scale ion trap arrays, integrated ion chips or cryogenic ion traps. Table 3.1 shows the average ground state flux produced by PLA and the oven temperature required to achieve the equivalent flux. The temperatures are calculated by extrapolating the fit in Fig. 3.6.

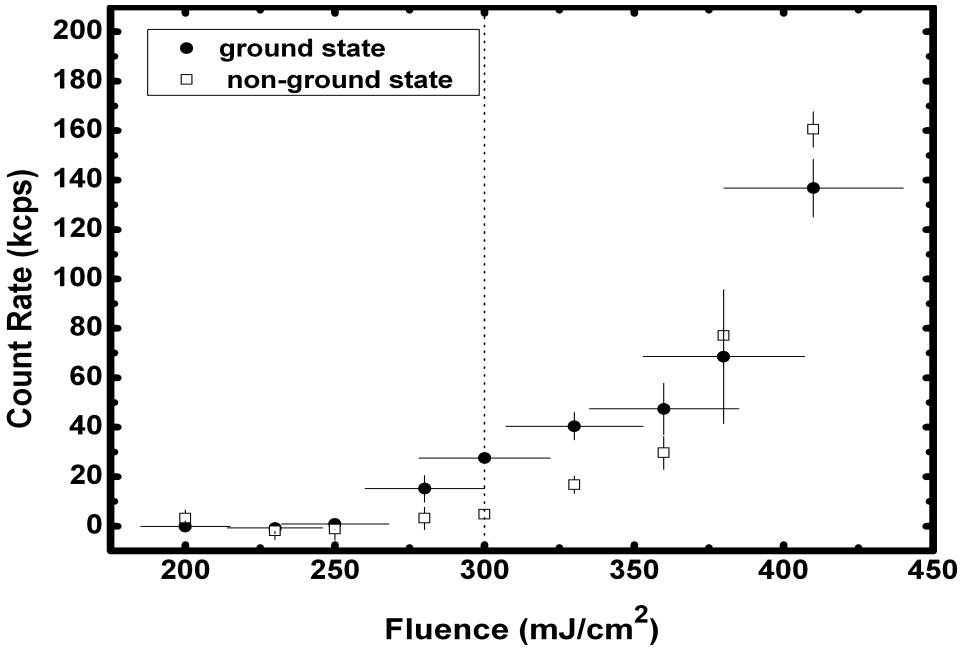

Figure 3.10: The ground state and non-ground state flux production rates for fluences in the range of 210(15) mJ/cm^2 to 410(30) mJ/cm^2. For fluences below around 300 mJ/cm^2 the signal is comprised entirely of ground state atoms. This region, to the left of the dashed line, is the ideal region for producing atomic beams in an isotope selective ion trap loading scheme. Above this fluence the atomic beam contains both ground and non-ground state atoms and the benefits of producing atomic flux through PLA are reduced.

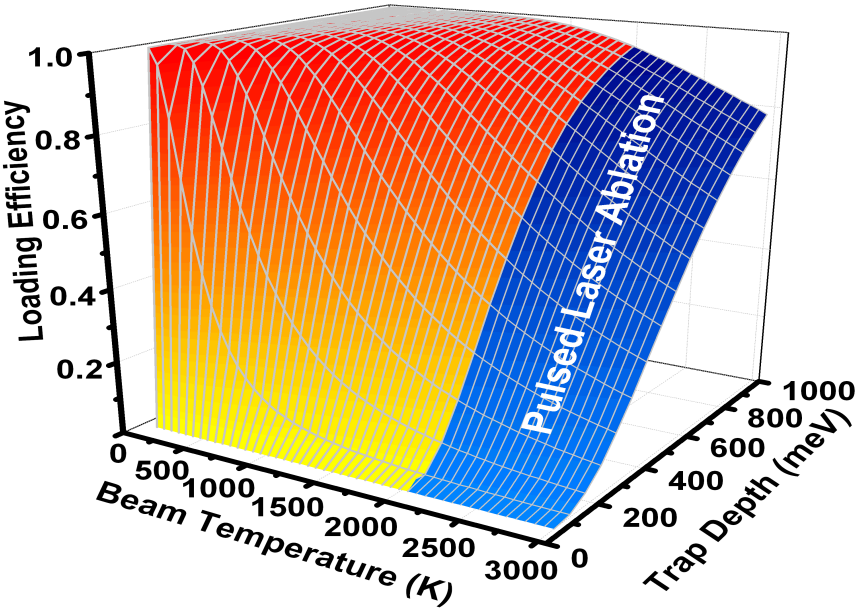

Figure 3.11: Fraction of the atomic flux which can be potentially trapped for a range of beam temperatures and trap depths. The atomic beam temperature range accessible to PLA is indicated in the diagram.

Table 3.1: Ground state count rates calculated for each ablation laser pulse fluence and resistively heated oven temperatures required to produce the equivalent atomic flux.

fluence (mJ/cm^2)	count rate (kcps)	oven temp (K)
280 ± 20	15 ± 5	660
300 ± 22	28 ± 1	680
330 ± 23	40 ± 5	700
360 ± 25	50 ± 10	710
380 ± 27	70 ± 26	720
410 ± 30	140 ± 11	740

The resistively heated oven delivers a continuous flux in contrast to the ablation laser, which creates discrete bunches of atoms. This is a considerable advantage as the pulsed ablation laser beam may be blocked following the successful loading of an ion, thus immediately halting the atomic flux. This may reduce the contamination of the trap structure significantly.

In other applications, the high repetition rate for loading the trap may be a crucial advantage. Given the fact that the loading cycle with an oven is determined by slow thermal conduction, experiments seeking to load single ions with kHz cycle time may only be possible using PLA. The warm-up time of the oven has been characterised in Sec. 7.5.1 and is shown to be on the order of 100 s.

The loading efficiency of ion traps depends on the temperature of the atomic beam as well as on the trap depth. The photo-ionisation process is not expected to be significantly impaired by the increased atomic velocities for the case of intense ionisation lasers orthogonally aligned with respect to the atomic beam. In our investigation, we found that the width of the atomic ionisation spectrum was the same for a conventional oven and PLA, limited only by saturation broadening of the transition. Thus, the residual Doppler broadening of the resonant transition was less than 100 MHz. The trap depth, however, limits the range of the kinetic energy spectrum of the atomic beam which can be utilised for ion trap loading. If ionised within the trap centre, only ions with a kinetic energy below the depth of the trapping potential are confined. With a significantly increased atomic beam temperature from PLA, the loading efficiency is greatly reduced for shallow traps. Figure 3.11 shows the fraction of atoms with a kinetic energy less than the trap depth for a range of atomic beam temperatures and trap depths. The temperature range of PLA is indicated in the graph. For a shallow ion trap with a depth of 100 meV only 4% of the atoms generated by PLA can be trapped as ions. In comparison, 34% of atoms from an effusive oven will be trapped for an atomic beam temperature of 700 K, which

corresponds to a comparable flux. However, already for a trap depth of 700 meV more than 80% of the atomic flux produced by PLA can be trapped.

3.5 Summary

The atomic beams produced through PLA have a Maxwellian velocity distribution with a temperature above the boiling point of calcium that increases linearly with the pulse fluence for the investigated range. The velocities are roughly a factor of 3-4 greater than those of atomic beams produced by a resistively heated oven. The corresponding kinetic energy is typically less than 350 meV, still well below the depth of typical macroscopic ion traps. However, for shallow traps the loading efficiency may be significantly impaired.

Below a threshold fluence of 315(16) mJ/cm^2, the atomic beam produced through PLA is shown to consist of exclusively ground state atoms. Maintaining a pulse fluence below this threshold ensures that a precisely controlled flux of ground state atoms is made available for isotope selective photo-ionisation.

PLA in combination with resonant photo-ionisation appears to be a viable alternative for loading ion traps. It offers unparalleled temporal control of the loading process as the production of ground state atoms can be started or halted instantaneously. High repetition rate ion trap loading could be useful in destructive spectroscopy experiments and chemical reaction studies involving small numbers of ions. If the ion trap requires reloading following a measurement, the PLA technique offers a greatly improved measurement cycle time compared to loading with a resistively heated oven.

Chapter 4

Ion trap and laser systems

4.1 Ion trap

All experiments with trapped ions described in this thesis are performed with the experimental ion trap, which is a linear rf Paul trap. A three-dimensional model of the ion trap is shown in Fig. 4.1. It consists of four stainless steel blade shaped rf-electrodes that provide the radial confinement of the ions. The separation of adjacent electrodes is 580 μm and the ion-electrode distance is 465 μm. The rf-electrodes are designed to allow good optical access in the radial plane. Radial lasers may be aligned with large components in both the vertical and horizontal planes. In addition, the blade shape of the rf-electrodes increases the solid angle available for ion fluorescence collection compared to a traditional cylindrical rod electrode configuration.

The trap geometry has been designed to be self-aligning, so that the electrode positions are entirely determined by the machining process. The electrode mount as well as the rf-electrodes are machined out of one block of stainless steel after precision holes have been reamed. After separating the parts and shaping the electrodes, the trap can be easily assembled by inserting precision ceramic dowel pins through the rf-electrodes and into the mount. Each rf-electrode is electrically insulated from the rest of the trap with ceramic spacers. This design ensures the desired symmetry and spacing of the rf-electrodes are preserved during assembly.

Positive static potentials applied to the two stainless steel DC endcap electrodes are used for the axial ion confinement. The endcap electrode separation is 6 mm. The endcap electrodes have 500 μm openings in order to provide laser access to the trapped ions exactly along the trap axis. This feature simplifies the alignment of laser beams with ions located along the trap axis.

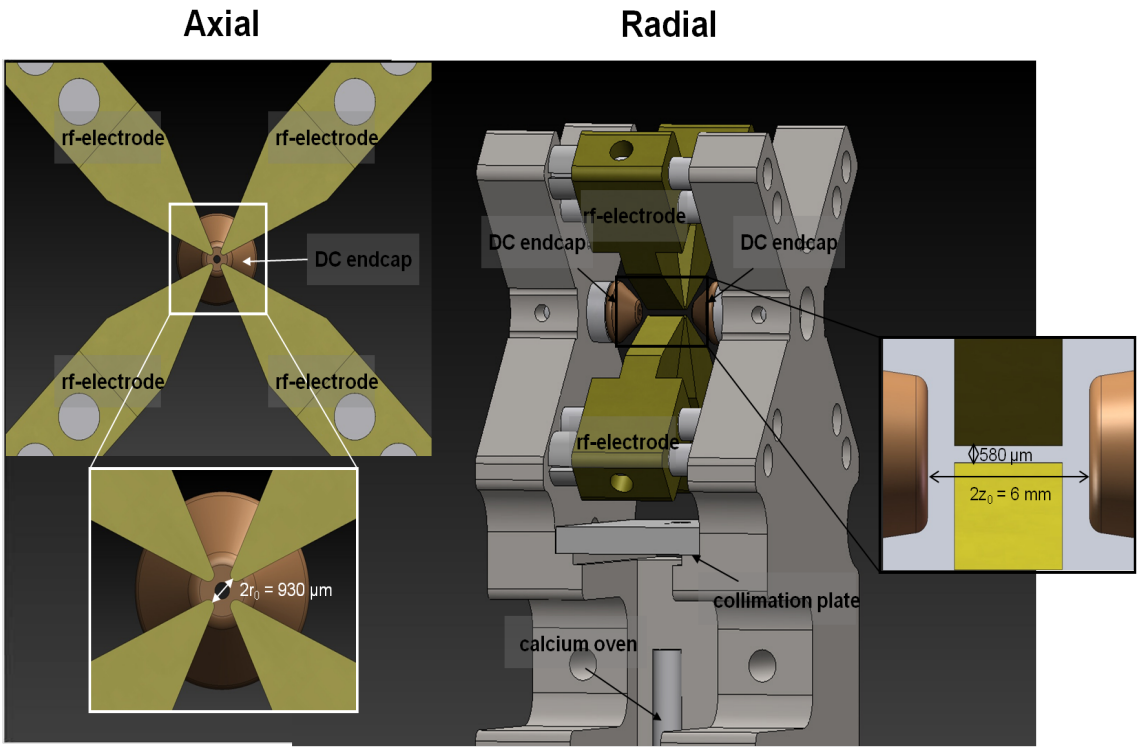

Figure 4.1: Three-dimensional model of the ion trap. The inset shows the radial plane when viewed along the trap axis. The trap mount and electrodes are machined from a single block of stainless steel. Ceramic spacers are used to electrically insulate the electrodes from the mount structure. The separation of adjacent rf-electrodes is 580 μm and the distance from the centre of the trap to each rf-electrode is 465 μm. The DC endcap electrode separation is 6 mm. Each endcap electrode has a 500 μm opening to provide laser access along the trap axis. An oven, serving as the source of neutral calcium atoms, is mounted below the trap.

4.1.1 Vacuum system

The trap is contained and operated within an UHV environment. A cube shaped stainless steel chamber houses the ion trap. Four sides of the chamber have 75 mm diameter windows allowing optical access along the trap axis and in the radial plane. The top window, with a diameter of 35 mm, is designed to provide optical access for the imaging system, which is suspended above the chamber.

The chamber is mounted onto a reducing-cross with four UHV compatible feedthrough ports. These include a sub-D feedthrough for supplying current to the atomic oven source, a two-pin high voltage feedthrough for supplying DC potentials to the two endcap electrodes, a four-pin high voltage feedthrough for connecting the rf-electrodes and an UHV valve for the optional connection of a turbomolecular pump.

A bellows connects the chamber and cross to an ion pump[1]. The ion pump is used to

[1]Kurt J. Lesker LION 303

maintain a typical vacuum system operating pressure on the order of 10^{-11} mbar. The pressure within the vacuum system can be measured from the current across the ion pump electrodes during operation.

The reducing-cross is bolted to an aluminum breadboard mounted in a cut-away section of a floating optical table. The chamber is positioned so that the centre of the side window is positioned 100 mm above the surface of the optical table. The bellows and ion pump are supported from below and bolted to the underside of the optical table. This design couples the ion trap and optical components to the same vibrationally isolated table surface.

In order to achieve the desired operating pressure, care must be taken when reducing the system pressure down from atmospheric pressure. A turbomolecular pump, backed by a rotary pump, is connected to the sealed system through the UHV valve in the four-way-cross. After a few hours of pumping with the turbomolecular pump, the system pressure is typically on the order of 10^{-7} mbar. Next, the system is 'baked' in order to remove contaminants from the interior surfaces and ensure that a sufficiently low pressure can be achieved. Heating elements are connected to the outside of the vacuum system, around each of the flanges and on the chamber. The temperature of the entire system is slowly, typically over the course of 48 hours, raised to 200 degrees Celsius. The temperature is monitored using several thermistors fixed to the outside of the vacuum system. Due to the variety of materials within the vacuum system and corresponding variety of thermal expansion coefficients, temperature gradients increase the risk of damaging components. This is a particularly important consideration in the regions surrounding the window ports. Slowly raising the temperature reduces the risk of producing harmful gradients. The baking temperature is maintained for typically five days. Near the end of the baking period the ion pump is activated in order to remove contaminants from the pump electrodes. Similarly, a current is supplied to the calcium oven to remove contaminants and oxides from the surface layer of calcium. Finally, with the ion pump activated, the turbomolecular pump is disconnected from the system by closing the UHV valve and the temperature is slowly returned to room temperature.

4.1.2 Calcium oven

Rather than implementing the PLA loading scheme described in chapter 3, a resistively heated oven is used as the source of neutral calcium atoms in order to create an experimental set-up suitable for studying charge exchange reactions (see chapter 7). The oven is identical in design to the one described in chapter 3. The tantalum tube is mounted

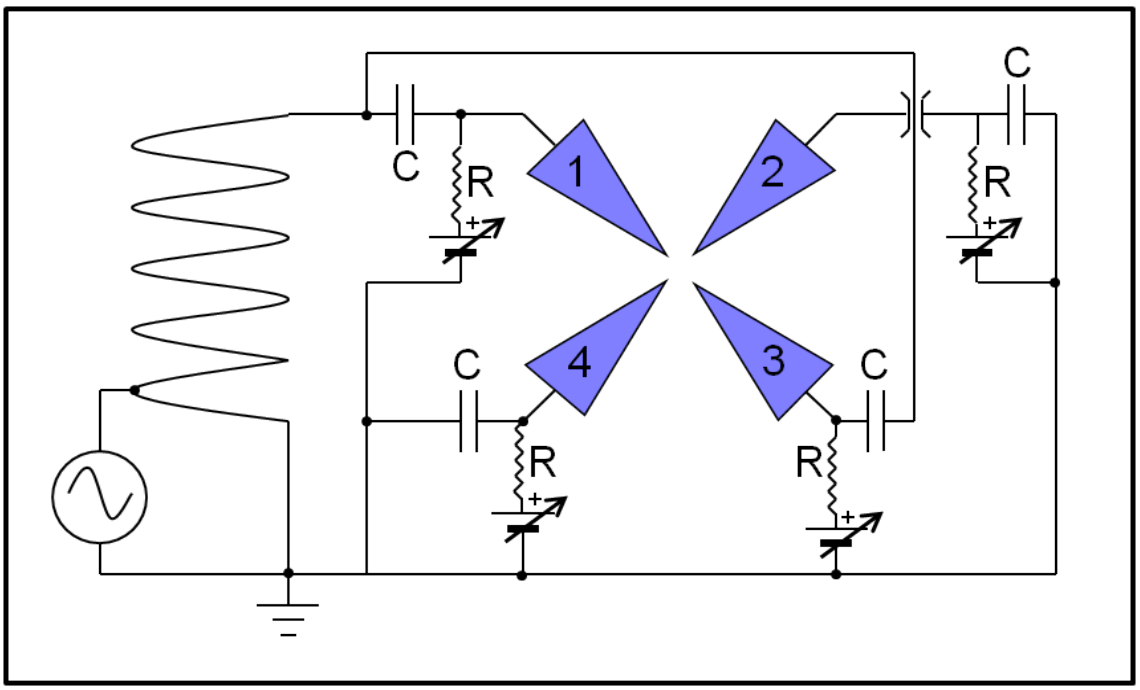

Figure 4.2: Schematic showing the rf-drive circuit. An auto-transformer amplifies the input rf-signal, which is applied to rf-electrodes one and three. Electrodes two and four are kept at rf-ground. An RC circuit is used to superimpose a DC-signal onto each rf-electrode. The DC-potentials are used for compensating stray electric fields. In each instance R=25 kΩ and C=8.2 nF.

approximately 25 mm below the centre of the ion trap and electrically isolated from the trap structure (see Fig. 4.1). An aluminium plate with a 250 μm hole concentric with the line passing through the centre of the trap and the center of the tantalum tube serves as a collimator for the atomic beam. The opening of the calcium oven is positioned approximately 7 mm from the collimation hole. Typical operating powers of 1-2W give oven temperatures on the order of 500 K.

4.1.3 Trapping potentials

Fig. 4.2 shows a schematic of the circuit used to apply the rf-signal to the trap electrodes. An auto-transformer is used to amplify the signal from the driving source, which is the direct output of a function generator[2]. The coil, resistors and capacitors are contained in an aluminium housing mounted directly onto the vacuum system high voltage feedthrough flange. A photograph of the set-up is shown in Fig. 4.3. Each trap electrode is connected to a high voltage feedthrough wire. The driving rf-signal is applied to two diagonally opposed electrodes (electrodes one and three in Fig. 4.2), which can be modeled by a capacitor in

[2]SRS DS345 30MHz synthesized FG

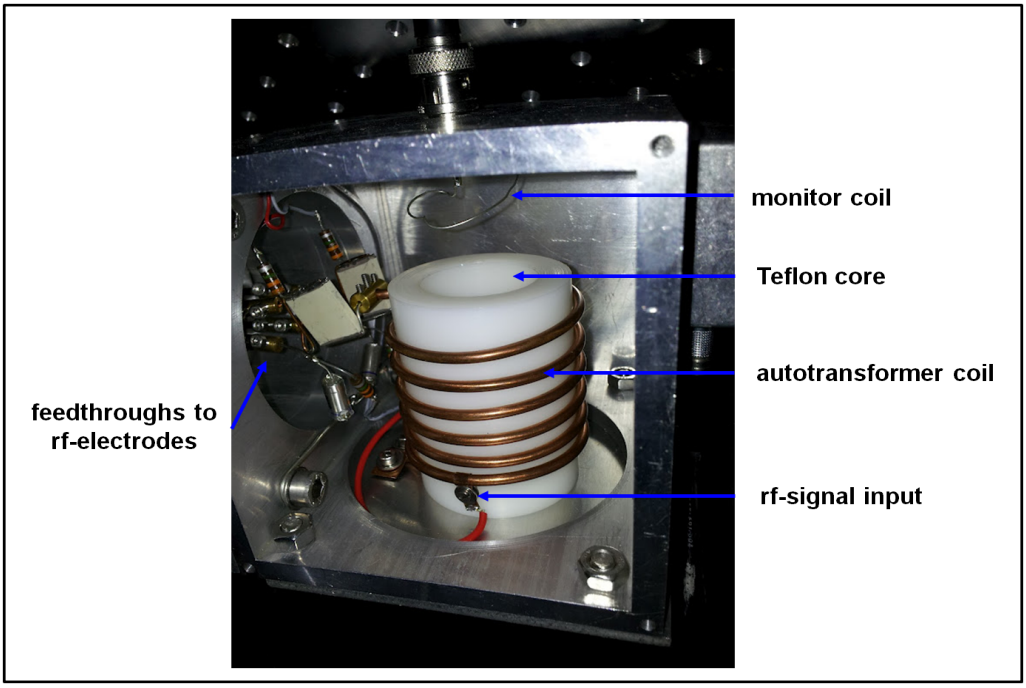

Figure 4.3: Photograph of the rf-drive circuit contained in an aluminium housing mounted to the high voltage feedthrough flange on the vacuum system. The input rf-signal is amplified by the autotransformer and coupled to two of the rf-electrode feedthroughs by an RC circuit. The remaining two feedthrough connections are kept at rf-ground. A single loop of wire is used as a monitor coil.

a series LCR circuit. The other two electrodes (electrodes two and four) are kept at rf-ground. The impedance matching of the rf-source to the circuit is determined by the point of contact with the auto-transformer coil. This is optimised by monitoring the transmitted and reflected rf-power with an rf-reflectometer (in series with the driving source) while adjusting the contact point of the source with a sliding fastener. For optimised impedance matching, the circuit has a measured quality factor of 155(5) for the resonance frequency of 29.579 MHz. We have empirically found that the circuit has approximately the same resonance frequency when the trap electrodes are replaced by a 15 pF capacitor. Therefore, by measuring the applied rf-power we can estimate the amplitude of the rf-voltage from the relation

$$V(P) = \sqrt{\frac{\mathrm{PQ}}{w_0 \mathrm{C}}}, \tag{4.1}$$

where P is the rf-power measured with the reflectometer, w_0 is the resonance frequency, Q is the quality factor and C is the effective capacitance of the trap electrodes (approximately 15 pF). Typical rf-powers in the range of 20 mW to 500 mW corresponding to rf-electrode voltages on the order of several hundred volts.

DC-voltages may be applied independently to each of the four trap electrodes in order

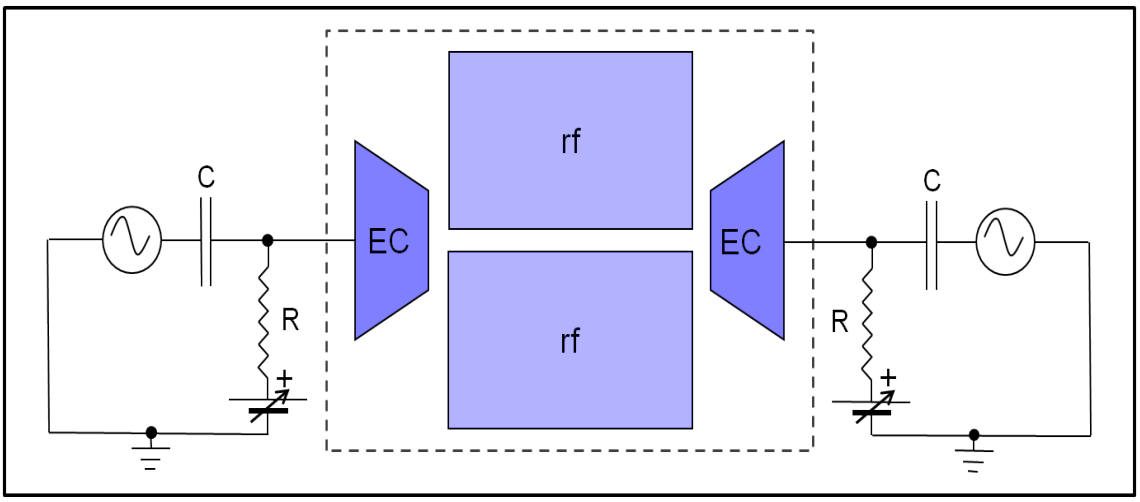

Figure 4.4: Schematic of the circuit used for applying the axial confining potential to the endcap (EC) electrodes. The dashed line indicates the interior of the vacuum system. An RC circuit is used to superimpose rf-signals, for exciting the secular motion of the ion, with the DC confining potential. In each instance R=25 kΩ and C=8.2 nF.

to compensate stray electric fields and position the ion at the centre of the rf-potential. The DC-signal is superimposed onto the rf-signal with a resistor and capacitor (see Fig. 4.2). Each DC source is an analogue output voltage from a computer controlled DAQ[3].

The endcaps electrodes are used to create the confining potential along the trap axis. Positive voltages are applied to each of the two endcaps using a pair of high voltage DC sources[4]. Fig. 4.4 shows the endcap electrode circuit. Each endcap is connected to a high voltage feedthrough wire and positive potentials of up to 3000 V may be applied to the endcaps, limited only by the electric breakdown of the circuitry located outside the vacuum chamber. The secular motion of the ions may be excited by external rf-signals, which are applied independently to each of the endcap electrodes by superimposing the rf and DC-signals with an RC circuit. The RC circuit is contained in an aluminium housing mounted on the high voltage feedthrough flange outside the vacuum system.

4.1.4 Imaging system

Ion fluorescence is collected by a microscope objective[5] with x10 magnification and a numerical aperture of 0.22. A photograph of the imaging system is shown in Fig. 4.5. The objective is mounted onto a two-dimensional translation stage on top of the chamber where the window port allows it to be positioned 46 mm, the working distance of the

[3]National Instruments USB-6229
[4]SRS PS350/5000V-25W
[5]Nikon MM series 210 mm tube length

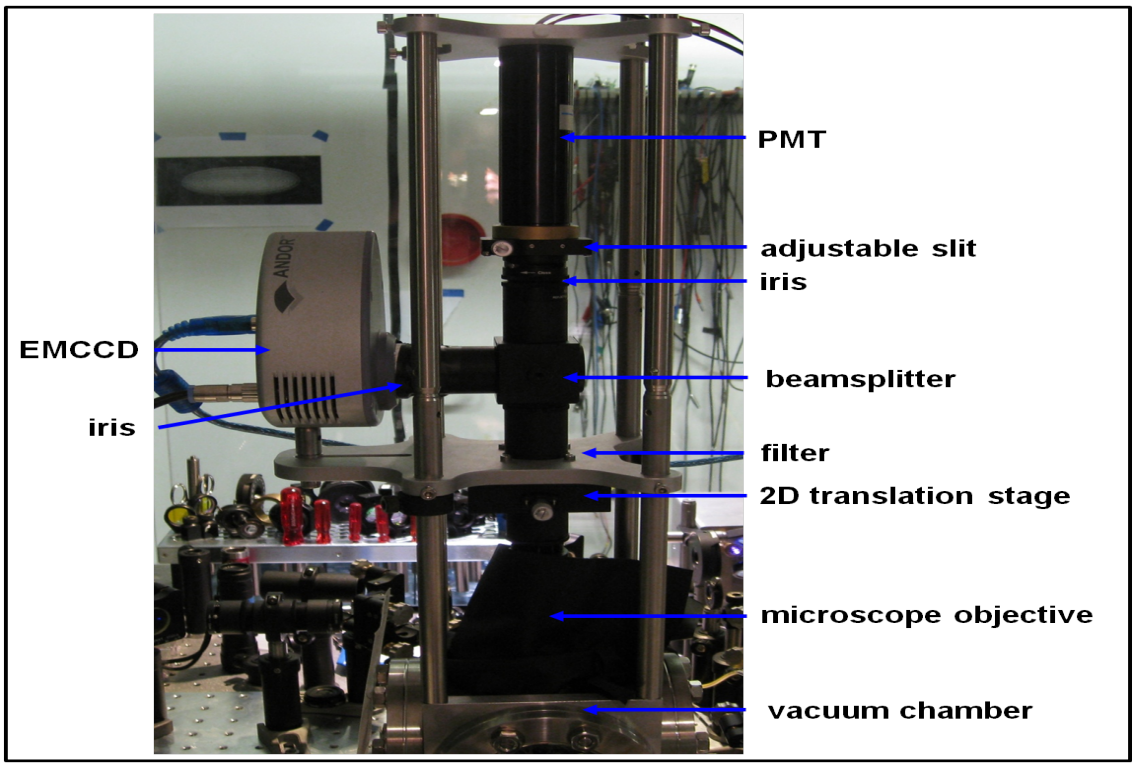

Figure 4.5: Photograph of the imaging system mounted above the vacuum chamber. Ion fluorescence is collected with a x10 objective lens. The image is then divided by a beamsplitter. 8% of the incident light is reflected to the EMCCD and the remaining 92% is transmitted to the PMT. A slit and iris are positioned in front of the PMT to eliminate laser scatter from the trap electrodes.

objective, from the centre of the ion trap. An adjustable lens tube is used to optimise the vertical position of the objective. The light collected by the objective is passed through an optical filter[6], which transmits >85% of light at the wavelength of the ion fluorescence and <0.1% of light at the other laser wavelengths used. A sharp image of the trap centre is formed 200 mm behind the objective. The image is split by a beamslitter[7] which reflects 8% of the light and transmits 92% of the light. The images follow equal path lengths to a single photon EMCCD[8] and a PMT. Along the transmitted path, an adjustable slit is position at the location of the sharp image and used to cut light scattered from the trap electrodes. The PMT is mounted immediately behind the slit. Along the reflected path, the sharp image is formed on the surface of the EMCCD chip. The ion fluorescence collection efficiency of the system is estimated to be 0.1%.

[6]Semrock BrightLine single-band bandpass filter FF01-395/11-25
[7]Thor Labs Cube-Mounted Pellicle Beamsplitter, 8:92
[8]Andor Luca S

4.2 Laser system

All of the lasers used for photo-ionising neutral calcium and for Doppler cooling trapped calcium ions in the experiments described in this work are external cavity diode lasers. Each laser is installed within an in-house designed mount. Feedback to the laser diode is provided by an optical grating in the Littrow configuration. The laser is coarsely tuned to the desired frequency by adjusting the grating angle, the current through the diode and its temperature. Fine tuning of the frequency and frequency scanning is achieved by applying a voltage to a piezoelectric actuator controlling the tilt angle of the optical feedback grating.

The frequency of each laser is continuously monitored during operation by a wavemeter[9] with an absolute accuracy of 60 MHz. A computer controlled frequency lock is employed by applying proportional-integral feedback to the laser grating piezoelectric actuator based on the error signal of the wavemeter.

Each laser is delivered to the experiment through a single-mode polarisation maintaining fibre. The fibre acts as a spatial filter for the light and serves to decouple the laser system, which is isolated on an optical table, from the experiment, which is located on a separate optical table.

4.2.1 Photo-ionisation lasers

The first stage photo-ionisation light at 423 nm is generated through SHG within a custom designed periodically poled waveguide crystal[10]. The fundamental light, at 846 nm, is produced by a laser diode[11]. The 846 nm laser diode frequency and output power are controlled by adjusting the diode laser temperature, current and the angle of the optical feedback grating. The 846 nm light is coupled into the waveguide via a pigtailed single mode fibre. The efficiency of the frequency doubling is strongly dependant on the crystal temperature, since this determines the phase matching of the SHG light. The length of the waveguide is controlled by a temperature stabilised oven. During typical operation, 30 mW of 846 nm light is coupled into the waveguide and approximately 250 μW of 423 nm light is measured at the output.

The second stage photo-ionisation light is supplied by the laser diode at 375 nm, which has been described in Sec. 3.2.2.

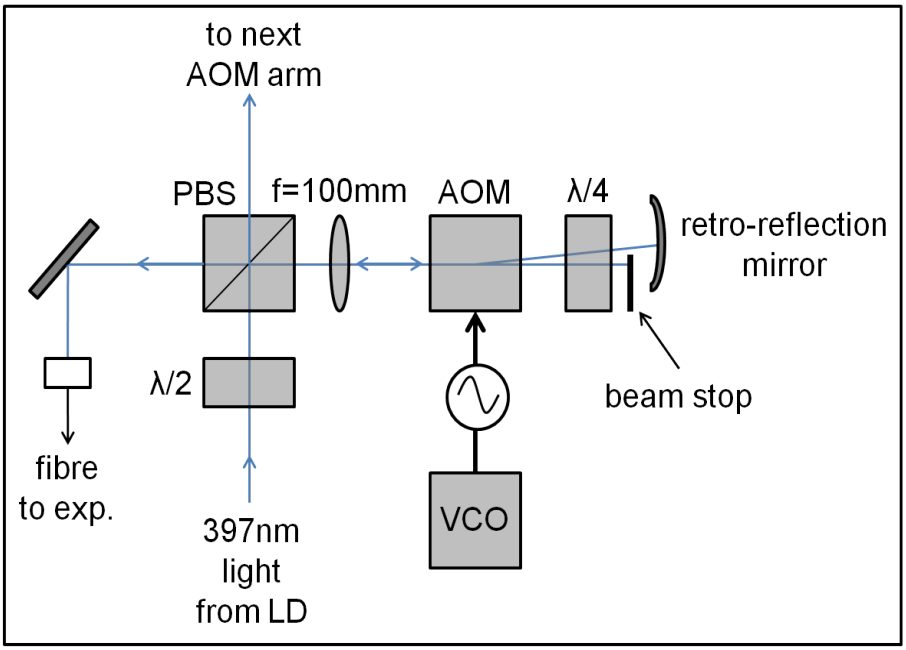

Figure 4.6: Double pass AOM set-up for the 397 nm laser. A portion of light is reflected by the PBS and sent to the AOM. The zeroth-order diffracted beam is blocked by a beam stop while the first order diffracted beam is retro-reflected back through the AOM. Two passes through the $\lambda/4$ waveplate ensures that the return beam acquires an orthogonal linear polarisation relative to the input beam. The double frequency shifted return beam is transmitted through the PBS where it is coupled into a single-mode polarisation maintaining fibre and sent to the experiment.

4.2.2 Doppler cooling laser

The 397 nm laser diode was manufactured by Toptica[12]. During typical operation it has an output power of 3 mW. The elliptical output beam is aligned through an optical isolator and circularised with a cylindrical lens pair. A glass wedge plate is used to deflect around 4% of the beam, which is coupled into a multi-mode fibre and sent to the wavemeter. A portion of the primary beam is directed to a double-pass AOM[13] set-up via a $\lambda/2$ waveplate and a PBS. A schematic of the set-up is shown in Fig. 4.6.

The AOM is aligned such that the first-order diffracted beam has a positive frequency shift relative to the zeroth-order diffracted beam. The zeroth-order diffracted beam is blocked by a beam stop and the first-order diffracted beam is retro-reflected back through the AOM. After two passes through the $\lambda/4$ waveplate, the output beam acquires a linear polarisation orthogonal with respect to the input beam. The return beam is therefore

[9] HighFinesse wavelength meter WS-7
[10] HC Photonics
[11] Eagleyard Photonics
[12] Toptica series DL100
[13] Crystal Technologies model 3200

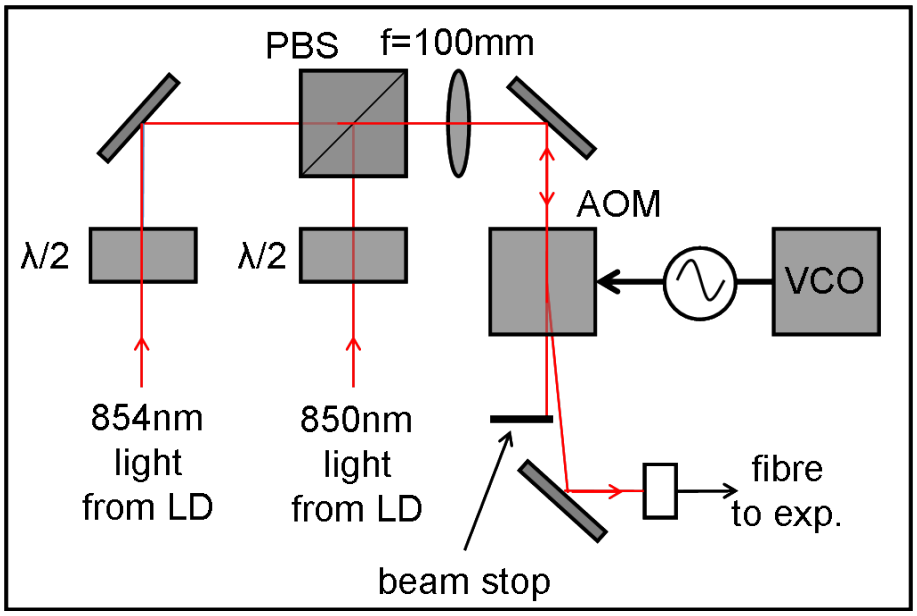

Figure 4.7: Single-pass AOM set-up used for the 850 nm and 854 nm lasers. The two laser beams are overlapped at a PBS with linearly orthogonal polarisations and aligned through an AOM. The power of both lasers can be controlled by adjusting the amplitude of the VCO signal. The overlapped beams are coupled into a single mode polarisation maintaining fibre which maintains the polarisation of both beams simultaneously.

transmitted through the PBS. The beam is then coupled into a single-mode polarisation maintaining fibre and sent to the experiment.

The AOM is controlled by a VCO[14]. The set-up allows the laser frequency of the first-order diffracted beam to be scanned by controlling the frequency of the VCO signal. During frequency scanning, the coupling into the single mode fibre is not affected since any change in the laser beam path during the first pass through the AOM is reversed during the second pass. The frequency of the output beam is adjustable between approximately +300 MHz and +500 MHz with respect to the input beam. In addition, the power of the output beam can be controlled over the full range by adjusting the amplitude of the VCO signal. Both the frequency and amplitude of the VCO signal are controlled by analogue voltages from a computer controlled DAQ. The modular nature of each double-pass AOM arm allows for several separate 397 nm laser beams each with independent control of the laser power and frequency.

4.2.3 Re-pump lasers

The laser diodes used for re-pumping were supplied by Eagleyard. By adjusting the feedback grating as well as the diode current and temperature, the lasers are tuned to

[14]Crystal Technologies model 1200AF-AEF0-1.0W

850 nm and 854 nm respectively. When optimised, each laser has an output power of around 20 mW at the desired frequency.

The 850 nm and 854 nm lasers are used for re-pumping via the $4P_{3/2}$-state, as discussed in Sec. 2.2.3. Each laser beam is aligned through an optical isolator before a small fraction of light is deflected from the primary beam with a glass wedge plate and sent to the wavemeter. The two primary beams acquire mutually orthogonal polarisations with a pair of $\lambda/2$ waveplates and are overlapped at a PBS. The overlapped beams are aligned through an AOM and the first-order diffracted beam is coupled into a polarisation maintaining fibre. The zeroth-order diffracted beam is blocked by a beam stop. The set-up is shown in Fig. 4.7.

The AOM is used to simultaneously control the power of both lasers in this set-up. By adjusting the amplitude of the VCO signal with the computer controlled DAQ, the power in the first-order diffracted beam can be adjusted over the full range. Frequency scanning is not possible in this set-up since changes in the laser beam diffraction angle would compromise the coupling efficiency into the single mode fibre.

The polarisation of both overlapped laser beams is maintained within the fibre provided one of the beams is aligned with the polarisation maintaining axis of the fibre. The polarisation of the second beam, orthogonal to the first, is maintained too since the fibre prevents mixing between the two linear polarisation states.

4.3 Trap loading

A schematic showing the alignment of the photo-ionisation and Doppler cooling lasers is shown in Fig. 4.8. To create calcium ions, neutral calcium atoms are photo-ionised in the centre of the trap. A flux of neutral calcium atoms is produced by passing a current through the resistively heated oven. The 423 nm and 375 nm photo-ionisation lasers are overlapped with a PBS and aligned along the trap axis. The beams are focused with a single convex lens down to a waist of approximately 100 μm at the centre of the trap. The 423 nm laser has a typical power of 50 μW and the 375 nm laser has a typical power of 1 mW. Neutral calcium atoms pass through the focused pair of photo-ionisation lasers and are ionised with high probability in the trapping region between the rf-electrodes.

Ions created in the centre of the trap are radially confined by the quadrupole electric potential and confined along the trap axis by the axial potential. Typically, an rf-signal with a power of 100 mW is applied to the rf-electrodes giving a radial frequency on the

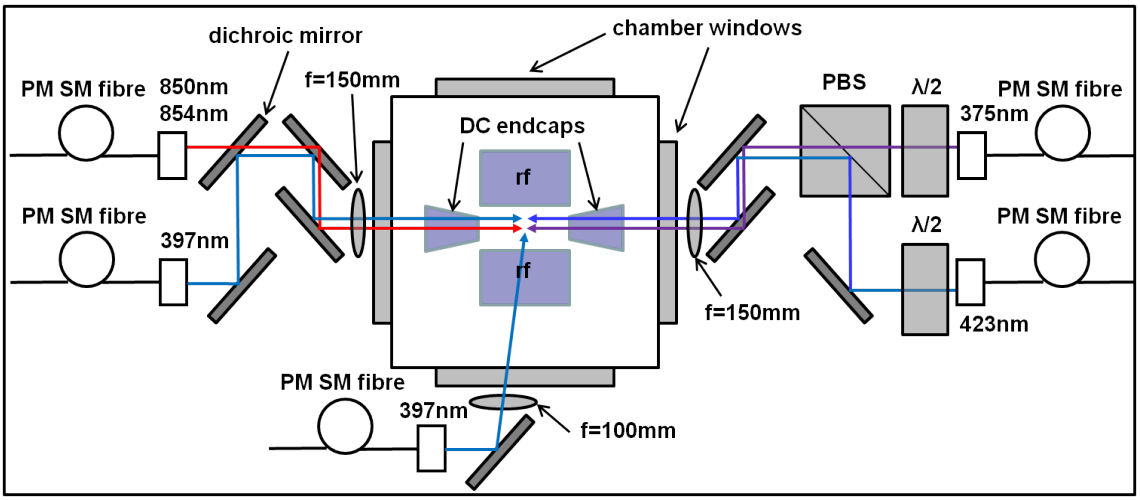

Figure 4.8: Top view of the experimental chamber showing the alignment of the photo-ionisation and Doppler cooling lasers. Both sets of lasers are aligned along the trap axis and focused with convex lenses. The overlapped beams are offset in the schematic for clarity. An additional 397 nm laser beam is aligned in the radial plane.

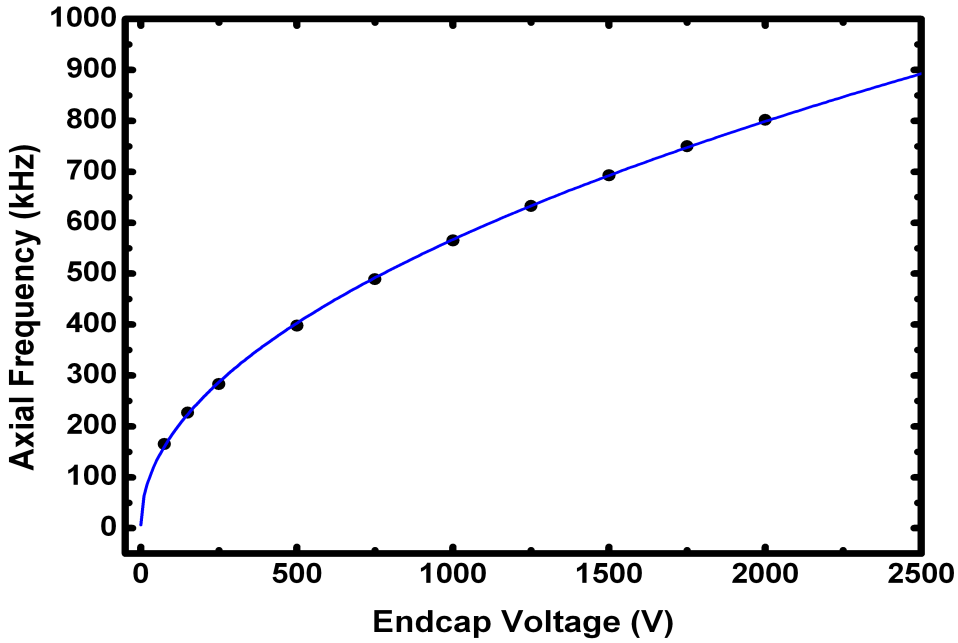

Figure 4.9: The axial frequency of a single ion as a function of the voltage applied to the DC-endcap electrodes. Equ. 2.14 has been fit to the data (solid line).

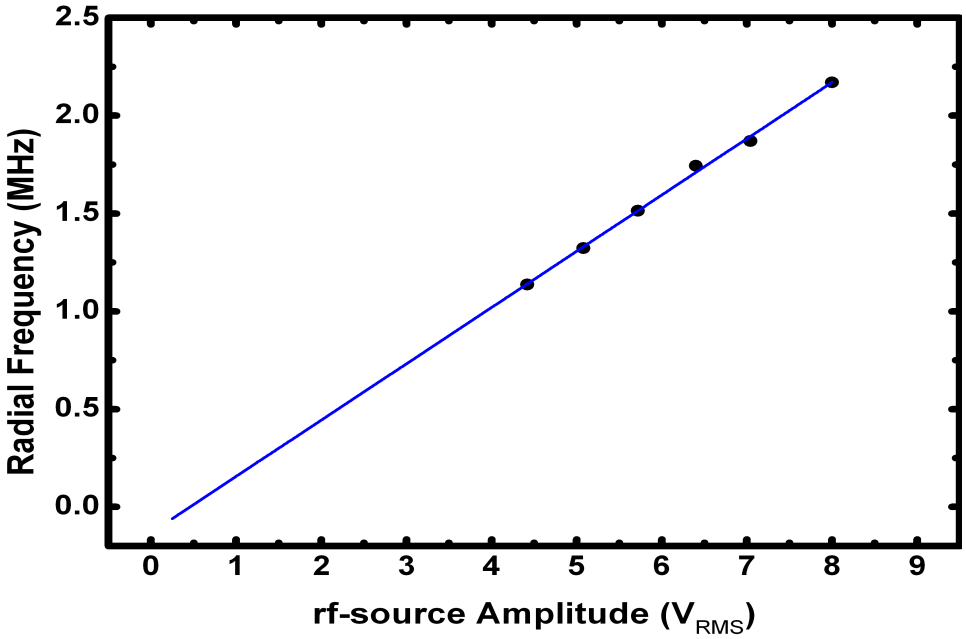

Figure 4.10: The radial frequency of a single ion as a function of the rf-voltage source amplitude. Equ. 2.10 has been fit to the data (solid line). Since the a parameter is small, the relationship between the rf-source amplitude and the radial frequency is approximately linear.

order of 1 MHz. A DC-potential in the range between 100 V and 2000 V is applied to each of the endcap electrodes giving an axial frequency on the order of 100 kHz.

The 397 nm, 850 nm and 854 nm lasers are used for Doppler cooling the ion(s) in the trap centre. The 850 nm and 854 nm lasers are out-coupled from a single fibre and overlapped with the 397 nm laser at a dichroic mirror. The three overlapped lasers are aligned along the trap axis counter-propagating with respect to the photo-ionisation lasers (see Fig. 4.8). The lasers are focused by a single convex lens down to a waist of approximately 70 μm at a focal point located at the centre of the trap. A second 397 nm laser beam is aligned in the radial plane to ensure efficient cooling of all directions of motion of the ion(s). The radial laser is aligned with an angle of 76° with respect to the trap axis and is focused to a waist of approximately 50 μm at the centre of the trap with a single convex lens. The 850 nm and 854 nm lasers have powers between 1 mW and 2 mW resulting in the saturation of the $3D_{3/2} \rightarrow 4P_{3/2}$ and $3D_{5/2} \rightarrow 4P_{3/2}$ re-pump transitions respectively. The axial 397 nm laser power is typically set between 10 μW and 150 μW depending on the size of the ion crystal being loaded. The radial 397 nm laser power is set between 1 μW and 5 μW. The ratio of the axial and radial 397 nm laser powers is adjusted such that the majority of the fluorescence is generated by the axial laser but enough radial cooling is provided for good localisation of the ions.

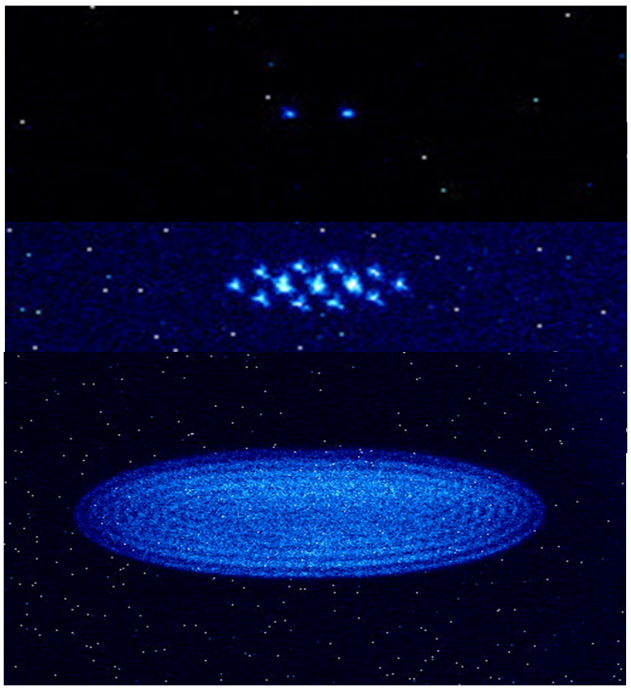

Figure 4.11: EMCCD images of a two ion string, a small crystal containing around ten ions and a large crystal containing several hundred ions. Each picture is taken with a different resolution.

Single ions, linear ion strings and large three-dimensional ion crystals can be rapidly and reliably loaded into the trap. For an oven power of 2.5 W, a single ion is typically loaded after approximately 30 seconds of oven operation. As the oven approaches its constant operating temperature (around 500 K), the ion loading rate increases. Ion crystals containing tens of ions can be loaded in around 60 seconds and large crystals containing hundreds of ions can be loaded after a few minutes. For a reduced axial confinement and increased radial confinement, long one-dimensional ion strings are formed along the trap axis. With a larger axial confinement and reduced radial confinement, three-dimensional cigar-shaped ion crystals form. Fig. 4.11 shows EMCCD images of typical trapped ion crystals.

To coarsely measure the ion's secular frequency, an rf-signal is superimposed onto a nearby electrode. The frequency is scanned and when the excitation frequency approaches the secular frequency a resonant excitation of the ion's motion occurs. This motion is observed with the EMCCD or by monitoring changes in the ion's fluorescence with the PMT. Fig. 4.9 shows the axial frequency of a single ion as a function of the applied DC-endcap voltage. Equ. 2.14 has been fit to the data (solid line). The axial frequency increases with the square root of the DC-endcap voltage. Fig. 4.10 shows the radial frequency of a single ion as a function of the rf source voltage. Equ. 2.10 has been fit to

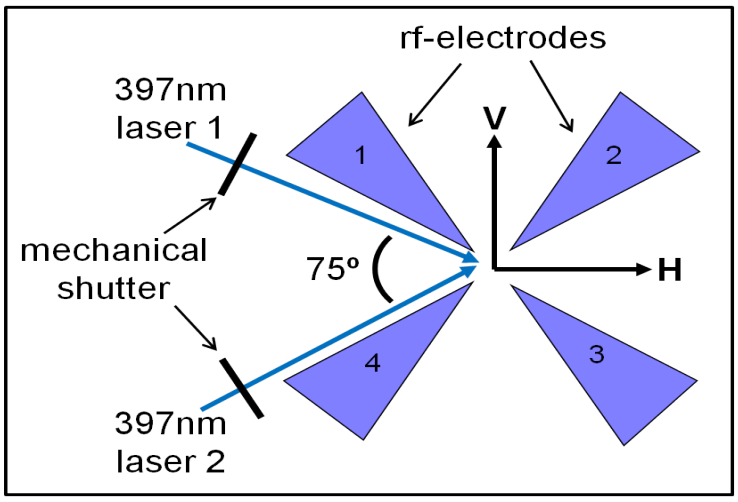

Figure 4.12: The radial plane viewed from the trap axis. DC-compensation voltages applied to the rf-electrodes change the ion's position in H-V space. The origin of the H-V coordinate system is the location of the trapped ion when all rf-electrodes are DC-ground. Two 397 nm laser are aligned in the radial plane with an angle of 75 degrees between them. Each laser can be blocked by a mechanical shutter.

the data (solid line). Since the a parameter is small, the relationship between the rf-source amplitude and the radial frequency is approximately linear. Chapters 6 and 8 describe improved techniques for precisely measuring the secular frequency of trapped ions.

4.4 Micromotion minimisation

Micromotion is an oscillatory motion of the ion driven by the rf trapping field. It is an intrinsic property of ions confined in a quadrupole potential (see Sec. 2.1). For a single ion, the micromotion amplitude can be minimised by positioning the ion at the centre of the rf-potential. However, even small spatial deviations of the ion from the centre of the rf-potential can lead to large amplitude micromotion which induces heating and compromises efforts to precisely localise the ion. Shifts in ion position with respect to the centre of the rf-potential are caused by stray electric fields. Examples of stray electric fields include charges built up on dielectric surfaces near the trap or 'patch-potentials' located on the surface of the trapping electrodes. The exact source of the stray fields may not be known and they may vary on time scales of hours or days.

By manipulating the DC-compensation voltages on the rf-electrodes, the stray electric fields can be compensated such that the ion is positioned at the centre of the rf-potential. Fig. 4.12 shows the radial plane when viewed along the trap axis. A coordinate system labelled H (horizontal) and V (vertical) has been assigned to describe the location of the ion

in the plane. The origin of the coordinate system is the location of the trapped ion when all four rf-electrodes are DC-grounded. Since the quadrupole field in the linear trap is two-dimensional, the micromotion of the ion will be confined to this plane. Equal amplitude DC-compensation voltages applied to electrodes 1 and 4 will shift the ion in the positive H-direction with the ion's V-coordinate remaining constant. Likewise, equal amplitude voltages applied to electrodes 3 and 4 will shift the ion in the positive V-direction while maintaining a constant H-coordinate.

4.4.1 Coarse micromotion minimization

The ion's micromotion can be coarsely minimised by modulating the magnitude of the rf-potential while observing the resulting motion with the EMCCD. Switching between a low rf-potential and a high rf-potential 'opens' and 'closes' the radial confinement. If external electric fields within the trap are not fully compensated, the ion will be pushed away from the trap centre as the radial confinement is reduced. For a modulated rf-potential in the presence of uncompensated stray electric fields, the ion's position will oscillate. While observing this effect with the EMCCD, the DC-compensation voltages can be manually adjusted until the ion's position becomes independent of the applied rf-potential modulation. This technique works very well for minimising the micromotion in the image plane but the modulation of the ion's position in the direction perpendicular to the image plane is not easily observable. If two cameras are used, with image planes perpendicular to one another, better results are achieved. However, this is an experimentally cumbersome process and higher accuracy can be attained in a much shorter time using the photon correlation technique.

4.4.2 Photon correlation technique

For an ion experiencing micromotion, there is a correlation between photon scattering events and the phase of the rf-potential for a fixed 397 nm laser alignment and frequency. This correlation is due to the linear Doppler effect. During each half-cycle of motion, the ion moves either parallel or anti-parallel with the laser thus decreasing or increasing the scattering rate. By recording photon arrival times with respect to the phase of the rf-potential, the amplitude of the ion's driven motion collinear with the propagation direction of the laser can be measured [43]. However, the component of the ion's driven motion orthogonal to the propagation direction of the laser cannot be measured. By employing two 397 nm lasers, each aligned in the radial plane of the trap and with a large angle

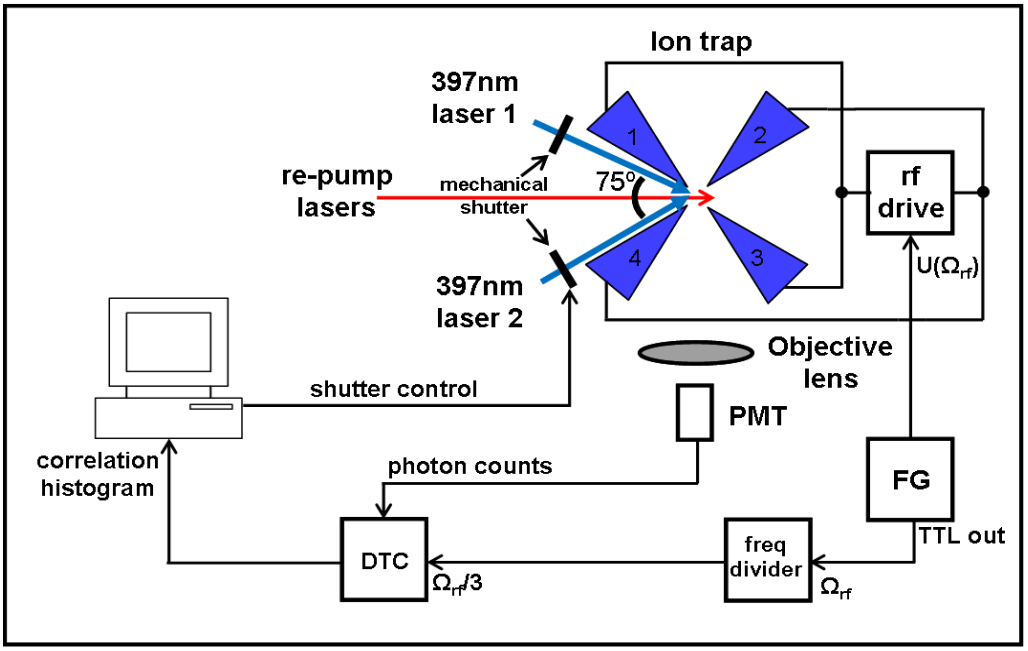

Figure 4.13: Experimental set-up used for measuring the ion's micromotion amplitude with the photon correlation technique. Both radial 397 nm lasers have individual computer controlled shutters. Photon counts and the rf-drive signal are cross correlated with the TDC card. The correlation histogram reveals the sinusoidal motion of the ion at the trap frequency Ω_{rf}.

between them, both components of the ion's micromotion amplitude can be measured. Since the radial potential is two-dimensional, only two lasers are needed.

Fig. 4.13 shows a schematic of the experimental set-up used for measuring the ion's micromotion. The two radially aligned 397 nm lasers have an angle of 75 degrees between them. Both lasers also have a small component in the axial direction. In order to measure one component of the ion's micromotion, the ion is interrogated by one of the lasers while the other is blocked by a mechanical shutter. During a measurement the ion is re-pumped by the axial 850 nm and 854 nm lasers with the axial 397 nm laser switched off (See Fig. 4.8). The photon signal from the PMT and the TTL output from the rf-source function generator, which is in-phase with the rf-potential, are connected to a TDC with nanosecond resolution[15]. A cross correlation is created by recording the time delay between each detected photon and the subsequently detected TTL pulse from the rf-source. The trigger signal from the rf-source is divided by a factor of three prior to being counted using a frequency divider so that three periods of the ion's micromotion are visible in the histogram. A sine function is fit to the histogram with a frequency equal to $\Omega_{\mathrm{rf}}/3$ and an amplitude proportional to the ion's micromotion amplitude.

[15] ACAM TDC-GP2 2-channel Universal Time-to-Digital Converter

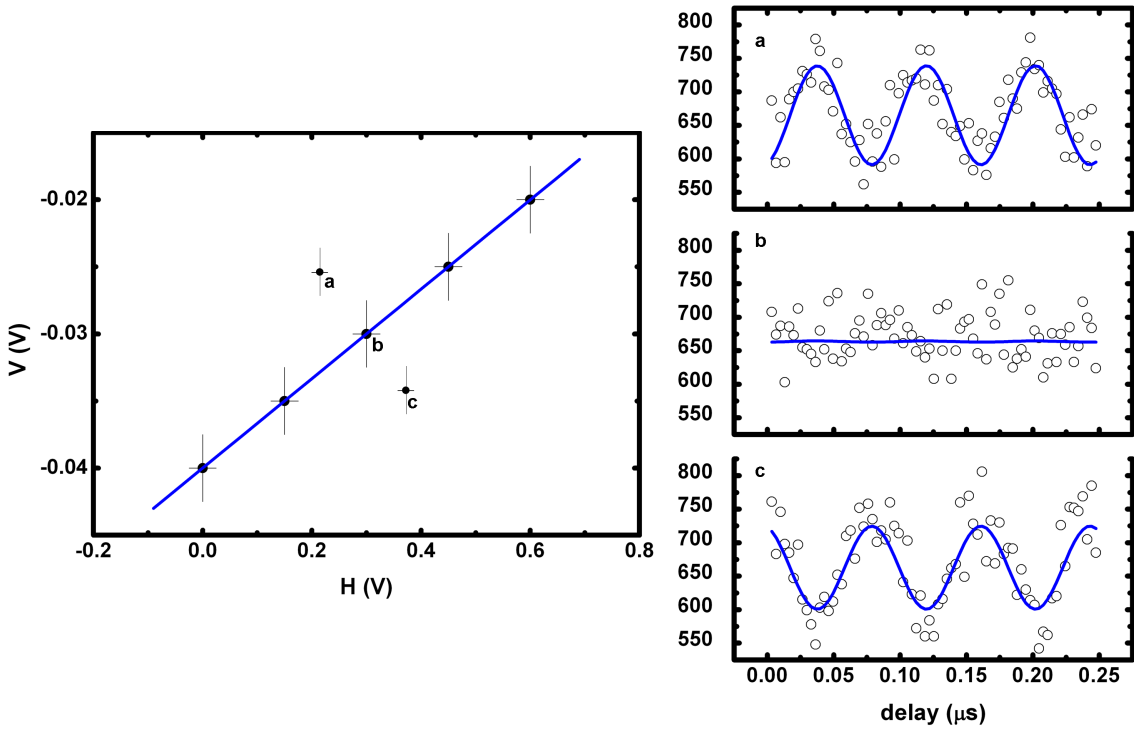

Figure 4.14: *Left*: Five points of micromotion minimum in H-V space measured using one of the radial lasers. The H-V coordinates of the ion are in units of the voltage on the DC-compensation electrodes. Each data point is the mean amplitude of ten cross-correlation histograms and the error bars are the standard deviation each data set. A linear function (solid line) has been fit to the data. *Right*: Cross-correlation histograms for three points in H-V space. A sine function has been fit to each histogram (solid lines). The ion has a large micromotion amplitude at points (a) and (c). The micromotion amplitude is minimised for DC-compensation voltages positioning the ion at point (b).

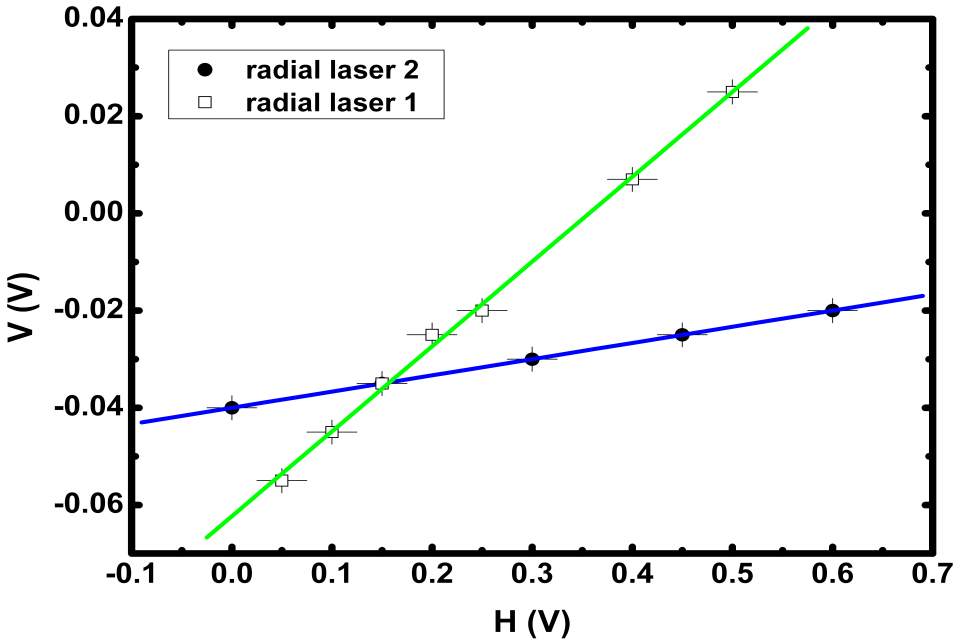

Figure 4.15: The lines of micromotion minimum measured independently with both radial lasers. The point of intersection of the lines corresponds to the DC-compensation voltages that position the ion at the centre of the rf-potential.

The entire H-V space is mapped in small steps by applying DC-voltages to the rf-electrodes, measuring the cross-correlation histogram and recording the coordinates where the ion's micromotion amplitude is minimised. Fig. 4.14(left) shows the H-V coordinates giving minimum micromotion amplitude for one of the radial 397 nm lasers. H and V are in units of the DC-compensation voltages applied to the rf-electrodes. The points of minimum micromotion amplitude lie on the straight line corresponding to the propagation direction of the laser. Fig. 4.14(right) shows the cross-correlation histograms recorded at three points in Fig. 4.14(left). Compensation voltages positioning the ion at point (b) give minimum micromotion amplitude while points (a) and (c) give a large micromotion amplitude. There is a 90 degree shift in the phase of the rf-driving force, and corresponding phase shift in the sine fit to the cross-correlation histogram, when the ion moves from point (a) to point (c) through the point of minimum micromotion at (b).

The centre of the rf-potential, where both components of the ion's micromotion amplitude are minimised, must lie at some point along the line in Fig. 4.14(left). In order to find that point, the second 397 nm laser is employed. With the first laser blocked, the mapping of the H-V space is repeated with the second laser. Fig. 4.15 shows the lines of minimum micromotion for both lasers. The point of intersection gives the compensation voltage values that position the ion at the centre of the rf-potential.

The static electric field between the rf-electrodes is determined using a three-dimensional model of the trap and finite element method software[16]. The electric potential at the centre of the ion trap is 60 mV when the optimum DC-compensation voltages from Fig. 4.15 are applied.

[16]FEMLAB

Chapter 5

Spectroscopy of laser cooled calcium ions

5.1 Introduction

Spectroscopy on the $4S_{1/2} \rightarrow 4P_{1/2}$ transition at 397 nm is an important tool for studying the laser cooling and motion of trapped calcium ions. Measurements of the transition lineshape allow for the precise determination of the central frequency of the spectral line and the relative detuning of the lasers used for Doppler cooling. In addition, the Lorentzian and Gaussian contributions to the lineshape can be used to determine the magnitude of laser intensity broadening and measure the magnitude of thermal motion respectively. Furthermore, measurements of the fluorescence spectrum have been used to accurately determine the heating rate of the ion in the trap [85, 86].

The standard way to collect the fluorescence spectrum of the $4S_{1/2} \rightarrow 4P_{1/2}$ transition is to scan the frequency of the 397 nm laser over the resonance while recording the ion's fluorescence signal with a PMT. A typical fluorescence spectrum collected in this way is shown in Fig. 5.1. Cooling the ion while simultaneously collecting a fluorescence spectrum is challenging since scanning the 397 nm laser frequency changes the cooling dynamics. As the cooling laser frequency is scanned toward the centre of the transition, the Doppler cooling efficiency peaks and then rapidly decreases. The decrease in cooling efficiency leads to an increase in the temperature of the ion. At a point near the line centre the rate of heating surpasses the cooling rate resulting in a rapid loss of ion localisation. This is accompanied by a loss of the fluorescence signal as is illustrated by the sharp drop in Fig. 5.1. A Lorentzian function may be fit to the measured fluorescence spectrum to

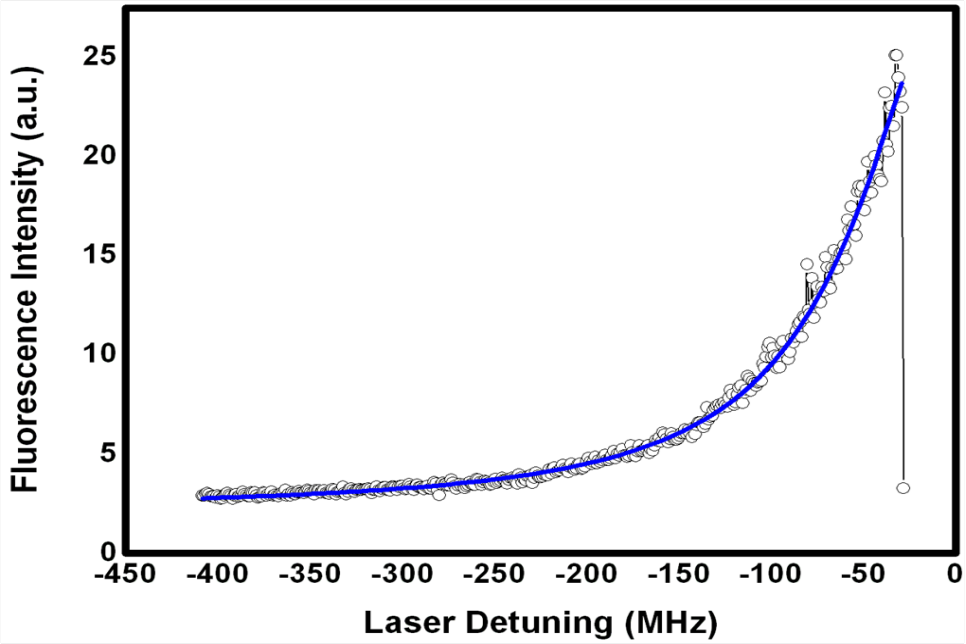

Figure 5.1: Fluorescence spectrum collected by a single 397 nm laser while simultaneously cooling the ion and scanning the laser frequency. A Lorentzian function has been fit to the data (solid line). For a 397 nm laser detuning close to the line centre the heating of the ion results in delocalisation. This manifests as a sharp drop in the fluorescence signal.

determine the line width and line centre. However, due to the restricted range of the measured fluorescence spectrum, the line centre and line width can only be determined with limited precision. As a further drawback, the ion may gain enough energy through heating effects during the frequency scan to escape from the trap. This is a particularly important consideration when shallow trapping potentials are employed.

The complications arising from the standard spectroscopy procedure described above can be removed by modifying the experimental set-up and adding a second laser at 397 nm. One of the lasers is employed to probe the $4S_{1/2} \rightarrow 4P_{1/2}$ transition while the frequency of the other laser is maintained at an optimal detuning for Doppler cooling [87]. As demonstrated in the experiment by Wolf et al., the Doppler cooling laser is periodically blocked by a mechanical shutter allowing a cloud of ions to be interrogated solely by the probe laser. Fluorescence is collected with a PMT which is gated to record only the counts occurring while the Doppler cooling laser is blocked. By scanning the frequency of the probe laser and limiting the probe interaction time for each frequency step, the entire fluorescence spectrum can be measured while keeping the ions well localised in the trap.

We have developed a spectroscopy technique similar to the method of Wolf et al. that requires only a single 397 nm laser beam, which serves both as the Doppler cooling laser and as the probe. The 397 nm laser is rapidly switched between cooling and probing by

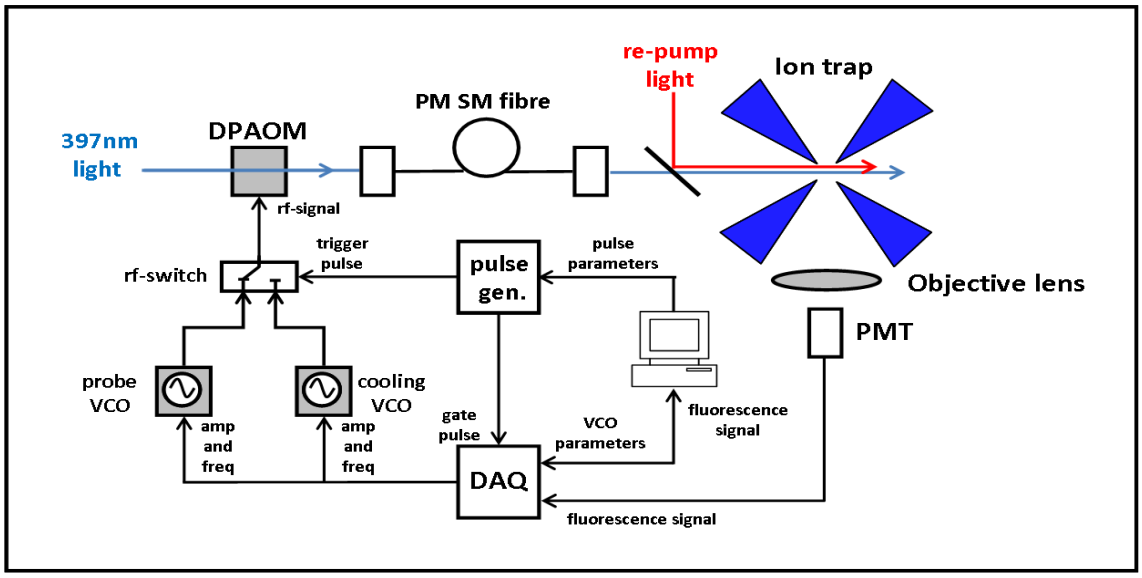

Figure 5.2: Schematic of the experimental set-up. The 397 nm light is coupled through a double-pass AOM (DPAOM) set-up before it is sent to the ion trap through a single-mode (SM) polarisation maintaining (PM) optical fibre. The rf-signal is supplied to the AOM by either of two VCOs connected through an rf-switch. A computer controlled pulse generator switches between the two VCOs by supplying a trigger pulse to the rf-switch. A gate pulse, synchronous with the trigger pulse, is supplied to the DAQ to ensure that the fluorescence signal from the PMT is only recorded when the probe VCO is active.

employing a double-pass AOM set-up, controlled by a pair of VCOs. The entire fluorescence spectrum of a single trapped calcium ion can be measured rapidly and with high precision while maintaining a low ion temperature and good ion localisation throughout the scan.

5.2 Experimental set-up

Figure 5.2 shows a schematic of the experimental set-up. A 397 nm laser in double-pass AOM configuration (see Sec. 4.2) is fibre coupled to the ion trap and aligned either along the axis or in the radial plane of the trap. The laser cools a single trapped calcium ion in the centre of the trap. The ion fluorescence is collected with an objective lens and photons are counted with a PMT. The PMT signal is recorded with a DAQ and the timing of the measurement is controlled by a pulse generator[1].

A pair of VCOs are connected through an rf-switch[2] to the AOM. The rf-signal amplitude and frequency of each VCO output is controlled by analogue signals from the DAQ.

[1] SRS-DG5920 four-channel pulse generator
[2] Mini-Circuits ZASWA-2-50DR DC-5GHz

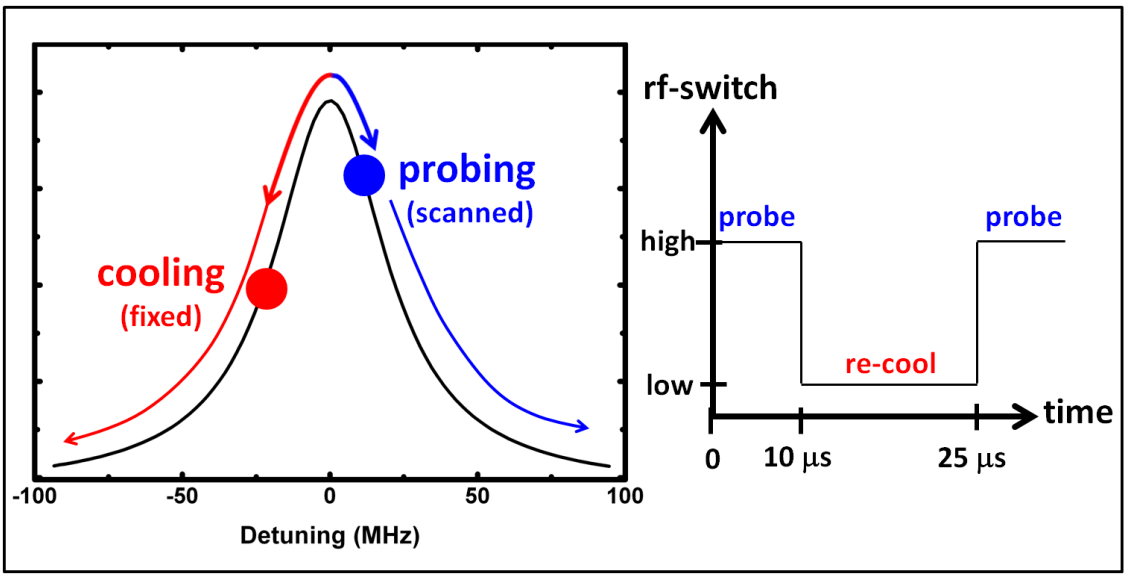

Figure 5.3: *Left*: The cooling VCO maintains a frequency shift selected for optimal Doppler cooling and remains fixed for the duration of the scan. The probe VCO is stepped over a frequency range covering the entire fluorescence spectrum. *Right*: A typical pulse sequence used during a spectroscopy measurement. The sequence is repeated at a rate of 40 kHz giving a pulse duration of 25 μs. The AOM is controlled solely by the probe VCO when the trigger pulse supplied to the rf-switch is high. When the pulse supplied to the rf-switch is low, control of the AOM is switched back to the cooling VCO and the ion is re-cooled.

The cooling VCO maintains a constant frequency that is selected for optimal laser cooling. The frequency output of the probe VCO is stepped over the probe frequency range, which typically spans 200 MHz. A square pulse from the pulse generator is applied to the rf-switch in order to switch control of the AOM from the cooling VCO to the probe VCO for the duration of the pulse. An identical pulse is simultaneously applied to the DAQ and acts as a gate for the PMT signal. Therefore, photon counts from the PMT are only recorded during the probe pulse. Following a probe pulse, control of the AOM is switched back to the cooling VCO and the ion is re-cooled.

Fig. 5.3 shows a schematic of the pulse sequence. Typically, the pulse sequence is repeated at a rate between 10 kHz and 40 kHz. Order 10,000 probe pulses of duration between 5 μs and 25 μs are applied for each probe frequency and the photon counts for all pulses are summed to produce a single data point in the fluorescence spectrum. After collecting a data point, the probe frequency is stepped and the process is repeated until the entire fluorescence profile has been measured. Finally, a lineshape is fit to the collected fluorescence spectrum and the line centre and line width are recorded.

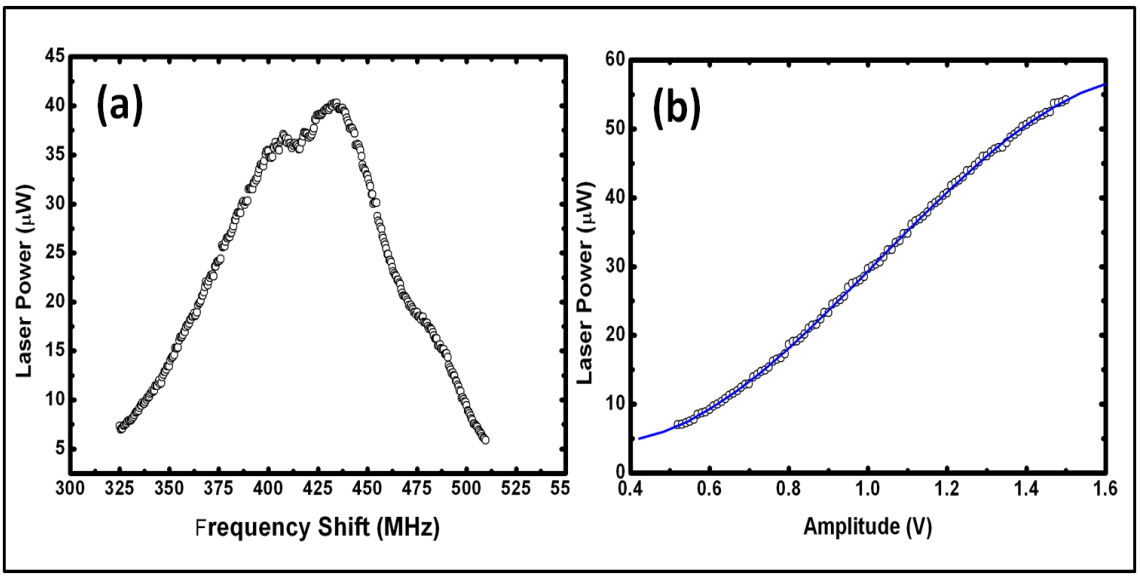

Figure 5.4: (a) The laser power in the double-pass first-order diffracted beam as a function of the frequency of the rf-signal input to the AOM. The amplitude of the input rf-signal is kept constant throughout the scan. (b) The laser power in the double-pass first-order diffracted beam as a function of amplitude of the rf-signal input to the AOM. The frequency of the input rf-signal is kept constant throughout the scan. A cubic function is fit to the data (solid line).

5.2.1 Scan calibration

The 397 nm laser power must be kept the same for each probe frequency step in the scan. However, the laser power in the beam diffracted by the AOM varies as a function of the acquired frequency shift. The measured relationship between the laser power in the diffracted beam and the frequency of the rf-signal from the probe VCO is shown in Fig. 5.4(a). The laser power in the diffracted beam also depends on the amplitude of the rf-signal input to the AOM. The measured cubic relationship between the laser power and the amplitude of the rf-signal is shown in Fig. 5.4(b). In order to produce a constant 397 nm laser power during the frequency scan, the amplitude of the rf-signal input to the AOM is scanned concurrently with the frequency.

During calibration, the frequency is stepped while simultaneously measuring the 397 nm laser power. For small frequency steps (less than 0.5 MHz) the change in laser power resulting from the change in frequency is small. The rf-amplitude necessary to compensate the change in laser power is calculated from a linear fit interpolation to a small region of the plot in Fig. 5.4(b). An rf-amplitude value giving constant laser power is determined for each step in the frequency scanning range. The resulting set of rf-amplitudes as a function of frequency is shown in Fig. 5.5(a). Fig. 5.5(b) shows the laser power during

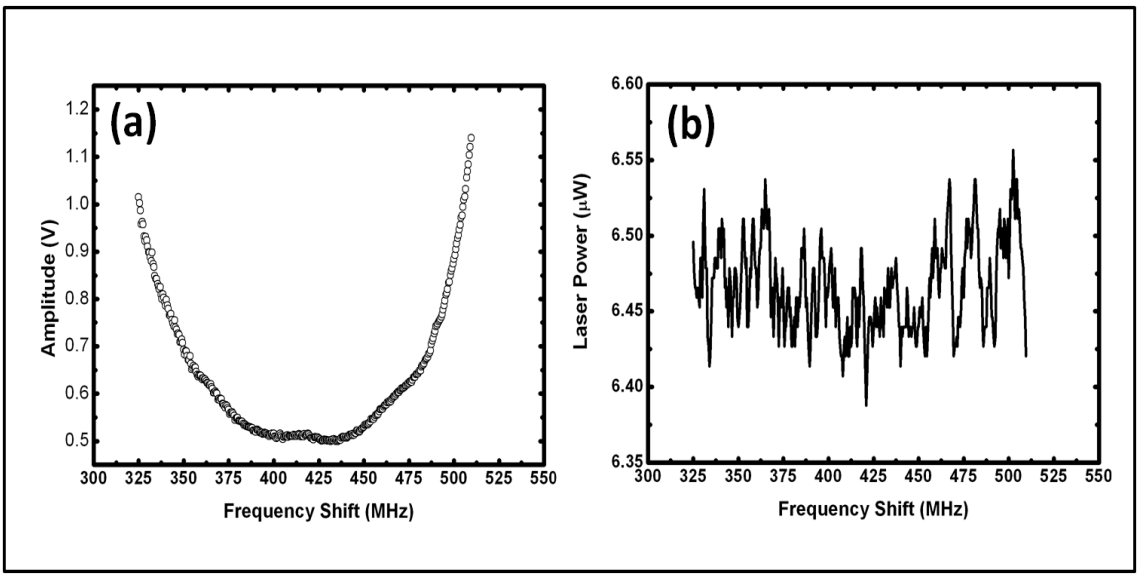

Figure 5.5: (a) The set of rf-signal amplitudes which provide a constant laser power for each step in the frequency scan. (b) The 397 nm laser power measured during the frequency scan when the compensating rf-amplitude values shown in (a) are applied. The laser power is constant throughout the scan with fluctuations less than 2% of the mean.

the frequency scan when the set of rf-amplitude values shown in Fig. 5.5(a) are applied. The laser power remains constant with fluctuations smaller than 2% of the mean.

5.2.2 Computer control

A LabView VI has been developed to control the spectroscopy measurement. The user controlled input parameters include the repetition rate of the pulse sequence, the duration of each probe pulse, the frequency resolution of the scan, the duration of each frequency step and the 397 nm laser power during probing and re-cooling. The typical run-time of the scanning program is between 10 seconds and 30 seconds depending on the desired resolution and the ion fluorescence collection SNR. Following a scan, a Lorentzian function is fit to the data and the centre, width and coefficient of determination (R^2) of the fit are output. R^2 describes how well the data fits the fitting function and is defined by

$$R^2 = 1 - \frac{\sum_i (y_i - f_i)^2}{\sum_i (y_i - \bar{y})^2}, \tag{5.1}$$

where y_i are the data points, f_i are the fit values and $\bar{y}$ is the mean value of the data points. As the fit residuals approach zero, R^2 approaches 1.

Fig. 5.6 shows a 2 MHz resolution fluorescence spectrum collected during a computer controlled spectroscopy measurement. A single calcium ion is probed over a 200 MHz

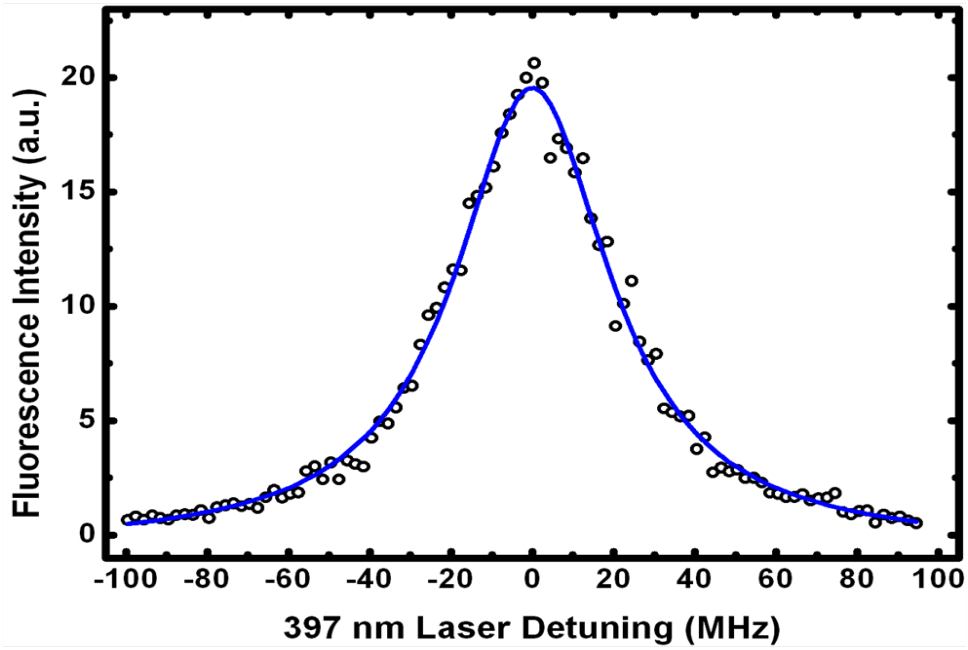

Figure 5.6: Fluorescence spectrum collected during a computer controlled spectroscopy measurement with 2 MHz resolution. A Lorentzian function has been fit to the data (solid line). The width of the spectrum is 46(1) MHz, the run-time of the measurement is 23 seconds and the value of R^2 for the fit is 0.991.

range by a scan with a total run-time of 23 seconds. For each step in the scan, 10 μs of probing is followed by 15 μs of re-cooling. The pulse sequence is repeated at a rate of 40 kHz. A Lorentzian function has been fit to the data and the measured width of the spectrum is 46(1) MHz. This is approximately equal to 2Γ, where Γ is the natural linewidth of the $4S_{1/2} \rightarrow 4P_{1/2}$ transition, and is consistent with the expected homogeneous broadening for the 397 nm laser power used. The value of R^2 for the fit is 0.991.

5.3 Measurement characterisation

5.3.1 Pulse sequence

The most important parameters to consider when optimising the spectroscopy measurement are the duration and repetition rate of the probing. For each step in the frequency scan a sufficient fluorescence signal must be collected while constantly maintaining a cool and well localised ion. For probe frequencies close to line centre or on the blue side of the line centre, the ion's temperature will increase due to momentum kicks from photon scattering events and the lack of laser cooling. In order to maintain a low ion temperature, an upper limit on the duration of each probe pulse must be set. Each probe pulse is followed

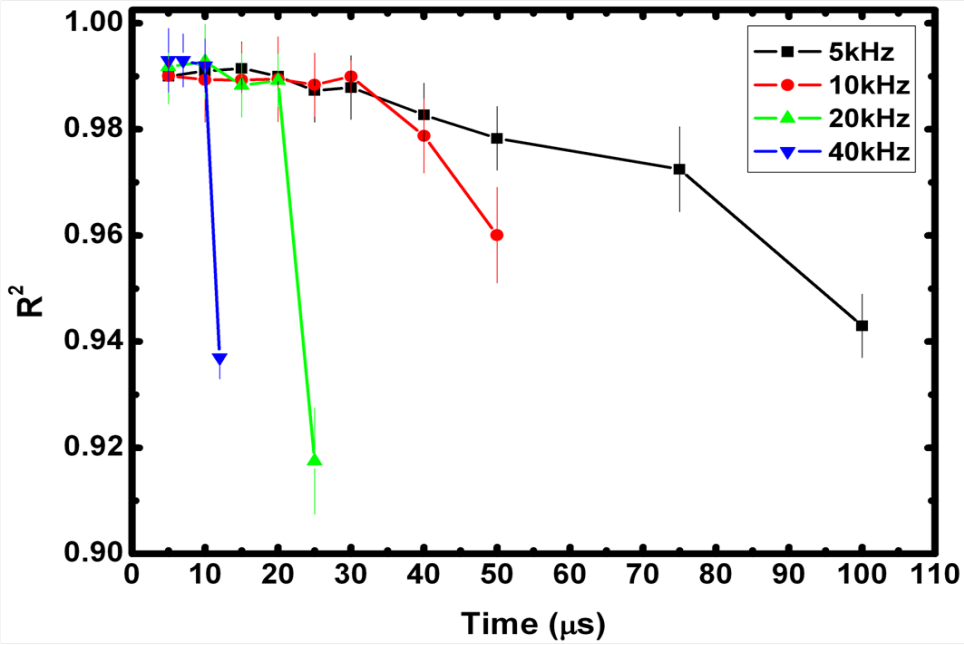

Figure 5.7: R^2 as a function of probe time for a range of pulse sequence repetition rates. For pulse sequence repetition rates of 20 kHz and 40 kHz the value of R^2 drops sharply when the ratio of re-cooling duration to probe duration is less than 1.2(1). For pulse sequence repetition rates of 5 kHz and 10 kHz R^2 begins to decrease when the probe time exceeds 35(5) μs.

by a re-cooling pulse that removes the measurement induced motion of the ion. The re-cooling pulse must be long enough to fully restore the ion's equilibrium state. Otherwise, an accumulation of thermal energy throughout the course of the scan will result. To avoid a 'pile-up' of thermal energy during the scan, a lower limit on the ratio of the re-cooling time to probing time must be established.

For a pulse sequence with sufficient re-cooling time, the spectral lineshape is Lorentzian with a width determined by contributions from the natural linewidth of the transition and homogeneous broadening. Inhomogeneous contributions to the lineshape, caused by the thermal motion of the ion, are not detectable in the fluorescence spectrum if the ion temperature remains low. Thermal motion of the ion, due to laser heating through excessive probing, will only occur for probe frequencies close to line center or on the blue side of the resonance peak. Therefore, for the case of excess thermal motion, inhomogeneous broadening will only contribute to the lineshape in the regions near line centre or on the blue side of the resonance peak. The result is a fluorescence spectrum with a non-Lorentzian shape.

We employ the coefficient of determination (R^2) of the Lorentzian fit to detect the presence of distortion in the spectral lineshape due to heating effects. We collect fluorescence

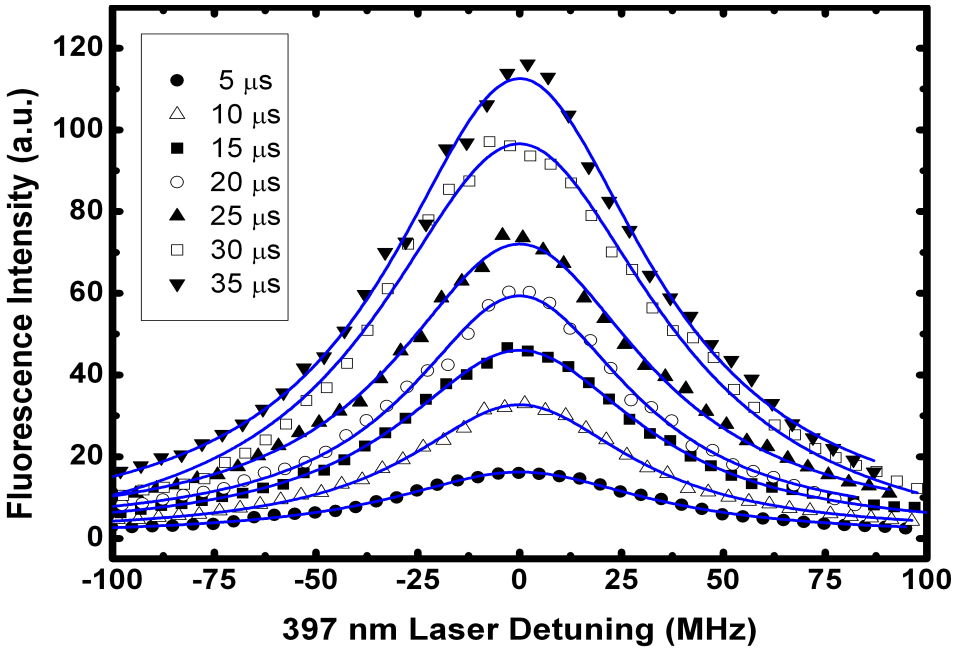

Figure 5.8: Fluorescence spectra collected for probe times in the range between 5 μs and 35 μs for a re-cooling time to probe time ratio greater than 1.2(1). The pulse sequence repetition rate is 1 kHz for each measurement. A Lorentzian function is fit to each spectrum (solid lines) and R^2 >0.99(1) in each case.

spectra for a range of pulse sequence parameters. The results are used to determine both an upper limit on the probe time and a lower limit on the ratio of re-cooling time to probe time.

Fig. 5.7 shows the R^2 value of the Lorentzian lineshape fit to the measured fluorescence spectrum as a function of the probe time for a range of pulse sequence repetition rates. Each data point is the mean R^2 value for ten fluorescence spectra of a single ion. The error bars are the standard deviation of each data set. A single 397 nm laser aligned in the radial plane of the trap with a constant laser power of 6(2) μW is used for each measurement. A fixed laser detuning of -15 MHz is used during the re-cooling portion of each pulse sequence. A frequency range covering 200 MHz in steps of 2 MHz is probed for each spectrum.

For pulse sequence repetition rates of 20 kHz and 40 kHz the value of R^2 is consistently greater than 0.99(1) until it drops sharply for probe times of 25 μs and 12.5 μs respectively. This drop is caused by a distortion of the fluorescence spectrum due to the heating pile-up effect discussed above. For a probe time of 25 μs at a repetition rate of 25 kHz, and for a probe time of 12.5 μs at a repetition rate of 40 kHz, the pulse sequence has equivalent probe and re-cooling durations. When the probe frequency is tuned to the point on the spectrum corresponding to maximum heating, the ion's equilibrium state can only be fully

restored with a re-cooling detuning selected for maximum cooling, as is the case for these measurements. In addition, the duration of re-cooling must be at least equal in duration to that of the probing. However, we empirically find that the duration of re-cooling must be greater than the duration of probing. This is likely due to small magnitude laser frequency fluctuations leading to a heating of the ion following a single pulse sequence. A small increase in the ion's temperature following a single pulse sequence can rapidly accumulate to a large net increase in temperature following many pulses. The effect is exacerbated when higher pulse repetition rates are used. For the data set collected with a pulse repetition rate of 40 kHz, the minimum ratio of re-cooling duration to probe duration for which Lorentzian fluorescence spectra with $R^2 > 0.99(1)$ can be measured is 1.2(1). This lower limit can also be applied to the other data sets, where a lower repetition rate is used.

For repetition rates of 5 kHz and 10 kHz, R^2 begins to decrease for increased probing time despite the fact that the re-cooling time to probe time ratio remains greater than 1.2(1). Even though the ion may be fully restored to the equilibrium state following probing, for long probe durations heating of the ion leads to a significant Gaussian contribution to the total lineshape. As a result, the fluorescence rate during probing will change as a function of time due to the increased width and decreased amplitude of the fluorescence spectrum. Since this effect only occurs for probe frequencies near line centre or on the blue side of line centre the resulting measured flourescence spectrum will have a distorted shape. The data in Fig. 5.7 shows that this effect becomes measurable as a drop in R^2 for probe durations between 30 μs and 40 μs. This sets an upper limit of 35(5) μs on the duration of probing. Fig. 5.8 shows fluorescence spectra collected with probe times between 5 μs and 35 μs for a re-cooling time to probe time ratio greater than 1.2(1). Each spectrum has a Lorentzian fit with $R^2 > 0.99(1)$. For probe durations beyond 35(5) μs the measured spectrum will be distorted regardless of the re-cooling duration due to the temperature increase of the ion during probing.

We have measured a quadratic relationship between the temperature increase of the ion and the time for a fixed laser detuning on the blue side of the line centre. The laser detuning is empirically selected for the maximum heating of the ion (see Sec. 8.4.2). 35(5) μs of heating corresponds to a measurement induced temperature increase of 10(2) mK.

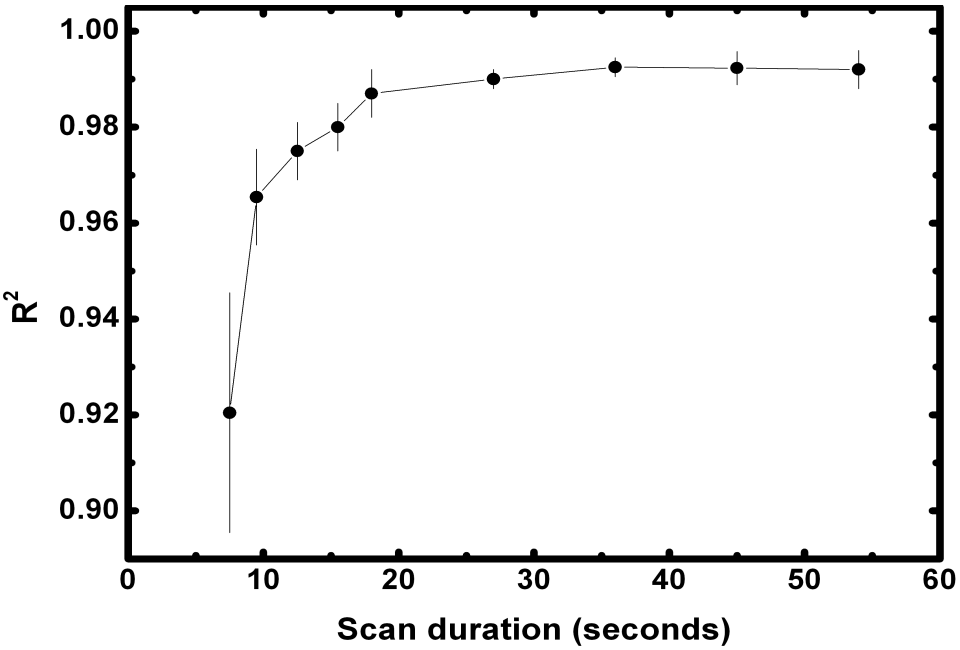

Figure 5.9: The R^2 of the Lorentzian fit to the measured fluorescence spectrum as a function of the scan duration for fixed pulse sequence and laser parameters. Each data point is the mean R^2 for ten spectra. The error bars are the standard deviation of each data set. For a scan duration greater than or equal to 23(5) seconds, the value of R^2 is greater than or equal to 0.988(2)

5.3.2 Interrogation time

The duration of the spectroscopy measurement can be minimised by optimising the time spent on each step in the scan, by increasing the ion fluorescence SNR or by increasing the ion fluorescence collection efficiency. The fluorescence collection efficiency depends on the numerical aperture of the objective lens and is 0.1% in the current experimental set-up. The ion fluorescence SNR depends on the 397 nm laser scatter and the optimisation of the imaging system. For the experiments performed here, the ion's on-resonance fluorescence SNR is 15:1. In the case of fixed ion fluorescence SNR and ion fluorescence collection efficiency, the R^2 value of the Lorentzian fit increases as the total duration of each step in the frequency scan is increased. We have measured R^2 as a function of the total scan time by varying the number of probe pulses used for each step in the scan.

Fig. 5.9 shows the R^2 value of the Lorentzian lineshape fit to the measured fluorescence spectrum as a function of the duration of the measurement. Each data point is the mean R^2 value for ten fluorescence spectra of a single ion. The error bars are the standard deviation of each data set. A single 397 nm laser aligned in the radial plane of the trap with a constant laser power of 6(2) μW is used for each measurement. A fixed laser detuning of -15 MHz is used during the re-cooling portion of each pulse sequence. A

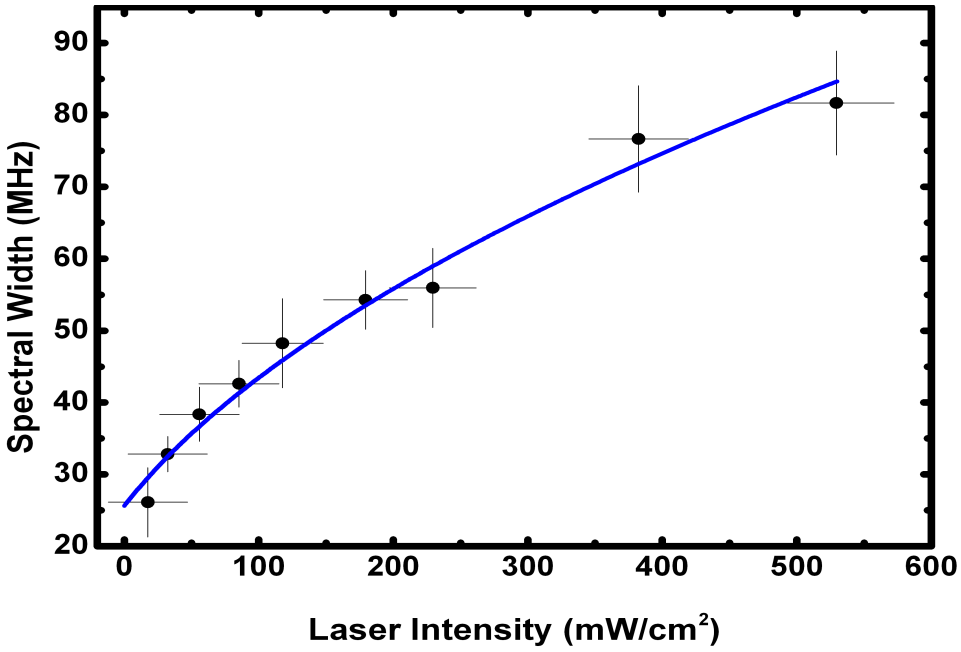

Figure 5.10: The width of the collected fluorescence spectrum as a function of the 397 nm laser intensity. Equ. 2.34 is fit to the data (solid line). The fit gives a value of 53(11) mW/cm^2 for the saturation intensity and a value of 26(2) MHz for the natural linewidth.

frequency range covering 200 MHz in steps of 2 MHz is probed for each spectrum. The pulse repetition rate is 40 kHz with a probe time of 10 μs and a re-cooling time of 15 μs. The duration of the scan is controlled by varying the number of probe pulses over a range from 1,500 to 15,000 pulses per step in the scan. For scan durations longer than 30 seconds, the value of R^2 is observed to level-off to approximately 0.990(5). For a scan duration greater than or equal to 23(5) seconds, the value of R^2 is greater than or equal to 0.988(2). This is taken to be the lower limit of scan duration for fluorescence spectra collected with the current experimental set-up.

5.4 Saturation intensity of the $4S_{1/2} \rightarrow 4P_{1/2}$ transition

We have measured the saturation intensity of the calcium ion $4S_{1/2} \rightarrow 4P_{1/2}$ transition using the above described spectroscopy technique. A calcium ion is trapped and laser cooled with a single 397 nm laser beam aligned with a component in all three spatial dimensions. The beam is focused with a 100 mm plano-convex lens to a spot with diameter 66(2) μm at the location of the ion. The ion is re-pumped by the pair of lasers at 850 nm and 854 nm as described in Sec. 2.2.3.

The fluorescence spectrum of the ion is measured for a range of cooling laser intensities using the optimal spectroscopy pulse sequence parameters discussed above. The laser

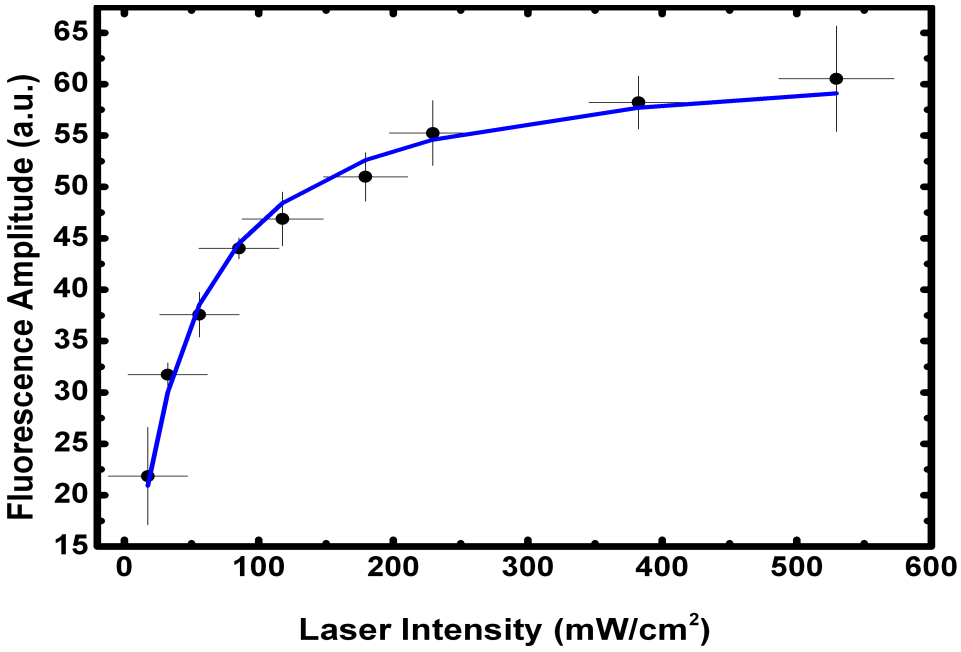

Figure 5.11: The amplitude of the collected fluorescence spectrum as a function of the 397 nm laser power. Equ. 2.52 is fit to the data (solid line). The fit gives a value of 35(4) mW/cm^2 for the saturation intensity.

power at the position of the ion is determined by measuring the power both before the laser enters the vacuum chamber and after it exits the chamber with a photodiode. The difference between these two measurements gives the power loss due to reflection and absorption of the beam during transmission through the two chamber windows. Assuming that the losses are equal for each chamber window, the power can be monitored during the spectroscopy experiment by measuring the power of the beam exiting the chamber.

For each measurement, the spectroscopy probe duration is 10 μs and the re-cooling duration is 15 μs for a pulse sequence repetition rate of 40 kHz. The probe and re-cooling laser intensities are equivalent for each scan. A frequency range covering 200 MHz in steps of 2 MHz is probed for each spectrum. A fixed laser detuning of -15 MHz is used during the re-cooling portion of each pulse sequence. Ten consecutive spectra are collected for each laser intensity and the mean and standard deviation of the fluorescence spectrum amplitude and width are recorded. For each Lorentzian fit $R^2 > 0.99(1)$.

Fig. 5.10 shows the width of the measured fluorescence spectrum as a function of the 397 nm laser intensity. Equ. 2.34 is fit to the data (solid line). The fit gives a saturation intensity of 53(11) mW/cm^2, which agrees with the value of 45.88 mW/cm^2 calculated from Equ. 2.32. In addition, the fit gives a natural linewidth of 24(5) MHz, which agrees with the literature value of 22.4 MHz [62].

The amplitude of the fluorescence spectrum as a function of the 397 nm laser intensity is shown in Fig. 5.11. Equ. 2.52 is fit to the data (solid line). The fit gives a saturation intensity of 35(4) mW/cm^2. The lower saturation intensity for this fit is due to the larger effective decay rate as discussed in Sec. 2.2.3.

These results confirm that the Doppler cooling scheme we employ with the 850 nm and 854 nm repump lasers can be well approximated by a two-level system with independent linewidth and saturation intensity. The linewidth is determined only by the spontaneous decay of the $4P_{1/2}$-state. However, the continuous fluorescence rate is also dependent on the re-pumping.

Chapter 6

Weighing of trapped ion crystals

6.1 Introduction

The precise measurement of the secular motion of ions in an ion trap is an important tool in modern atomic physics. In many applications, most notably trapped ion quantum information processing (QIP) [88, 89, 90] and metrology [91, 92, 93, 94], the motion of the ions must be cooled close to the motional ground state, which requires the precise knowledge of the motional spectrum of the trapped ions. Furthermore, knowledge of the motional spectrum is crucial for ion-trap quantum information experiments to enable high fidelity quantum gates [48, 95]. Recently, the measurement of the individual secular frequencies of ions in large multi-component ion crystals has been exploited to investigate the photo-dissociation of large molecules [96] and to perform high resolution spectroscopy of molecular ions [18, 7, 8]. These novel applications make it especially interesting to investigate innovative ways of performing secular frequency measurements quickly and with high precision.

Often the secular frequency of ions is measured by continuous excitation of the ions' motion and the simultaneous observation of their fluorescence level [97] or the phase between the ions' oscillation and the excitation [45]. In multi-component ion crystals, the excitation of the secular motion of one ion species may heat the entire crystal which results in a decrease in fluorescence [27, 98]. Side-band spectroscopy, which is used routinely in QIP and high resolution spectroscopy with trapped ions, can also be employed to measure the secular frequency of ions [99, 100].

Instead of utilising the change in the fluorescence level, the induced modulation of the fluorescence can be used to extract a spectroscopic signal. The ion's oscillation leads to

a modulation of its fluorescence which can be measured by correlating the fluorescence with the external modulation [41, 42, 43, 44]. Alternatively, the second-order correlation function ($g^{(2)}$-function) of the fluorescence can be measured [101, 102].

In this chapter we present a novel method to measure the COM-mode frequency which is suitable for a wide range of ion crystals reaching from single ions to several hundred ions. We employ the Fourier transform of the auto-correlation of the ions' fluorescence intensity while exciting their motion by a pulsed electric field. The resolution of this method is governed by the motional damping due to laser cooling and the SNR of the fluorescence. We demonstrate a resolution of better than 100 Hz with an interrogation time on the order of seconds. The increase in the ion's average temperature is less than 3 mK and the method is shown to work well even with large ion crystals. The technique we present is unique in the fact that it provides an accurate and fast real-time secular frequency measurement without the need for modifications to the standard laser cooling scheme. In effect, only the fluorescence during Doppler cooling is analysed. Owing to its non-invasive nature, it can be employed in a diverse range of novel applications.

In the first part of this chapter we discuss the principles of this method and the experimental set-up. The characterisation is then presented, where the secular frequency of a single trapped ion is measured and the results are compared to a model of the system. In the last section, we present some of the possible applications of this method. For a short mixed ion string we measure the axial COM-mode frequency of the different ion configurations and extract the mass of a dark ion embedded in a short ion string. Finally, we demonstrate that this method can be utilised to measure the COM-mode frequency of three-dimensional ion crystals with several hundred ions without deteriorating the crystal structure.

6.2 Measurement principle

The measurement principle is based on the detection of the Doppler induced modulation of the ion's fluorescence due to its motion, as described in Sec. 2.2.6. In contrast to the other methods described above, the motion is excited by short voltage pulses and detected through the auto-correlation of the ion's fluorescence. The secular frequency is then determined by Fourier transforming the auto-correlation.

As described above, several schemes have been demonstrated to measure the modulation of the ion's fluorescence due to its motion. We employ the auto-correlation of the

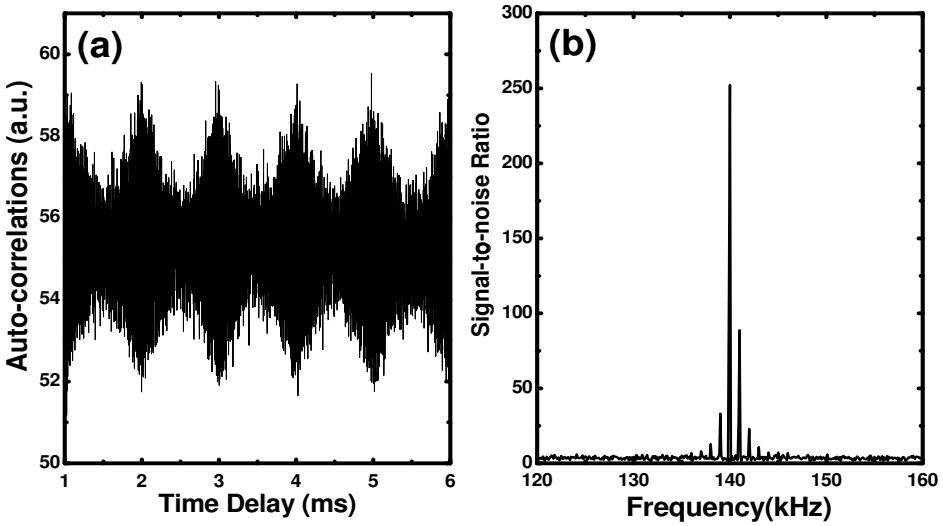

Figure 6.1: (a) Auto-correlation of the arrival times of photons collected from the modulated single ion. The interrogation time is 45 seconds, the driving pulse amplitude is 2.0 V, the repetition rate is 1 kHz and the pulse width is 3 μs. An axial cooling laser power of 10 μW is used. (b) Motional spectrum of the auto-correlation with a high contrast peak at the secular resonance.

fluorescence signal measured by a photomultiplier. Taking the FFT of the auto-correlation gives the motional spectrum of the ion. This technique provides a high signal-to-noise spectrum on a flat background which is independent from the timing of the excitation pulses.

Instead of using a monochromatic excitation, we employ periodic broadband pulses to access a wide range of secular frequencies simultaneously. The motion is driven by these short voltage pulses which are applied to the trap DC-electrodes. For an excitation with period T and a pulse length τ, the pulse train can be expressed as:

$$U(t) = \frac{U_0\tau}{2T} + \frac{2U_0\tau}{\pi T}\sum_{n=1}^{\infty}\mathrm{sinc}\left(\frac{n\pi\tau}{T}\right)\cos\left(\frac{2\pi nt}{T}t\right). \tag{6.1}$$

Thus, it consists of a comb-like spectrum with equidistant spacing of 1/T, which is the repetition rate of the excitation, and a sinc shaped envelope that is determined by the pulse width τ. The width of the individual comb peaks can be neglected in most cases.

During each voltage pulse, the trapping potential is instantaneously shifted which leads to the excitation of the COM-mode of the trapped ions. Due to the laser induced damping of the motion, the oscillation amplitude decays and this results in a damped modulation of the ion's fluorescence. Fig. 6.1(a) shows a typical auto-correlation of the ion's fluorescence

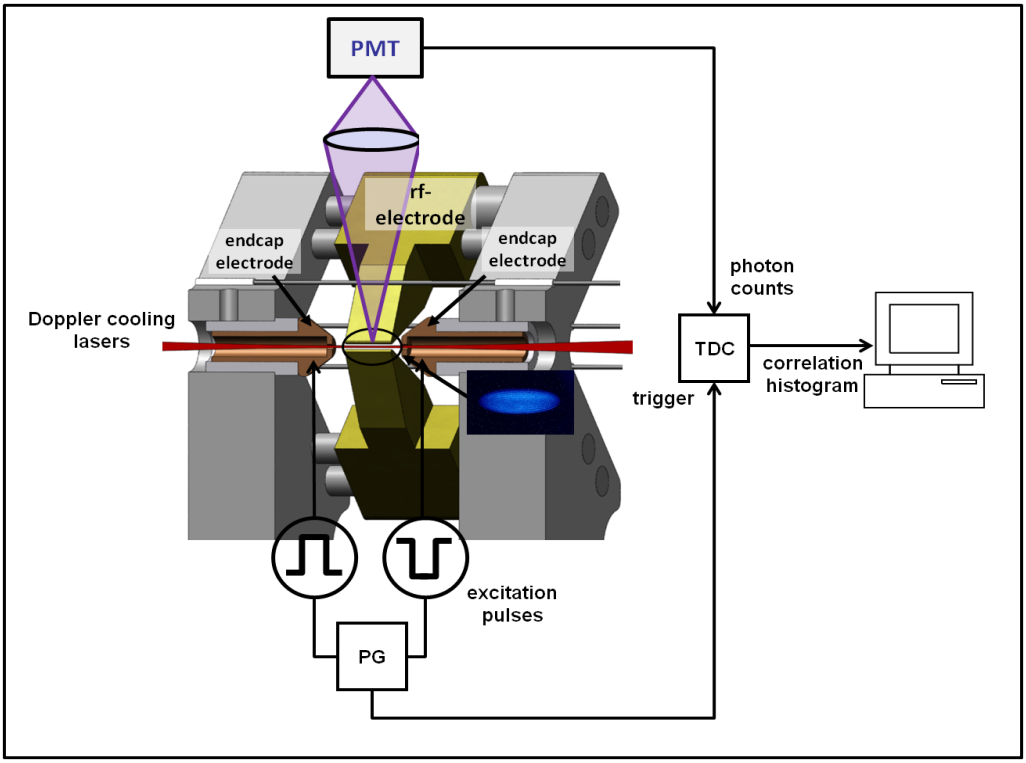

Figure 6.2: The experimental set-up used for weighing ion crystals. The ion trap is shown in cross section and the Doppler cooling lasers are aligned along the trap axis. Pulsed excitation is supplied by a pulse generator (PG). The axial potential is shifted by applying a positive square pulse is to one endcap electrode while simultaneously applying a negative square pulse to the other endcap electrode. The ion's fluorescence is collected with a PMT and photon arrival times are recorded with the TDC. Taking the FFT of the auto-correlation of the photon arrival times gives the motional spectrum of the ion.

for time delays between photon detection events in the range of 1 ms to 6 ms. The periodic excitation is clearly visible, with the occurrence of regular maxima in the oscillation of the auto-correlations together with the exponential decay due to laser induced damping of the ion's oscillation. Fig. 6.1(b) shows the motional spectrum of the auto-correlation measurement with a high contrast peak at the secular resonance. Due to the periodic pulsed excitation described by Equ. 6.1, the motional spectrum consists of a comb of peaks under a Lorentzian envelope corresponding to the motional resonance. The peak separation reflects the repetition rate of the excitation. By extracting only the points from the spectrum which are a multiple of the repetition rate and fitting a Lorentzian, the precise secular frequency can be determined.

6.3 Experimental set-up

Fig. 6.2 shows a schematic of the experimental set-up. The Doppler cooling lasers are aligned along the trap axis collinear with the axial secular motion of the ions. To prepare the secular frequency measurement, the cooling laser detuning is set to maximise the Doppler velocimetry signal and the ion's fluorescence is detected with a PMT. At this point the motional excitation of the ion is activated. The axial trapping potential is shifted by simultaneously applying a positive voltage pulse to one DC-endcap electrode and an equal amplitude negative voltage pulse to the other DC-endcap electrode with a pulse generator (PG). An RC circuit, described in Sec. 4.1.3, is used to superimpose the static DC voltage for the ion's axial confinement with the excitation voltage pulses. The voltage pulses have a typical width of several μs and a magnitude on the order of a few V. The repetition rate of the pulses is typically between 500 Hz and several kHz. During the measurement, the photon detection times are recorded with a TDC[1]. After the chosen measurement time, the auto-correlation of the photon detection times is calculated, from which the spectrum is obtained by Fourier transformation. The secular frequency is identified as the largest peak in the motional spectrum with an error equal to half the repetition rate. The frequency resolution can be improved beyond the repetition rate by fitting a Lorentzian to the motional spectra. With this, a precision of better than 50 Hz has been achieved for a repetition rate of 500 Hz.

We have conducted a numerical analysis which includes the back action of the measurement on the ion's motion. A simulation approximating the ion as a simple harmonic oscillator has been created in Matlab[2]. By solving the ion's equation of motion, non-linear effects of the laser damping as well as effects on the conversion of the ion's motion into a fluorescence modulation are included. The measured data have been analysed and compared with this model to characterise the effects of the excitation of the ion's motion and the laser parameters on the auto-correlation spectrum.

6.4 Measurement characterisation

By thoroughly characterising our measurement scheme the optimal parameters can be found to achieve the maximum frequency measurement resolution. These parameters can be split into two categories: those associated with the interaction of the laser with the ion

[1] FastComtec 7888

[2] The simulation was developed by Dr. Matthias Keller

and those related to the excitation of the ion's motion. The parameters of the periodic voltage pulses applied to the DC-electrodes strongly impact the ion's motion and thus the amplitude of the auto-correlation spectrum. These include the amplitude, repetition rate and width of the pulses in the pulse train. However, these parameters will not affect the conversion of the ion's oscillation into fluorescence modulation. In contrast, the laser parameters impact this conversion by changing the ion's spectral lineshape while at the same time acting on the ion's motion. In effect, the laser induced radiation pressure leads, for the appropriate detuning, to a damping of the motion.

6.4.1 Excitation pulse amplitude

For short excitation pulses, the laser induced damping during the pulse can be neglected, which leads to a linear increase of the ion's elongation in the trapping potential with increasing excitation pulse amplitude. This in turn results in an oscillation amplitude which is proportional to the excitation amplitude. According to Equ. 2.62, the ion's oscillation is converted into a modulation of its fluorescence. The auto-correlation, however, is a bilinear function of the modulation. Thus, the peak height of the motional spectrum, obtained from the FFT of the auto-correlation, increases quadratically with the excitation amplitude. This is clearly visible in the measurements shown in Fig. 6.3 together with a quadratic fit.

For large excitation amplitudes Equ. 2.62 is not valid and the conversion between the ion's oscillation and its fluorescence becomes non-linear. This leads to the occurrence of harmonics of the secular frequency in the auto-correlation spectrum. The measured spectra in Fig. 6.3 (inset) show that for small amplitudes no harmonic of the secular frequency is visible, however, a second peak at twice the frequency occurs for larger amplitudes.

Even though a large excitation amplitude leads to a favorable SNR it has an adverse effect on the ion's temperature that may limit the excitation amplitudes for some applications.

6.4.2 Excitation pulse width

The periodic excitation has a spectrum consisting of a comb-like structure with peaks separated by the repetition rate as described by Equ. 6.1. Its excitation amplitude spectrum is shown in Fig. 6.4 for a range of frequencies and pulse widths. Only frequencies that do not coincide with the zero crossings at $\omega_{sec}\tau = 2\pi$ can be detected. In addition, the excitation amplitude inevitably decreases with increasing frequency.

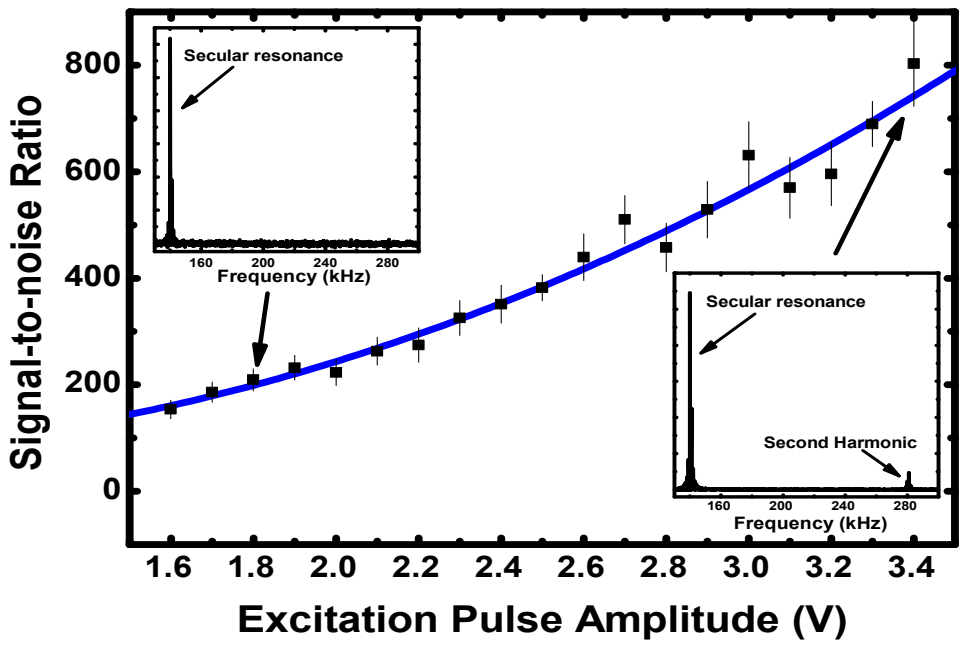

Figure 6.3: SNR of the Lorentzian fit of the auto-correlation spectrum as a function of excitation pulse amplitude for a single ion. The interrogation time for each measurement is 20 s, the repetition rate is 1 kHz, the pulse width is 3 μs, the laser detuning is -30 MHz and the laser power is 10 μW. The insets shows the auto-correlation spectra for excitation pulse amplitudes of 1.8 V and 3.4 V.

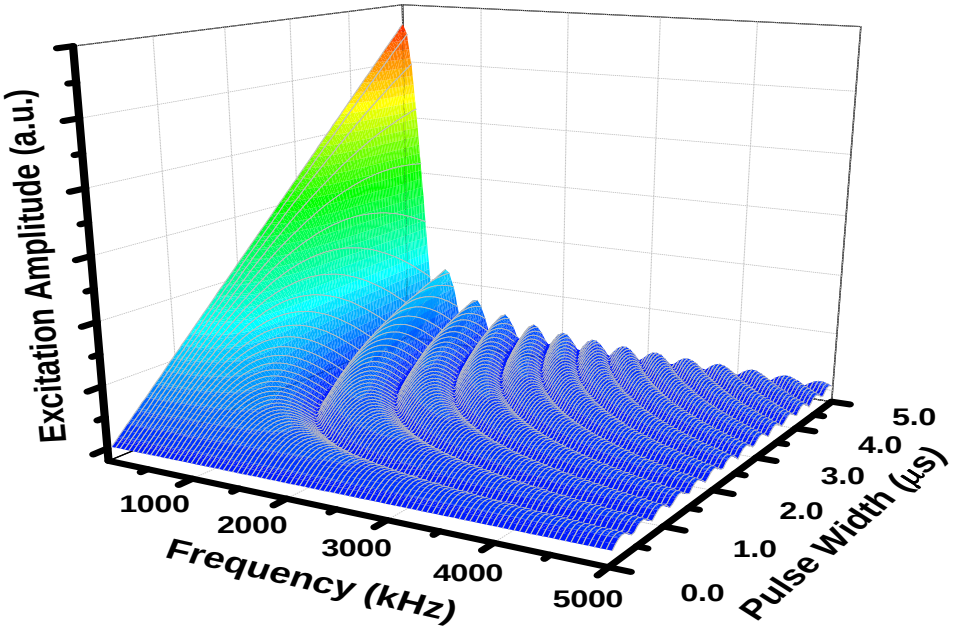

Figure 6.4: Excitation amplitude as a function of secular frequency and excitation pulse width.

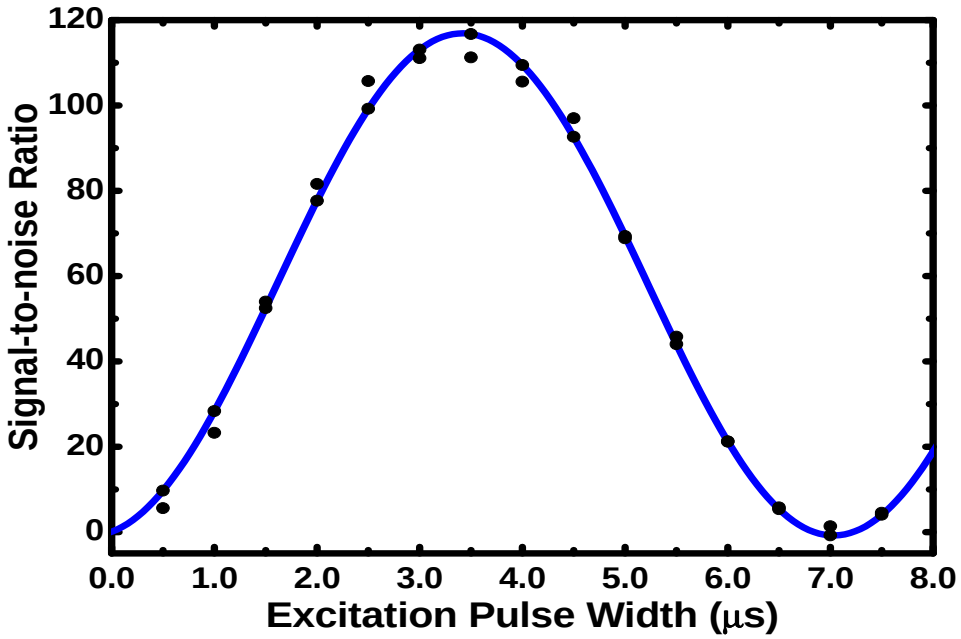

Figure 6.5: SNR of the auto-correlation spectra as a function of excitation pulse width for a single ion. The interrogation time is 10 s, the repetition rate is 1 kHz and the excitation amplitude is 2 V. The COM-mode frequency is approximately 140 kHz. A sine squared function has been fit to the data.

For a fixed secular frequency of the ion, the excitation amplitude exhibits a sinusoidal oscillation as $\sin(\omega_{sec}\tau/2)$. We have measured this behaviour for an axial secular frequency of approximately 140 kHz for modulation pulse widths ranging from 0.5 μs to 7.5 μs. Fig. 6.5 shows the SNR of auto-correlation spectra for the measured range of excitation pulse widths. Due to the quadratic dependency of the signal on the excitation amplitude (see Sec. 6.4.1), the height of the auto-correlation spectrum changes as $\sin^2(\omega_{sec}\tau/2)$. The data agree well with Equ. 6.1 which predicts a maximum at a pulse width of 3.57 μs and a minimum at 7.1 μs for a secular frequency of 140 kHz.

For a given secular frequency, the optimum excitation depends on both the pulse width and the excitation amplitude. Since the secular frequency may not be well known or may change with time, long pulse widths are undesirable as they lead to a narrow excitation spectrum. Employing short pulses increases the spectral width but leads to a decrease of the excitation amplitude. In order to compensate this, the pulse amplitude must be increased and this has an adverse effect on the temperature of ion crystals. Even though the excitation couples mainly to the COM-mode, coupling to higher modes of motion cannot be fully suppressed. Careful balancing of the pulse parameters is required to obtain a wide excitation spectrum while at the same time maintaining a low temperature of the trapped ions during the measurement.

6.4.3 Excitation pulse repetition rate

Increasing the repetition rate of the excitation has two effects on the auto-correlation spectrum. Firstly, the spacing between the comb peaks in the spectrum becomes larger since the separation reflects the repetition rate. Thus, for an accurate determination of the motional frequency of the ion small repetition rates seem advantageous as the spectral resolution increases. The second effect comes from the impact of the repetition rate on the signal amplitude. Each voltage pulse excites the oscillation of the trapped ion which is damped by the interaction with the laser light. Following each pulse the oscillation amplitude of the ion, and therefore the signal, decays. If the decay rate is much faster than the repetition rate of the excitation, the average oscillation over one excitation period is small, which in turn results in a small peak height of the auto-correlation spectrum. Due to the quadratic dependence of the height of the auto-correlation spectrum on the ion's oscillation amplitude, the signal is proportional to the square of the average amplitude, which is described by the first term in Equ. 6.2. In addition, the number of correlation events contributing to the signal increases linearly with the ratio of the interrogation time to pulse period and thus with the repetition rate. Both effects are clearly visible in Fig. 6.6 in which auto-correlation measurements for three different repetition rates are shown.

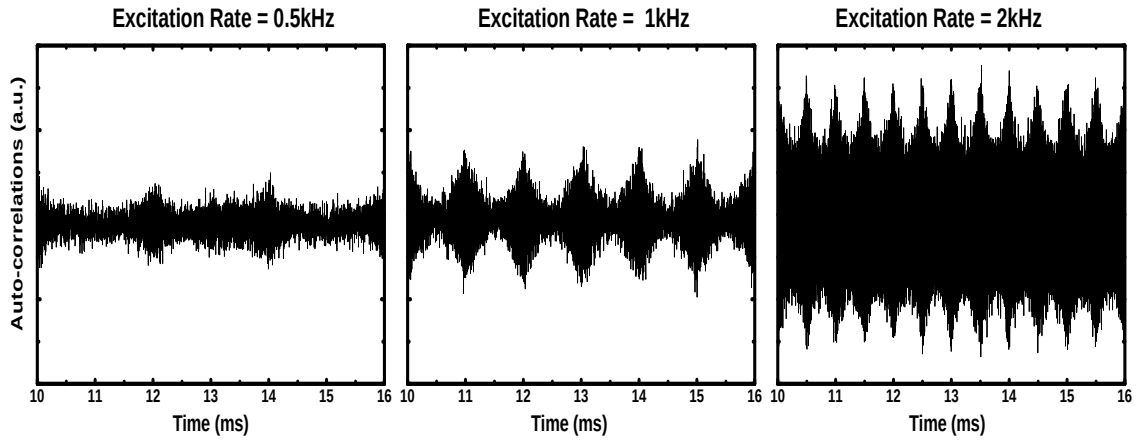

Figure 6.6: Auto-correlation measurements for three repetition rates. In all measurements the laser power is 10 μW, the detuning is -30 MHz, the excitation amplitude is 2 V and the pulse width is 3 μs.

While for a repetition rate of 500 Hz the signal completely decays before another excitation pulse is applied, the oscillation overlaps significantly with the next pulse for a rate of 2 kHz. The increase of the overall amplitude is due to the increase in correlation events for larger repetition rates.

In the regime where the damping is linear, e.g. for small oscillation amplitudes, the

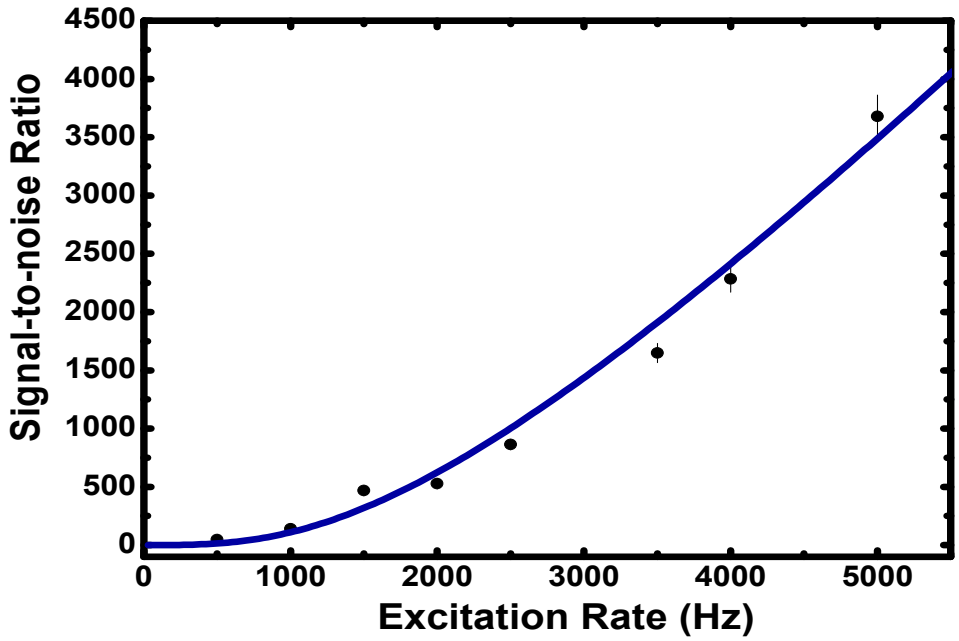

Figure 6.7: SNR of the auto-correlation spectrum for a range of excitation pulse repetition rates measured with a single ion. The laser detuning is -30 MHz, the laser power is 10 μW, the excitation amplitude is 2 V and the pulse width is 3 μs.

dependence of the auto-correlation signal amplitude on the repetition rate R can be approximated as:

$$\text{Signal} \propto \underbrace{\left\{\frac{R}{\gamma}\left(1-\exp\left(-\frac{\gamma}{R}\right)\right)\right\}^2}_{\text{average signal}} \cdot \underbrace{R}_{\text{correlation events}} \tag{6.2}$$

where γ is the damping rate of the ion's motion. Fig. 6.7 displays the measured signal amplitudes of the auto-correlation spectra for a range of repetition rates. Equ. 6.2 is fit to the data. Even though the signal increases with increasing repetition rate, the accuracy of measuring the secular frequency is at the same time adversely affected by the increased spacing of the comb peaks in the excitation spectrum.

The effect of the repetition rate on the measurement accuracy depends on the way the spectrum is analysed. The easiest way of analysing the data is by using the highest comb peak in the auto-correlation spectrum as the secular frequency. In this case the error is half the repetition rate and an increase in repetition rate directly degrades the spectral resolution. This method does enable very fast measurements since a reliable signal can be obtained for a SNR as low as 1. For example, we have achieved a SNR of 12 for a 10-ion crystal with an interrogation time of only 102 ms using a repetition rate of 500 Hz. By fitting a Lorentzian to the comb peaks the precision can be significantly higher than the repetition rate. A requirement for fitting a Lorentzian is that there are at least three visible comb peaks in the spectrum. For repetition rates smaller than the width of the

auto-correlation resonance, many comb peaks are available increasing the accuracy to which the motional resonance can be measured. In contrast, for repetition rates much higher than the motional damping rate, there is mainly one comb peak of the excitation spectrum contributing to the signal with the other peaks being quadratically suppressed with increasing repetition rate.

A detailed analysis shows that the error in the frequency measurement is proportional to $\frac{R}{H^2}$, with the centre peak height of the auto-correlation spectrum H. Taking Equ. 6.2 into account, the frequency error decreases with increasing repetition rate. The effect of the enhanced signal for large repetition rates offsets the reduction of the comb peaks due to their increased detuning from the auto-correlation resonance. However, this is only valid as long as $R \ll \omega_{sec}$.

6.4.4 Laser detuning

The laser power and detuning affect the conversion of the ion's motion into a modulation of its fluorescence by influencing the ion's state population and thus $\left.\frac{d\rho_{ee}}{d\delta}\right|_{\delta}$ (see Equ. 2.62). However, the velocity dependent radiation pressure directly affects the motion of the ion. For red detuned lasers close to resonance this results in a damping of the ion's oscillation in the trap and thus gives rise to a finite line width of the motional spectrum. For small velocities the damping rate of the ion's oscillation is proportional to $\left.\frac{d\rho_{ee}}{d\delta}\right|_{\delta}$. Therefore, the laser induced damping interferes with the detection of the ion's motion.

According to Equ. 2.62, the optimal conversion efficiency between the ion's motion and its fluorescence is obtained by tuning the laser to the largest gradient of the ion's spectral line profile. However, at this detuning, the laser induced damping has a simultaneous maximum which in turn leads to a reduction of the oscillation amplitude and thus to a reduction in the height of the auto-correlation spectrum. By tuning the laser closer to resonance, the decrease of the conversion efficiency is offset by a reduction of the damping leading to a shift of the optimal detuning towards the atomic resonance. The dependence of the signal strength on the detuning is shown in Fig. 6.8(a). The laser induced damping shifts the optimal detuning towards the atomic resonance and leads to a plateau at small detuning. This can be seen by comparing the position of the maximum SNR with the maximum in the width of the auto-correlation spectrum. The width of the spectrum corresponds to the damping of the ion's motion and thus the slope of its spectral line.

The measurements shown in Fig. 6.8 are fitted with the results of the numerical simulation. The SNR data show very good agreement with the model and the spectral

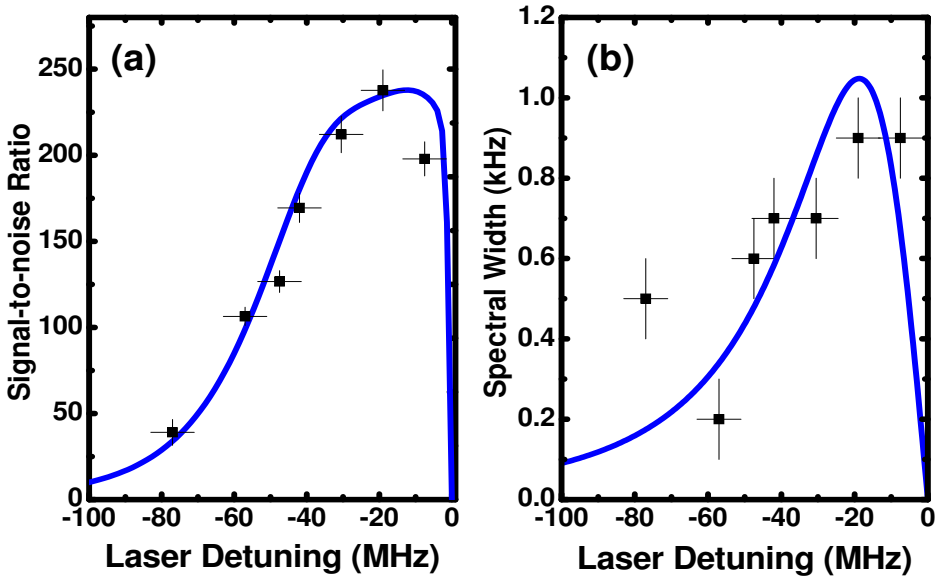

Figure 6.8: SNR and width of the auto-correlation spectrum as a function of the cooling laser detuning measured with a single ion. The laser power is 5 μW, the excitation amplitude is 1.6 V, the pulse width is 3 μs and the repetition rate is 500 Hz.

width measurements show a reasonable agreement. Since the spectra are narrow (FWHM less than 1 kHz), there is increased error in fitting a Lorentzian envelope to the limited number of discrete peaks forming each spectrum.

6.4.5 Laser power

The effect of the laser induced damping of the ion's motion can also be observed in the dependence of the SNR and the width of the auto-correlation spectrum on the laser power which is shown in Fig. 6.9.

For small laser power the signal increases fast and reaches a plateau as illustrated by the data in Fig. 6.9(a). In contrast, the spectral width increases for small laser intensities due to the increased damping and after reaching a maximum it decreases steadily. For small laser intensities, the slope of the ion's spectral line is governed by the fluorescence level while the width of the transition corresponds to the natural line width. Thus, with increasing intensity the signal and fluorescence level increase together. For large laser intensities, however, the fluorescence level saturates while the transition line width is governed by saturation broadening. This results in a decrease of the gradient of the spectrum and thus a decrease in the damping. This reduced damping, in turn, increases the ion's oscillation amplitude. Hence, the height of the auto-correlation spectrum is increased and this compensates the decrease in the conversion efficiency.

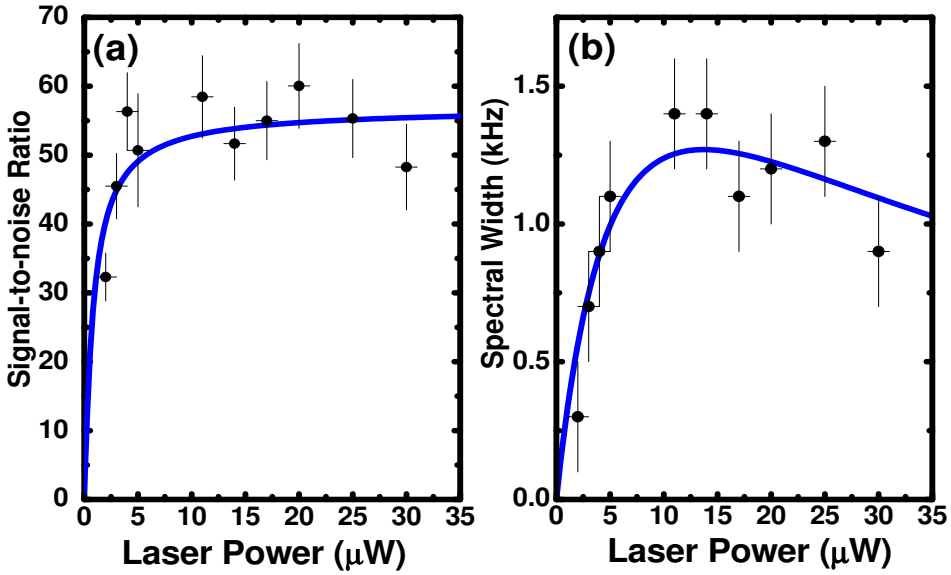

Figure 6.9: SNR and width of the auto-correlation spectrum as a function of the cooling laser power measured with a single ion. The excitation pulse amplitude is 2 V, the repetition rate is 500 Hz, the pulse width is 3 μs and the laser detuning is -40 MHz.

6.4.6 Heating of the ion

For many applications it is critical that the heating of the ion during the measurement is very small. This is especially important if the secular frequency of an entire ion crystal is to be detected. Typically, trapped ions form crystals at temperatures in the order of 100 mK [103]. Thus, the average kinetic energy imparted to the crystal by the measurement must be lower than around 100 mK. For small oscillation amplitudes, the amplitude of the fluorescence modulation can be approximated by Equ. 2.62 which we use to determine the kinetic energy of the ion. By taking the ratio of the auto-correlation's modulation amplitude and its constant offset, the detection efficiency cancels and the oscillation amplitude can be determined by using the spectroscopic properties of the transition which have been independently measured. The maximum energy induced into the COM-mode is calculated from the maximum amplitude of the oscillation whereas the average energy is determined by taking the decay of the oscillation into account.

Fig. 6.10 shows an auto-correlation measurement used to determine the measurement induced kinetic energy of a single ion. To obtain the oscillation amplitude, a damped oscillation has been fitted to the data.

From the analysis of this measurement we have obtained a maximum kinetic energy of 487(22) neV introduced into the ion's motion. This corresponds to a temperature increase

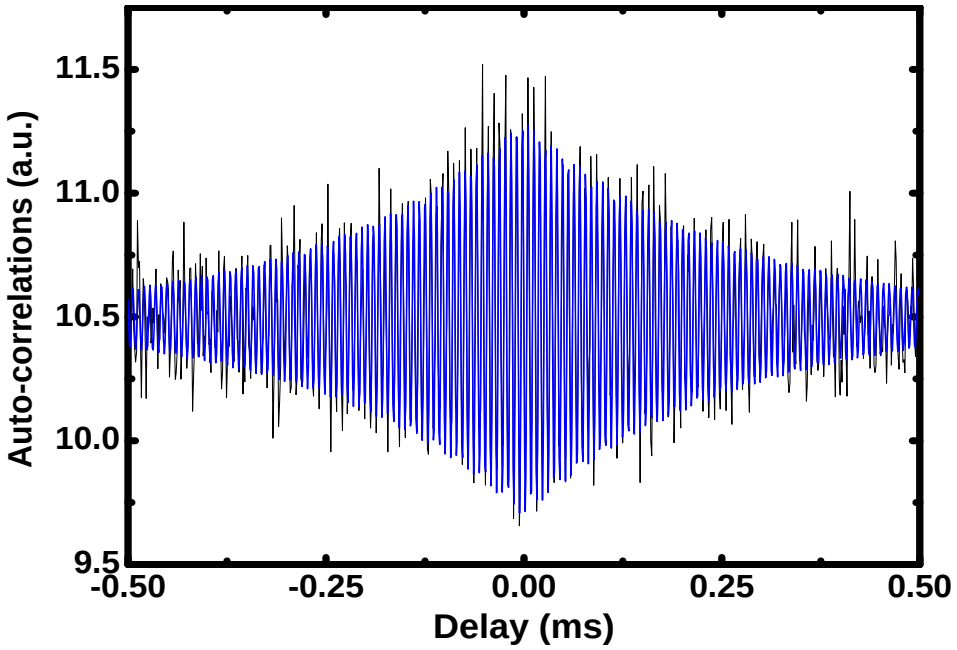

Figure 6.10: Auto-correlation measurement including a fitted damped oscillation. The laser detuning is -30 MHz, the laser power is 5 μW, the excitation amplitude is 2 V, the repetition rate is 500 Hz and the pulse width is 3 μs.

of 11.3(5) mK. The average measurement induced kinetic energy of the ion is around 150 neV corresponding to a temperature increase of about 3 mK. This is low enough for most applications and enables the use of this technique with larger ion crystals. However, the heating depends on the excitation parameters which must be carefully chosen in order to obtain a good signal but at the same time keep the ion's temperature low.

6.4.7 Summary

We have characterised all of the system parameters and shown how each contributes to the SNR of the auto-correlation spectrum. The optimal laser parameters are clearly illustrated by the measurements shown in Fig. 6.8 and Fig. 6.9. The optimal excitation pulse parameters, however, will depend upon the details of the desired application, e.g. the frequency range being measured and the limit placed on the energy imparted to the system by the interrogation. We have shown that the careful balancing of these parameters provides a high contrast motional spectrum (SNR>100) of a single ion with a low average temperature increase (around 3 mK) in a short interrogation time (less than 30 s).

6.5 Application to linear ion strings and three dimensional crystals

In the following section we show how the secular frequency measurement technique can be used to identify the mass of sympathetically cooled dark ions and measure the configuration shifts of a mixed linear ion string. In addition, we apply the technique to measure the COM-mode frequency of a three-dimensional ion crystal.

6.5.1 Ion mass identification

Due to the dependence of the secular motion on the charge-to-mass ratio of the ion, the measurement of its motional frequency can be used to identify the trapped ion species if the charge of the ion is known. To measure the mass of a single dark ion, we trap it alongside a ^{40}Ca-ion which is used to sympathetically cool the dark ion and to detect its secular frequency. The COM-mode frequency of this two-ion string can be expressed by

$$\nu_{\mathrm{COM}}^2 = \left[(1 + M_0/M_1) - \sqrt{1 - M_0/M_1 + (M_0/M_1)^2}\right] \nu_0^2, \tag{6.3}$$

if the charge of the two ions is the same [45]. Thus, if the secular frequency ν_0 of an ion with known mass M_0 is measured, the mass of the dark ion M_1 can be determined by measuring the ion string's COM-mode frequency.

We measure the COM-mode frequency shift with respect to a single ^{40}Ca-ion for a two-ion string in which a ^{40}Ca-ion is trapped alongside a different calcium isotope. The ion strings are loaded into the trap using isotope-selective photo-ionisation. For each isotope, a series of measurements are performed with a driving pulse amplitude of 3.5 V, repetition rate of 500 Hz, pulse width of 3 μs and interrogation time of 30 s. The measured frequencies and the resulting masses of ^{43}Ca$^+$ and ^{44}Ca$^+$ are listed in table 6.1 together with the literature values.

Isotope	Measured Mass (amu)	Literature Value (amu) [104]
^{43}Ca$^+$	42.96(7)	42.9587662(13)
^{44}Ca$^+$	43.90(8)	43.9554806(14)

Table 6.1: The measured masses of two calcium isotopes and their literature values.

The results demonstrate that the mass can be measured with a precision of better than 2×10^{-3}. This precision is only limited by a slow drift of the secular frequency due to the temperature change of the trap during the loading process and the stability of the DC voltage supply.

6.5.2 Configuration shifts in a linear ion string

Since the axial frequency measurement technique we employ induces only little heating into the ions, it is possible to measure the COM-mode frequencies of individual configurations of a mixed species linear ion string. The perturbation of the linear ion string due to the presence of an ion with different mass leads to a shift of the COM-mode frequency which depends not only on the average charge-to-mass ratio of the ions but also on the position of the ions in the string [105].

A measurement of the configuration shifts in a mixed linear ion string is performed for a five ion string consisting of four ^{40}Ca-ions and one dark ion. The dark ion used has a mass substantially larger than the mass of a ^{40}Ca-ion. In order to distinguish the five possible configurations of the ion string, it is monitored with the EMCCD.

The COM-mode frequency is measured for each of the five configurations several times and the average of the measurements is taken. Each re-configuration of the ion string is thermally induced and is triggered by blocking the Doppler cooling lasers for around one second. Sufficient time is available for the interrogation of the string between each configuration change. The axial COM-mode frequency and the standard deviation for each configuration are listed in table 6.2. There are three configurations giving a unique axial frequency shift which are labeled A, B and C. Configurations D and E are equivalent to configurations A and B, and give the same measured axial frequency shift accordingly. Configuration F is the pure string consisting of five ^{40}Ca-ions, which serves as a reference measurement. Fig. 6.11 shows one motional spectrum for each configuration together with a Lorentzian fit.

	Configuration	Axial Frequency (kHz)
A	●○○○○	247.08(17)
B	○●○○○	247.47(18)
C	○○●○○	247.81(16)
D	○○○●○	247.50(17)
E	○○○○●	247.11(19)
F	○○○○○	258.46(3)

Table 6.2: The experimentally measured axial frequencies for each of the five possible configurations of an ion string consisting of four ^{40}Ca-ions and one dark ion (A-E) and a pure crystal containing five ^{40}Ca-ions (F).

The theoretical shift of the axial frequency from the experimentally measured frequency of the pure ^{40}Ca-ion string is calculated for each of the configurations as a function of the mass of the dark ion. The result is shown in Fig. 6.12 together with the measured

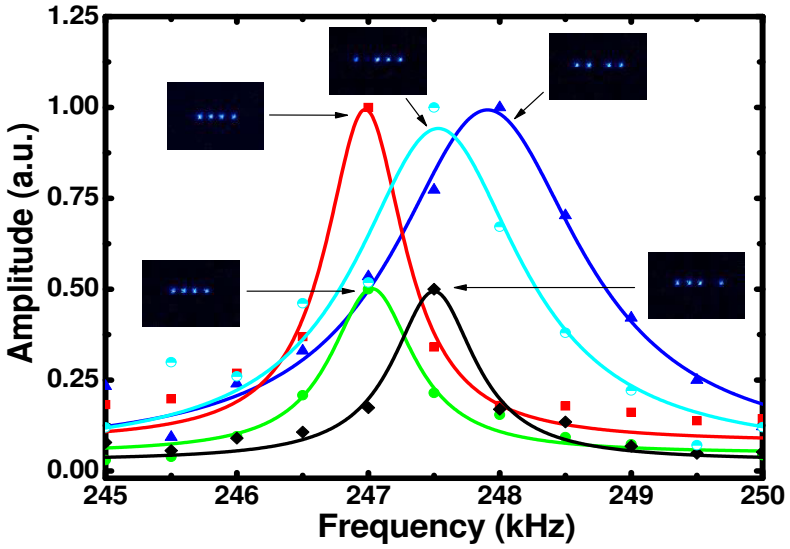

Figure 6.11: Normalised motional spectra measured for each of the five possible configurations of the mixed ion string. Two spectra, given by the symmetric configurations, have been rescaled for clarity. A Lorentzian function is fit to each spectrum. The measurement interrogation time is 15 s, with an excitation pulse amplitude of 1.5 V, a repetition rate of 500 Hz and a pulse width of 3 μs.

frequencies (dotted horizontal lines.) The bands around the measured frequencies indicate the measurement errors and the ellipses show the overlap with the calculated values.

Table 6.3 lists the dark ion masses which correspond to the experimentally measured frequency shift for the three unique configurations. Averaging these three masses gives 57.0(3) amu. This is within experimental error of the mass of the calcium monohydroxide molecular ion, which has a molecular weight of 57.085 amu.

Configuration	Dark Ion Mass (amu)
●○○○○	56.8(2)
○●○○○	57.2(3)
○○●○○	56.9(3)

Table 6.3: The dark ion mass values determined from comparing the experimental configuration shift to the shifts given by the calculation, shown in Fig. 6.12.

6.5.3 Measurement of the COM-mode frequency of a large crystal

The secular frequency measurement described above for single ions and short ion strings can also be applied to large three-dimensional Coulomb crystals. Using the same driving

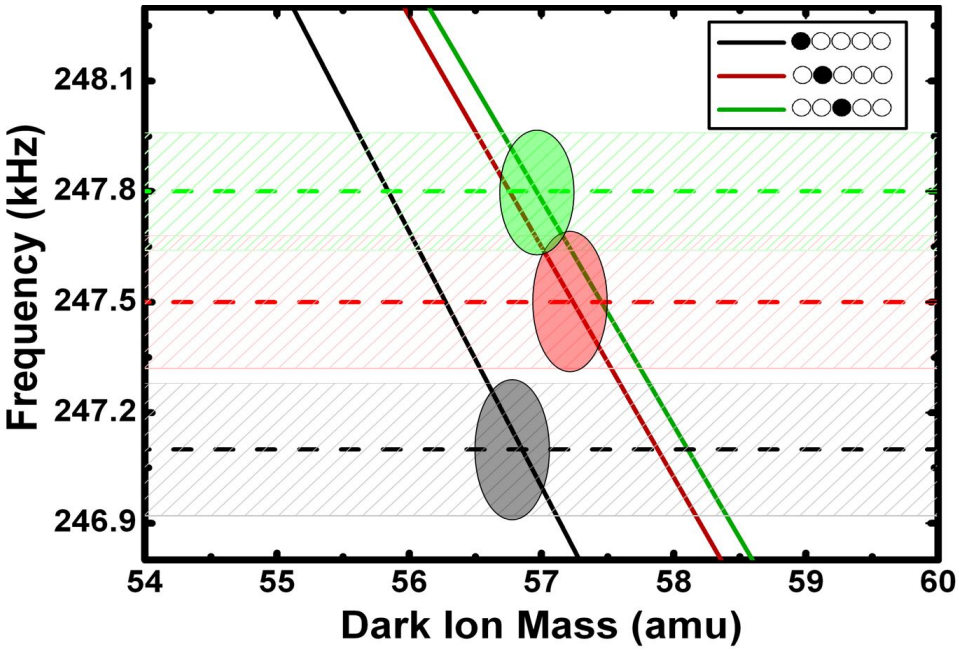

Figure 6.12: Calculation (solid lines) comparing the axial frequency for the three unique configurations in an ion string containing four ^{40}Ca-ions and one dark ion as a function of the mass of the dark ion. Experimentally measured frequencies (dotted horizontal lines) are included with bands indicating the measurement error.

pulse parameters, the structure of the crystal remains completely intact during the measurement. Fig. 6.13 shows a three-dimensional Coulomb crystal with and without excitation. The slight blurring of the image of the crystal with modulation indicates the motion of the ions. However, the crystal structure is still intact. The COM-mode energy has been measured using the procedure described in Sec. 6.4.6 and corresponds to a measurement induced maximum temperature increase of about 61 mK.

The amplitude of the motional spectrum is measured for an interrogation time of 5 s. Fig. 6.14 shows the corresponding auto-correlation of the crystal and its spectrum. Due to the large number of ions in the crystal the SNR of the measurement is still very good despite the short interrogation time and the large laser detuning.

6.6 Summary

We have developed a novel tool to quickly and precisely measure the secular frequency of trapped ions in rf-traps. With our set-up, we have achieved a precision of better than 250 Hz within an interrogation time of 100 ms and a few 10 Hz for an interrogation time of less than 30 s. The interrogation time is limited by the fluorescence collection efficiency, which is about 0.1% in the current set-up. The frequency measurement precision is limited

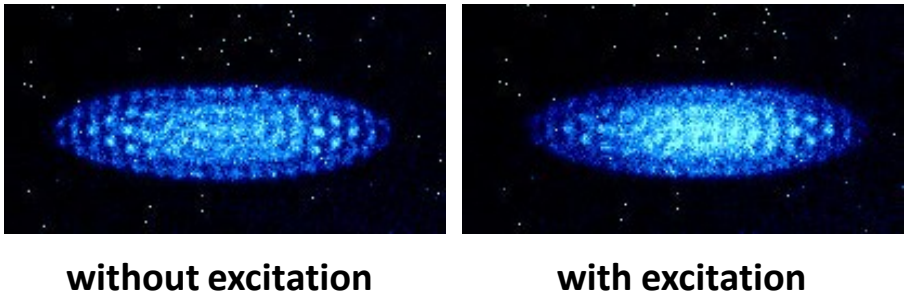

Figure 6.13: A large three dimensional Coulomb crystal made up of a few hundred ^{40}Ca ions.

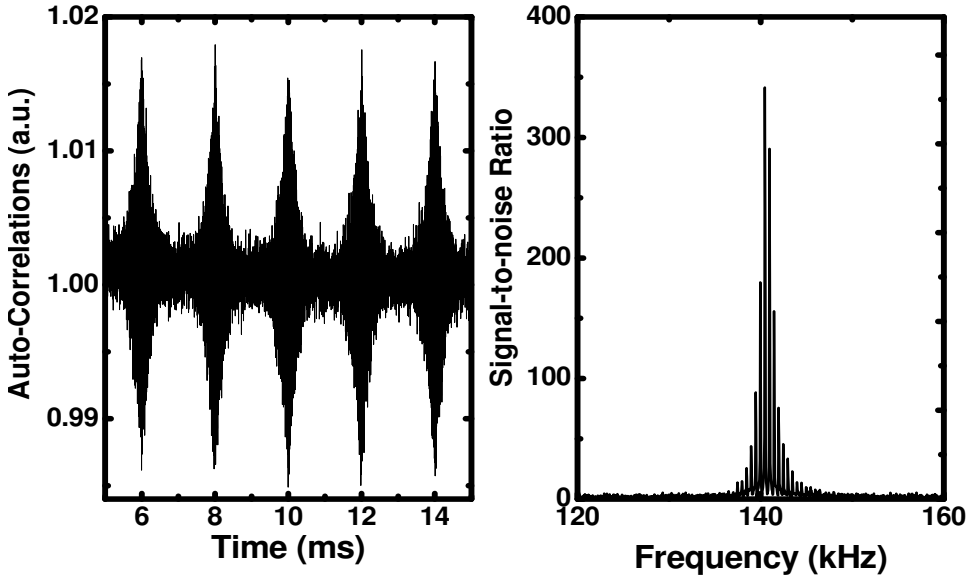

Figure 6.14: Auto-correlation measurement and motional spectrum of a three-dimensional ion crystal. The laser detuning is -150 MHz, the laser power is 25 μW, the excitation amplitude is 2 V, the repetition rate is 500 Hz, the pulse width is 3 μs and the interrogation time is 5 s.

by the temperature drift of the trap and the stability of the DC-endcap supply, which is $<0.01\%/\mathrm{hr}$[3].

We have demonstrated that this method produces accurate measurements of the COM-mode frequency of short ion strings as well as large three-dimensional ion crystals. The heat introduced into the ions' motion is small, so that the crystal state of the ions is maintained and even configurations of small mixed ion crystals are stable during the measurement. Employing a mixed two-ion string, we were able to measure the mass of a dark ion with respect to the mass of a ^{40}Ca-ion trapped alongside the dark ion to better than 0.08 amu. In a five-ion crystal consisting of four ^{40}Ca-ions and one dark ion, we were

[3]SRS PS300 series HV power supply

able to resolve the COM-mode frequencies for the three unique configurations. The heating of the ion string due to the interrogation was low enough to maintain the configuration while still providing accurate frequency measurements. These frequencies were used to determine the mass of the dark ion.

This simple non-invasive technique is especially suited for novel applications, most notably cold chemistry with ions, high resolution spectroscopy and the measurement of the charge-to-mass ratio of ions. The next chapter describes the application of this technique to the measurement of low energy ion-neutral reaction rates.

Chapter 7

Charge exchange reactions

7.1 Introduction

A typical experiment for studying cold chemical reactions involves trapped molecular ions sympathetically cooled by Doppler cooled atomic ions. In this scheme, the molecular ions form a highly localised target with a temperature on the order of mK. A beam of neutral molecules can be intersected with the molecular ion target to produce reactions within the ion crystal. A variety of experimental techniques including Stark deceleration, Zeeman slowing, buffer gas cooling and quadrupole guiding can be used to control the internal and/or external energy of the neutral molecules in the beam [2, 1].

Reactions, occurring when a neutral molecule from the beam collides with a molecular ion in the crystal, can result in changes to the charge-to-mass ratio of the crystal as well as changes to the configuration of the ions within the crystal. For reactions which change the configuration of the crystal, EMCCD images taken before and after the reaction may be observed and compared to molecular dynamics simulations to confirm the result of the reaction [40, 30, 98]. In addition, the secular frequency of the ion crystal may be probed before and after the reaction in order to determine changes in the charge-to-mass ratio of the crystal [45, 46]. This may be advantageous, since reactions can be detected even if they don't result in a configuration change. Secular frequency probing can be performed rapidly and with high precision using the ion crystal weighing technique. In effect, reactions can be measured continuously throughout the course of an experiment simply by monitoring the COM-mode frequency.

The high resolution and short interrogation time of the ion crystal weighing technique described in the previous chapter makes it useful for measuring small changes in the COM-mode frequency of ion crystals. The measurement induced temperature increase can be

kept low, as shown in Sec. 6.4.6. Thus, large three-dimensional ion crystals containing several hundred ions can be interrogated with high precision without compromising the crystal structure. By continuously collecting auto-correlation spectra of ion crystals undergoing pulsed electronic excitation, we have access to a tool which can precisely detect any change in the average charge-to-mass ratio on a single particle level. In effect, this technique is very well suited for studying cold ion-atom collisions [106, 107, 108] and ultra cold chemical reactions [36, 35].

We have performed experiments involving charge exchange reactions between calcium isotopes. We have observed single particle reactions in high resolution and measured the cross section of a charge exchange reaction.

7.2 Measurement principle

In contrast to small ion strings, the COM-mode frequency shift due to changes in the configuration of the three-dimensional ion crystal is negligible. Thus, for a crystal that consists of multiple ion species the COM-mode frequency can be approximated by:

$$\omega_{\mathrm{COM}} = \omega_0 \sqrt{\frac{m_0}{q_0}\frac{\langle q\rangle}{\langle m\rangle}}\,, \tag{7.1}$$

where q_0/m_0 is the charge-to-mass ratio of the reference ion, $\langle q\rangle$ and $\langle m\rangle$ are the average charge and mass of the crystal, ω_0 is the axial secular frequency of a single reference ion and m_0 is the mass of the reference ion. In low-energy charge exchange collisions between calcium isotopes, the electric charge of the ions will stay constant but the mass of the crystal may change. If we assume that all of the ions in the crystal have equal charge, then $\langle q\rangle = q_0$ and Equ. 7.1 becomes

$$\omega_{\mathrm{COM}} = \omega_0 \sqrt{\frac{m_0}{\langle m\rangle}}\,. \tag{7.2}$$

For a pure crystal $\langle m\rangle = m_0$ and the COM-mode frequency is equal to the reference frequency ω_0. For a harmonic confining potential, this is true regardless of the spatial extent of the crystal and the number of ions it contains. The average mass of a two species ion crystal is

$$\langle m\rangle = \frac{m_0 \cdot N_0 + m_i \cdot N_i}{N_0 + N_i}\,, \tag{7.3}$$

where N_0 and N_i are the number of ion (0) and ion (i) contained in the crystal respectively and m_0 and m_i are the ion masses. Therefore, the COM-mode frequency can be expressed by

$$\omega_{\mathrm{COM}} = \omega_0 \sqrt{\frac{N_i + N_0}{N_i \cdot (m_i/m_0) + N_0}}. \tag{7.4}$$

Hence, any change in the number of either isotope contained within the crystal will result in a shift of the crystal's COM-mode frequency. The ratio of the number of each isotope in the crystal can be found by rearranging Equ. 7.4 to give:

$$\frac{N_i}{N_0} = \frac{1-\alpha^2}{\alpha^2 \cdot (m_i/m_0) - 1}, \tag{7.5}$$

where

$$\alpha = \frac{w_{\mathrm{COM}}}{w_0}. \tag{7.6}$$

In effect, by measuring the COM-mode frequency of the ion crystal the population ratio can be determined provided the crystal contains two ions of known masses.

7.3 Experimental set-up

Since ^{40}Ca and ^{44}Ca are the most abundant calcium isotopes, the simplest charge exchange experiment to prepare involves a mixed species ion crystal containing Doppler cooled ^{40}Ca-ions and sympathetically cooled ^{44}Ca-ions exposed to a constant flux of neutral calcium atoms. The atomic oven, discussed in Sec. 4.1.2, contains naturally abundant calcium atoms and is used both to prepare the ion crystals and to supply the beam of neutral atoms during charge exchange experiments.

Fig. 7.1 shows a schematic of the experimental set-up. Positive and negative square pulses are applied to the two endcap electrodes to excite the COM-mode motion of trapped ions and the motional spectrum is measured according to the procedure discussed in Sec. 6.2. The Doppler cooling lasers and photo-ionisation lasers are aligned along the trap axis and ion fluorescence is measured with either the PMT or the EMCCD. The separation of the oven opening and the collimator has been measured by photographing the set-up within the vacuum chamber. The distance scale is calibrated by photographing a ruler at an equivalent distance. The separation of the collimator and the centre of the trap is measured from a three-dimensional model of the trap and a tolerance of 0.5 mm is set by the machining.

Calcium ions are loaded into the trap using two stage photo-ionisation of neutral calcium atoms, as discussed in Sec. 3.2.2. Fig. 7.2 shows the fluorescence spectrum of the naturally abundant neutral calcium atomic beam as a function of the first stage photo-ionisation laser wavelength, which drives the $^1\mathrm{S}_0 \rightarrow {}^1\mathrm{P}_1$ transition. The second stage photo-ionisation laser is blocked and the atomic fluorescence is collected with the PMT. A Voigt profile is fit to each peak in the spectrum and the resonance wavelength of each

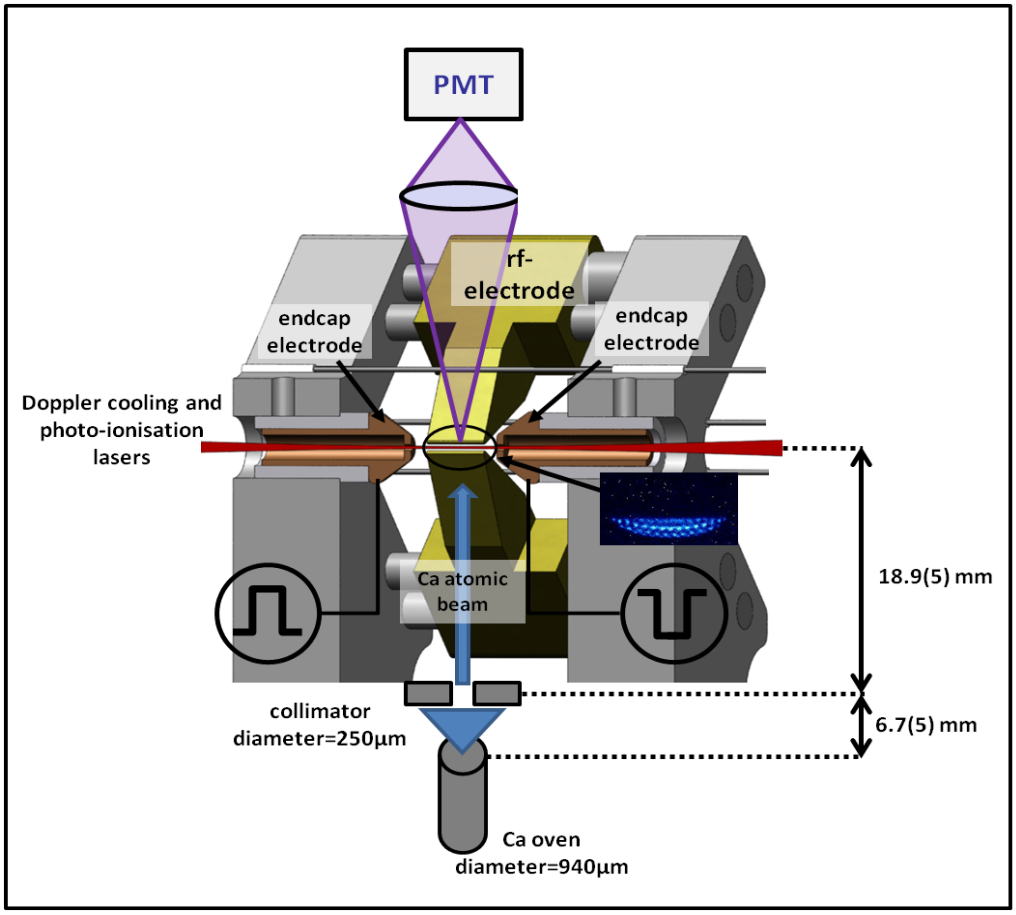

Figure 7.1: Experimental set-up used for studying charge exchange reactions within the ion trap. The ion trap is shown in cross section. Calcium atoms effusing from the oven are collimated by a 250 μm circular aperture located 6.7(5) mm from the oven opening. The distance between the collimator and the centre of the ion trap is 18.9(5) mm. The COM-mode frequency of an ion crystal is monitored by applying pulsed excitation to the endcap electrodes and recording the fluorescence modulation. Charge exchange reactions occur when neutral atoms in the beam collide with the ions in the crystal.

calcium isotope peak is determined along with the corresponding frequency shift with respect to the ^{40}Ca peak. The ^{43}Ca and ^{46}Ca peaks are not visible in the spectrum due to their low natural abundance and due to the distrubution of population into the three hyperfine components of the ^{43}Ca $^1S_0 \rightarrow {}^1P_1$ transition. Table 7.1 lists the literature values for the abundances of each calcium isotope along with the shift of the $^1S_0 \rightarrow {}^1P_1$ transition frequency with respect to the resonance of ^{40}Ca.

In order to prepare the mixed crystal, the calcium oven is operated at a power of approximately 2 W, the first stage photo-ionisation laser wavelength is tuned to the $^1S_0 \rightarrow {}^1P_1$ transition resonance of ^{44}Ca and the second stage photo-ionisation laser is switched on. Due to an overlap of the ^{44}Ca and ^{40}Ca $^1S_0 \rightarrow {}^1P_1$ transition resonances, some ^{40}Ca-ions are inevitably loaded during the preparation of the $^{44}Ca^+$ crystal. In addition, charge

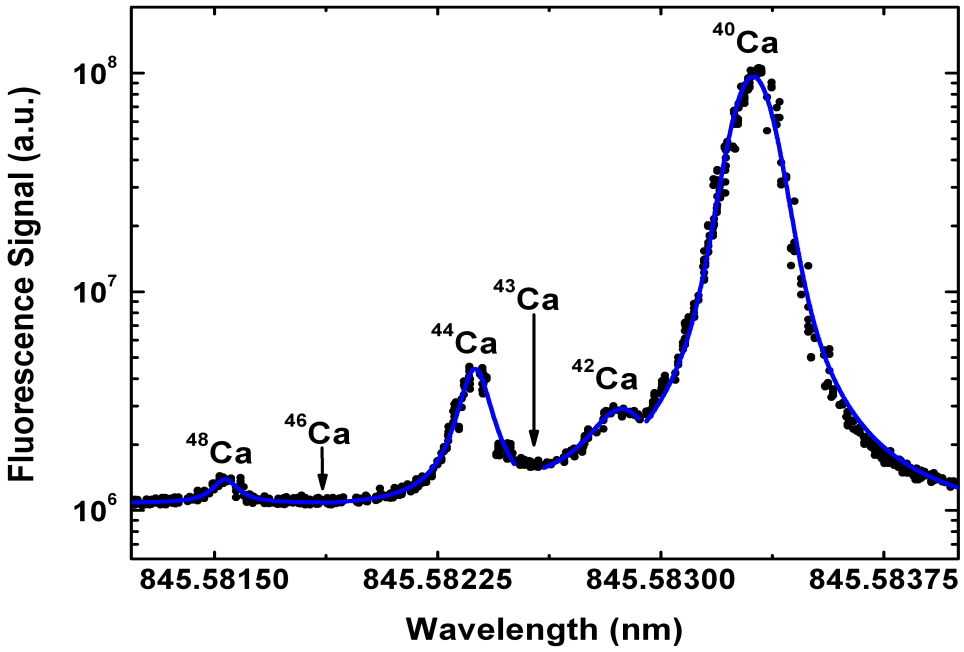

Figure 7.2: Fluorescence spectrum of the naturally abundant calcium atomic beam as a function of the wavelength of the frequency doubled 845 nm first stage photo-ionisation laser. The location of each calcium isotope is indicated. The ^{43}Ca and ^{46}Ca peaks are not visible in the spectrum, but their approximate location is indicated by the arrows.

Mass No	Natural Abundance [60]	Isotope Shift (MHz) [109]
40	96.9%	-
42	0.647%	394
43(c.g.)	0.135%	612
44	2.09%	774
46	0.004%	1160
48	0.187%	1513

Table 7.1: Natural abundances and the shifts of the $^1S_0 \rightarrow {}^1P_1$ transition frequency with respect to the resonance of ^{40}Ca for each of the naturally occurring calcium isotopes.

exchange collisions between ions in the crystal and atoms in the atomic beam may occur during the loading process. The calcium oven power and photo-ionisation laser parameters are empirically optimised to produce ion crystals containing between 100 and 150 ions with a typical $^{44}Ca^+$ population of 65%. The loading process typically takes between three and five minutes and following loading the calcium oven is switched off. Smaller mixed crystals, containing tens of ions, can be loaded within about one minute.

The Doppler cooling and re-pumping laser wavelengths are tuned to cool ^{44}Ca-ions during the loading process. Table 7.2 lists the experimentally measured resonance wavelengths for the $^{44}Ca^+$ transitions relevant for Doppler cooling. Once the crystal has been loaded, the Doppler cooling lasers are re-tuned to cool the ^{40}Ca-ions. The COM-mode fre-

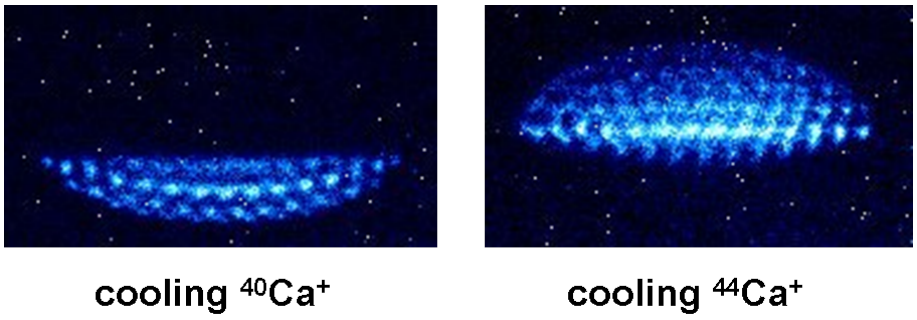

Figure 7.3: An ion crystal containing a mixture of ^{40}Ca-ions and ^{44}Ca-ions. During loading, the lasers are tuned to cool $^{44}Ca^{+}$. Following loading, the lasers are tuned to cool $^{40}Ca^{+}$. For the purposes of these photographs, the crystal has been radially displaced from the trap centre in order to spatially separate the two calcium isotopes.

Transition	Resonance Wavelength (nm)
$4S_{1/2} \rightarrow 4P_{1/2}$	396.95851(1)
$3D_{3/2} \rightarrow 4P_{3/2}$	850.0458(5)
$3D_{5/2} \rightarrow 4P_{3/2}$	854.4563(5)

Table 7.2: Experimentally measured resonance wavelengths for the transitions used for Doppler cooling ^{44}Ca-ions.

quency is measured before and after re-tuning the Doppler cooling lasers to detect changes in the crystal composition in the unlikely event of ion loss during the re-tuning process. A typical ion crystal contaning a mixture of $^{40}Ca^{+}$ and $^{44}Ca^{+}$ is shown in Fig. 7.3. In order to illustrate the composition of the ion crystal, it has been radially displaced from the trap centre so that the two isotopes become well separated. The lighter ^{40}Ca-ions experience a stronger confinement and therefore assemble on the side of the crystal nearest to the trap centre.

Since the atomic flux from the oven consists primarily of ^{40}Ca, the most likely charge exchange event that results in a change in the average charge-to-mass ratio is the $^{44}Ca^{+} + {}^{40}Ca \rightarrow {}^{40}Ca^{+} + {}^{44}Ca$ reaction.

7.4 Single event detection

To demonstrate the detection of single charge exchange reactions, a small crystal containing seven ^{44}Ca-ions and seven ^{40}Ca-ions is exposed to a flux of neutral calcium atoms. Following loading, the initial crystal composition is confirmed by observing the ^{40}Ca-ions with the EMCCD camera and by measuring the COM-mode frequency. The initial number of ^{44}Ca-ions is then calculated from Equ. 7.4. The oven is operated at a power of 1.5 W

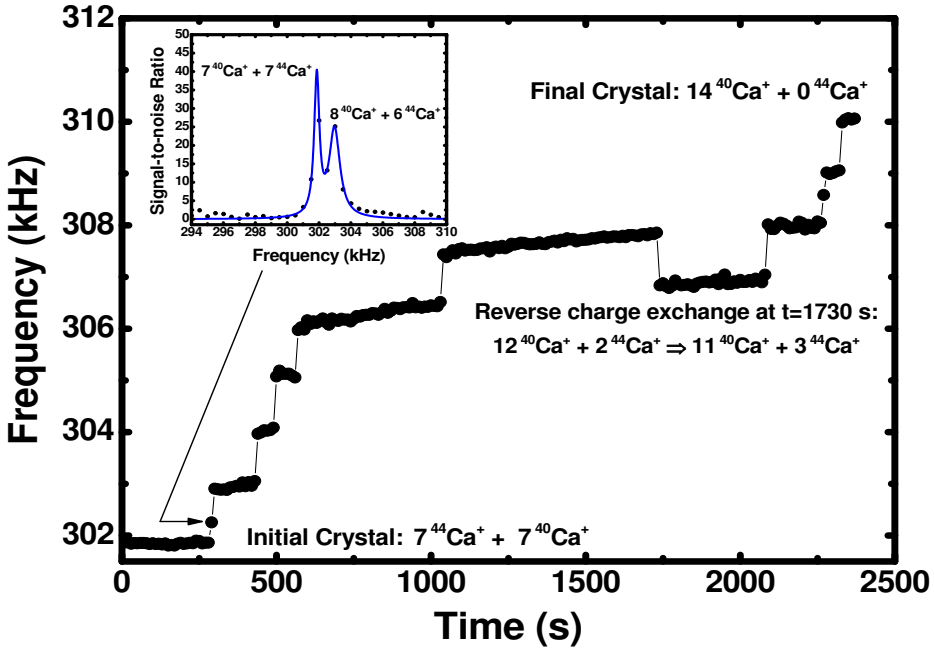

Figure 7.4: The COM-mode frequency of a mixed ion crystal during exposure to the neutral calcium atomic flux. The motional excitation has an amplitude of 2 V, a pulse width of 2 μs and a repetition rate of 500 Hz. This particular measurement includes a rare reverse charge exchange event that occurs at t=1730 s. Auto-correlation spectra are collected continuously and each measurement has an interrogation time of 10 s. The inset shows a motional spectrum with a double peak representing the axial frequency of the crystal before and after a charge exchange event.

to create the flux of neutral atoms. Pulsed excitation is applied to the DC-electrodes with an amplitude of 2 V, a pulse width of 2 μs and a repetition rate of 500 Hz. Auto-correlation spectra are collected continuously with an interrogation time of 10 s. Following the measurement, a Lorentzian function is fit to each collected motional spectrum.

Fig. 7.4 shows the COM-mode frequency of the ion crystal during the experiment. The steps in the frequency correspond to charge exchanges between ^{44}Ca-ions and neutral ^{40}Ca-atoms in the atomic beam. Even though there is a change in mass of only about 4% for each charge exchange, the change in frequency is clearly visible as a discrete step and each step corresponds to a frequency shift of around 1 kHz. Each COM-mode frequency shift occurring during the measurement is calculated by taking the difference between the measured frequency immediately following and immediately before the reaction. The corresponding change in the total mass of the crystal for each frequency shift is then calculated from Equ. 7.4. The measured frequency shifts for each reaction are listed in table 7.3 where they are compared with theoretical predictions. Since the uncertainty in

Crystal Population		Charge	Theoretical	Measured
$^{40}Ca^{+}$	$^{44}Ca^{+}$	Exchange Time (s)	Shift (kHz)	Shift (kHz)
8	6	300	1.03	1.08(6)
9	5	440	1.04	1.04(4)
10	4	500	1.05	1.04(5)
11	3	570	1.06	1.04(6)
12	2	1040	1.08	1.05(5)
11	3	1740	1.08	1.06(6)
12	2	2090	1.08	1.05(5)
13	1	2280	1.09	1.09(4)
14	0	2330	1.10	1.08(6)

Table 7.3: The experimentally measured frequency shift for each charge exchange event that occurs during the measurement shown in Fig. 7.4. Theoretical shift values are calculated from Equ. 7.4 for the known crystal population at t=0. The charge exchange time is taken as the time of the frequency measurement immediately following the reaction.

the experimentally measured crystal mass difference following each reaction is less than 1 a.m.u., the result of each reaction can be positively identified.

This method is particularly suited to detect rare events like the reverse charge exchange $^{44}Ca^{+} + {}^{40}Ca \rightarrow {}^{40}Ca^{+} + {}^{44}Ca$ which leads to a decrease of the COM-mode frequency. This event is visible in Fig. 7.4 as a shift to a lower COM-mode frequency at 1730 s. In addition, due to the single event resolution of this technique, the time resolution can be improved beyond the interrogation time of each measurement. By analysing the spectra, the exact moment an event has occurred can be deduced from the ratio of the amplitude of the frequency peak before and after the event. The inset in Fig. 7.4 shows a motional spectrum with two peaks of approximately the same amplitude. This indicates that the charge exchange reaction took place nearly halfway through the 10 s interrogation. Double peaks are present in the motional spectra for each reaction. In the case of a double peak, the routine used to analyse the data has assigned the frequency of the larger amplitude peak to the data point.

The plateau regions in Fig. 7.4, during which no charge exchange events occur, are slightly inclined due to the change in temperature of the ion trap caused by the resistively heated oven, which is in thermal contact with the trap mount. The observed drift in the frequency, however, is easily distinguishable from the discrete jumps of the COM-mode frequency resulting from charge exchange events.

The detection of single reaction events is limited by the number and mass of the ions contained in the crystal, the reference frequency ω_0 and the precision of the COM-mode frequency measurement. A detectable reaction must result in a modified crystal mass and

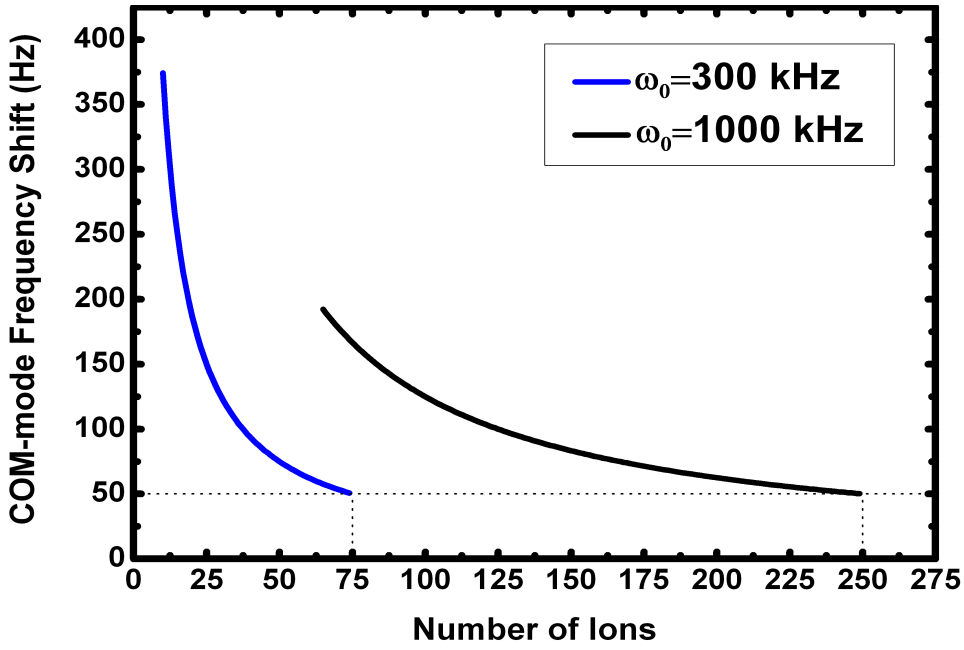

Figure 7.5: The COM-mode frequency shift following a 1 a.m.u. increase in the total mass of a crystal of ^{40}Ca-ions as a function of the number of ions in the crystal. The COM-mode frequency shift is inversely proportional to the number of ions in the crystal and linearly proportional to the reference frequency ω_0.

the smallest change is the addition or subtraction of 1 a.m.u. The change in the average mass of the crystal is inversely proportional to the number of ions it contains as shown by Equ. 7.3. For larger ion crystals, the COM-mode frequency shift resulting from a reaction may be lower than the measurement precision. This effect can be compensated by increasing the reference frequency ω_0. From Equ. 7.4, the change in the COM-mode frequency of the crystal due to a reaction is linearly proportional to the reference frequency. Therefore, maximising ω_0 maximises the single event resolution.

Fig. 7.5 shows the change in COM-mode frequency resulting from a change of 1 a.m.u. in the total mass of the ion crystal as a function of the number of ions in the crystal. The ions in the crystal are $^{40}Ca^+$ with $m_0 = 40$ with the addition of a single ion that has acquired a new mass $m_i = 41$ following a reaction. Setting the precision limit of the COM-mode frequency measurement to 50 Hz, the maximum ion crystal size allowing detection of the reaction is 75 ions when using a reference frequency of 300 kHz. For a reference frequency of 1 MHz, the maximum crystal size becomes 250 ions. A 1 a.m.u. change in the total mass of a 1000 ion crystal gives a COM-mode frequency shift of 50 Hz when a reference frequency of 4 MHz is employed. Secular frequencies on the order of MHz are commonly used in ion traps. Therefore, the single event detection demonstrated here with a 14 ion crystal and a secular frequency around 300 kHz is readily scalable to

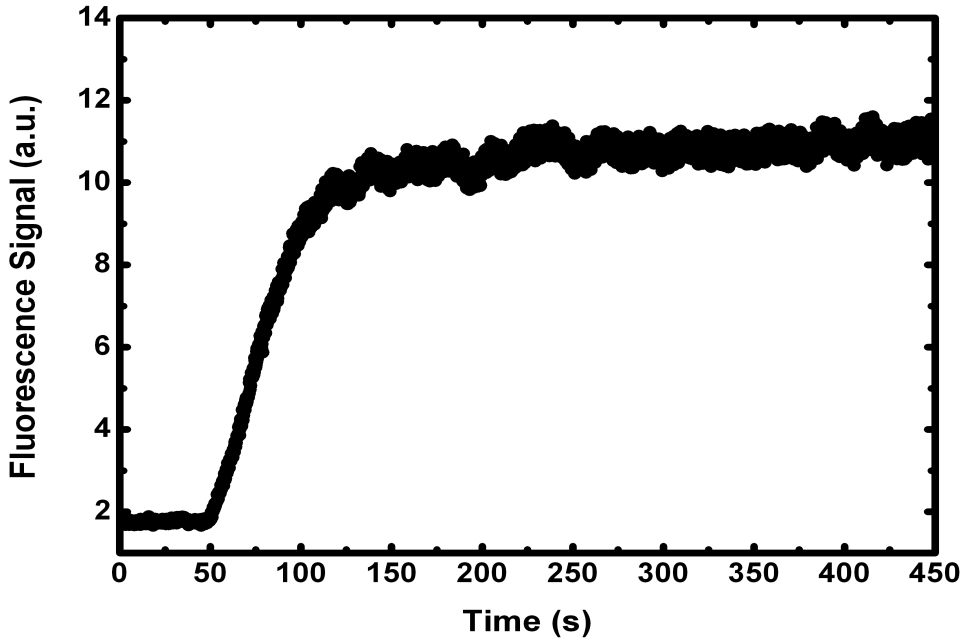

Figure 7.6: The atomic fluorescence rate as a function of the time elapsed since the application of a current through the calcium oven. A current of 1.65 A, corresponding to a power of 2.1 W, is used. The first stage photo-ionisation laser is tuned to the resonance of the ^{40}Ca $^1S_0 \rightarrow {}^1P_1$ transition and fluorescence is collected with the PMT. For t>200 s the atomic flux remains approximately constant.

experiments involving ion crystals containing several hundred ions.

7.5 $^{44}Ca^+ + {}^{40}Ca \rightarrow {}^{40}Ca^+ + {}^{44}Ca$ reaction cross section

The rate of the $^{44}Ca^+ + {}^{40}Ca \rightarrow {}^{40}Ca^+ + {}^{44}Ca$ charge exchange reaction can be measured by precisely monitoring the time evolution of the population ratio of a mixed species calcium ion crystal during exposure to the neutral calcium atomic flux.

In order to determine the charge exchange cross section, a constant flux of neutral calcium atoms passing through the centre of the ion trap is required and the spatial distribution of neutral atoms within the trapping region must be constant. In addition, the atomic flux produced by the oven must be measured.

7.5.1 Oven warm-up

The warm-up time of the oven is defined as the time difference between the application of a current through the oven and the effusion of calcium atoms from the oven at a constant rate. As the temperature of the oven increases, the effusion rate increases until the oven reaches its constant operational temperature. We measure the warm-up time

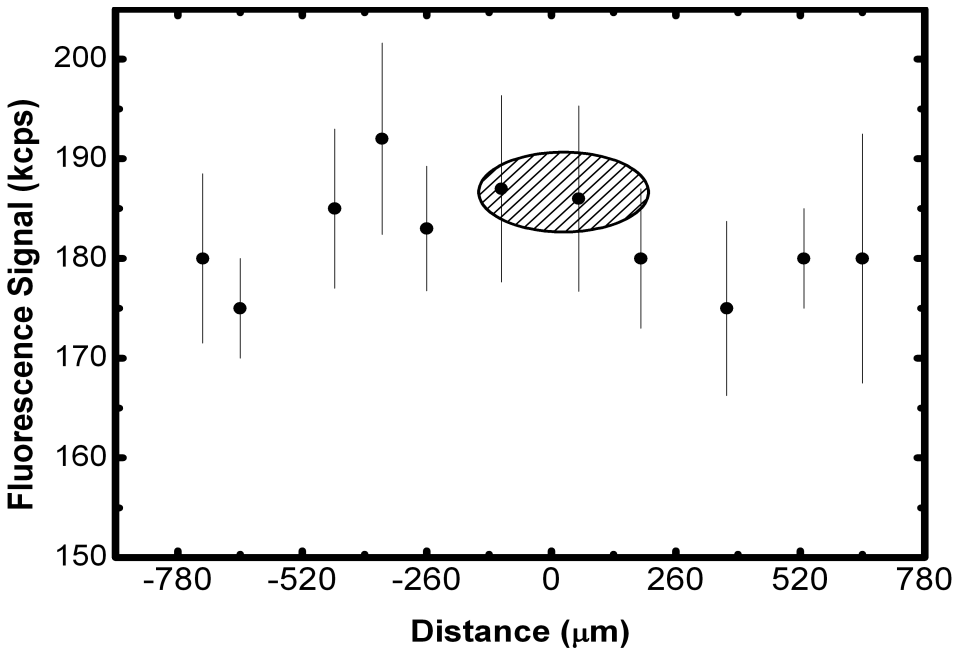

Figure 7.7: The atomic fluorescence signal as a function of the location of the focus of the orthogonally aligned first stage photo-ionisation laser. The laser is translated along the trap axis using a pair of mirrors. Each data point is the mean amplitude of ten atomic fluorescence spectra. The error bars are the standard deviation of each data set. The oval represents the location and spatial extent of an ion crystal containing several hundred ions with +500 V applied to both endcap electrodes. The data establishes that the atomic flux is uniformly distributed throughout the trapping region.

by measuring the fluorescence rate of the atomic beam. A laser tuned to the $^1S_0 \rightarrow {}^1P_1$ transition of ^{40}Ca is aligned through the trap centre orthogonal to the atomic beam and the atomic fluorescence rate is measured with the PMT. The laser frequency is locked to the resonance of the transition using feedback from the wavemeter and the measured fluorescence rate is proportional to the magnitude of the atomic flux.

Fig. 7.6 shows the atomic fluorescence rate as a function of the time elapsed since the application of a current through the oven. A current of 1.65 A, corresponding to a power of 2.1 W, is applied to the oven at t=0 s. A fluorescence signal is measured after approximately 50 s. The magnitude of the fluorescence signal then increases rapidly until it reaches a nearly constant value around t=200 s. For t>200 s, the flux of atoms through the trap centre remains approximately constant. In order to ensure that the charge exchange rate is measured for a constant flux, any reactions occurring within the ion crystal before 200 s has elapsed since the application of a current through the oven must be disregarded. In effect, the initial state of the mixed ion crystal is given by the population ratio at t=200 s after the application of a current through the oven.

7.5.2 Spatial flux distribution

We measure the magnitude of the atomic flux as a function of position along the ion trap axis in order to determine the spatial distribution of atoms in the atomic beam. A laser tuned to the resonance of the $^1S_0 \rightarrow {}^1P_1$ transition of ^{40}Ca is aligned orthogonal to the trap axis and focused to a spot size of 50(5) μm at the trap centre. The oven is operated continuously at a power of 2.1 W throughout the measurement. Ten fluorescence profiles of the $^1S_0 \rightarrow {}^1P_1$ transition are measured by scanning the laser frequency and collecting fluorescence with the PMT. The laser is then translated to a new position on the trap axis with a pair of mirrors. Each position of the laser along the trap axis is determined by taking an EMCCD image of the atomic fluorescence and finding the centre of the laser spatial profile.

Fig. 7.7 shows the atomic fluorescence signal for each position of the laser along the trap axis. Each data point is the mean amplitude of the ten measured fluorescence spectrums and the error bars are the standard deviation of each data set. The oval represents the location and spatial extent of an ion crystal containing 250 ions. The x-axis has been converted from pixels to metres using a separate EMCCD image of the separation of two ions with a precisely known axial frequency.

The results in Fig. 7.7 confirm that the ion crystal resides in a region of constant atomic flux. Therefore, the probability of a charge exchange reaction occurring at any location within the crystal is constant.

7.5.3 Temperature drift

Since the calcium oven is in thermal contact with the ion trap mount, heat diffuses to the trap structure during oven operation. As shown in Fig. 7.4, the temperature increase of the trap components results in a drift of the ion crystal's COM-mode frequency. This drift is always positive and the COM-mode frequency of a single ion is observed to increase with time as the temperature of the oven and the trap structure increase. Therefore, we conclude that the net effect of thermal expansion is a reduction of the separation of the endcap electrodes and a subsequent increase in the depth of the axial potential. For the experiment shown in Fig. 7.4, the frequency drift does not compromise the identification of single charge exchange events. However, for the current experiment, where single events are not resolvable, the frequency drift introduces a systematic error in the measurement of the time evolution of the ion crystal's COM-mode frequency.

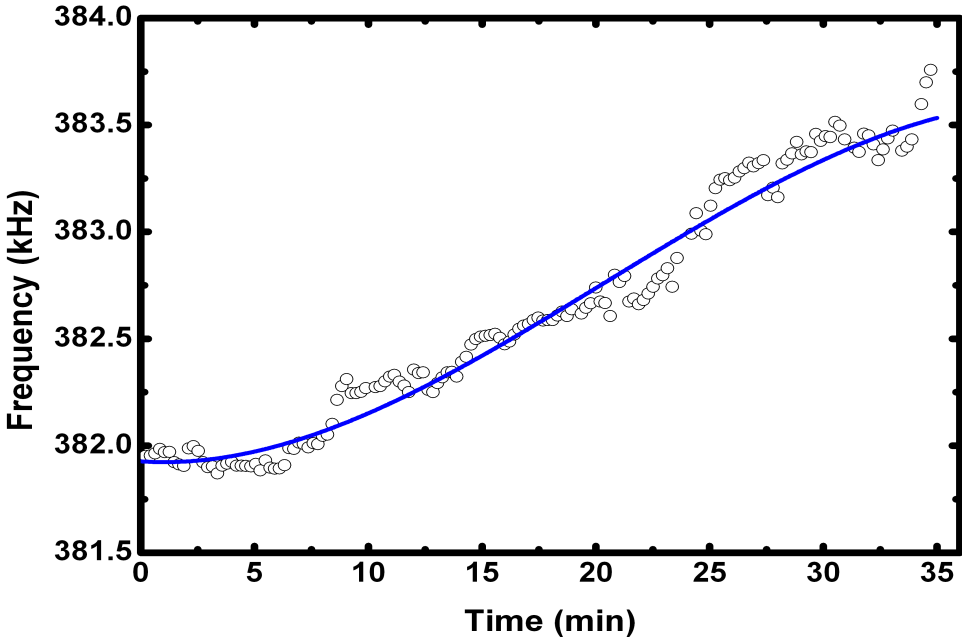

Figure 7.8: The COM-mode frequency of a single ion as a function of time since the application of a current through the oven. The frequency is measured with an interrogation time of 5 s at 20 s intervals and a cubic function is fit to the data (solid line).

We measure the time dependence of the frequency drift using a single ion as a probe for the time scales used in our experiment. Fig. 7.8 shows measurements of the COM-mode frequency of a single ^{40}Ca ion as a function of the time since the application of a current to the oven. The COM-mode frequency is measured with an interrogation time of 5 s at 20 s intervals with an excitation pulse amplitude of 3.5 V, a pulse width of 1.5 μs and a repetition rate of 1 kHz. The oven is operated at a current of 1.65 A, corresponding to a power of 2.1 W. The data has been fit with a cubic function:

$$\omega_{\mathrm{drift}}(t) = a + bt + ct^2 + dt^3 \tag{7.7}$$

where a, b, c and d are the fitting parameters. The measurement is repeated ten times and the mean and standard deviation of each fitting parameter is determined. Since the measurements are consistent, Equ. 7.7 can be employed as a time dependent correction to the measured COM-mode frequency of the ion crystal such that

$$\omega_{\mathrm{COM}}(t) = \omega^{\mathrm{M}}_{\mathrm{COM}}(t) - \omega_{\mathrm{drift}}(t), \tag{7.8}$$

where $\omega^{\mathrm{M}}_{\mathrm{COM}}(t)$ is the measured COM-mode frequency, $\omega_{\mathrm{drift}}(t)$ is the COM-mode frequency drift due to the trap temperature at time t and $\omega_{\mathrm{COM}}(t)$ is the corrected COM-mode frequency of the ion crystal at time t.

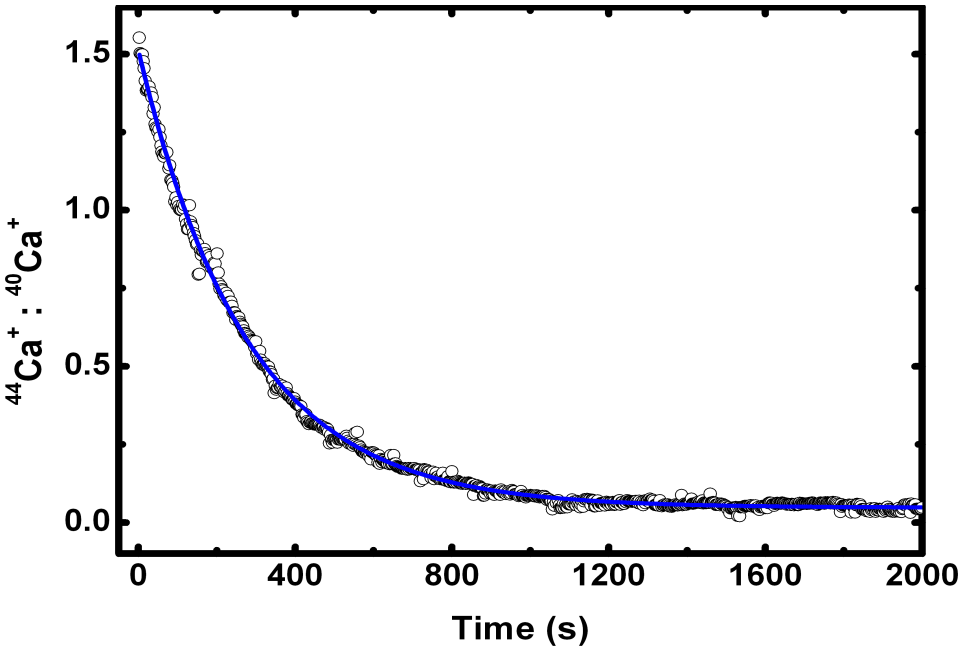

Figure 7.9: The ratio of ^{44}Ca ions to ^{40}Ca ions within the mixed crystal during exposure to the calcium atomic flux. A current of 1.65 A, corresponding to a power of 2.1 W, is applied to the oven at time t=-200 s. Each data point represents a COM-mode frequency measurement with an interrogation time of 2.5 s. Equ. 7.9 has been fit to the data (solid line) giving a decay constant of 278(1) s and a charge exchange rate of 0.0036(1) ions/s.

7.5.4 Charge exchange rate

We have measured the cross section of the $^{44}Ca^{+} + {}^{40}Ca \rightarrow {}^{40}Ca^{+} + {}^{44}Ca$ charge exchange reaction by constantly measuring the COM-mode frequency of two-species ion crystals during exposure to the neutral calcium atomic flux. The ion crystals contain between 100 and 200 ions with a typical initial population of 35% $^{40}Ca^{+}$ and 65% $^{44}Ca^{+}$. A trap secular frequency of 382 kHz is used and single events are not resolvable during the experiment due to the number of ions in the crystal. However, from Equ. 7.5 the ratio of the populations of the two species in the ion crystal can be monitored as they evolve following charge exchange reactions. The pulsed excitation has an amplitude of 2 V, a pulse width of 2 μs and a repetition rate of 1 kHz. The interrogation time of each COM-mode frequency measurement is 2.5 s. For each measured COM-mode frequency, the ratio of the $^{44}Ca^{+}$ population to the $^{40}Ca^{+}$ population is calculated using Equ. 7.5 where $\omega_{\mathrm{COM}}(t)$ is calculated from Equ. 7.8. Since we are only concerned with the rate of change of the population ratio, it is not necessary to measure the exact populations of the two calcium isotopes throughout the experiment.

Fig. 7.9 shows the population ratio as a function of exposure time to the calcium flux. Each data point corresponds to a single measurement of the crystal's COM-mode

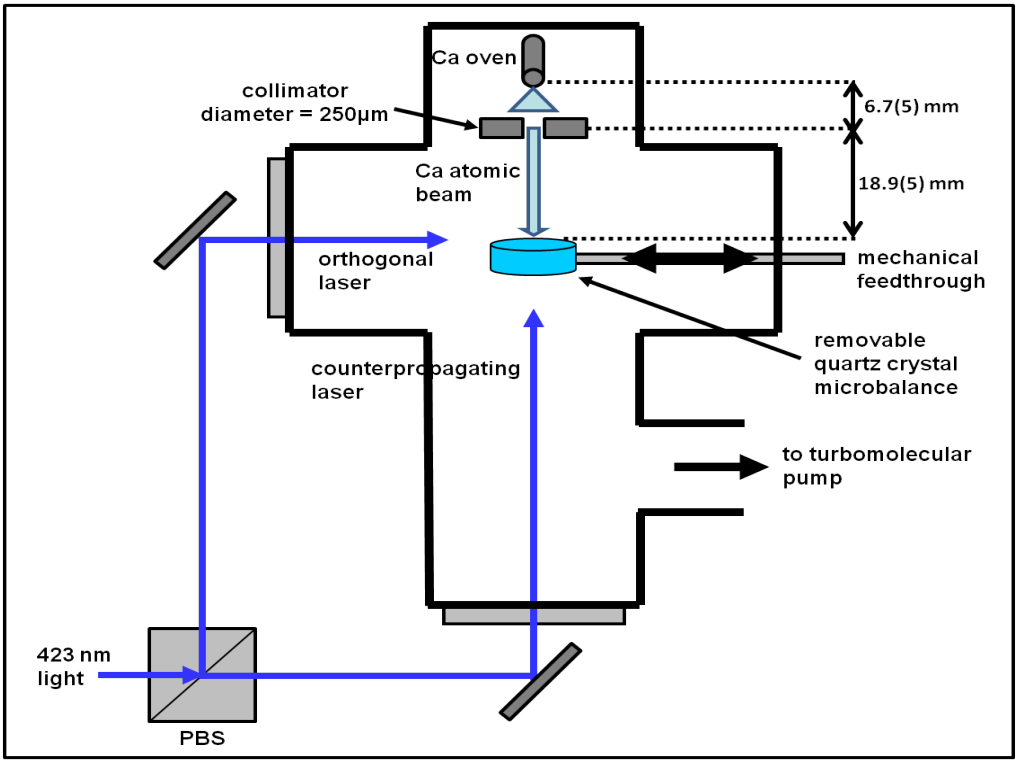

Figure 7.10: Experimental set-up used for measuring the calcium atomic flux. The oven used during the charge exchange experiments, a collimator and a quartz crystal oscillator are mounted within a five-way cross. The geometry is chosen to match the geometry of the ion trap set-up. A pair of windows allow laser access and a third window allows optical access from above for collecting atomic fluorescence. The position of the quartz crystal oscillator can be adjusted with the mechanical feedthrough.

frequency. The time t=0 has been set to 200 s after the initial application of current through the oven to ensure that reactions are only considered after the oven has reached its constant operational temperature. As ^{44}Ca-ions within the crystal are replaced by ^{40}Ca-ions, the population ratio decays to zero. The population ratio as a function of time can be expressed by

$$P(t) = P_0 \cdot \mathrm{e}^{-\sigma\Phi t}, \tag{7.9}$$

where P_0 is the initial population ratio, σ is the reaction cross section and Φ is the atomic flux. Equ. 7.9 is fit to the data in Fig. 7.9 to determine the time constant of the exponential decay. The measurement is repeated ten times and care is taken to ensure that the experimental procedure is identical for each measurement. The mean value of the exponential decay time constant is 269(10) s. This corresponds to a charge exchange rate of $\sigma \cdot \Phi = 0.0037(1)$ ions/s, where the error is the standard deviation of the data set. By precisely measuring the calcium atomic flux Φ, the charge exchange cross section σ can be determined from the result of the charge exchange rate measurement.

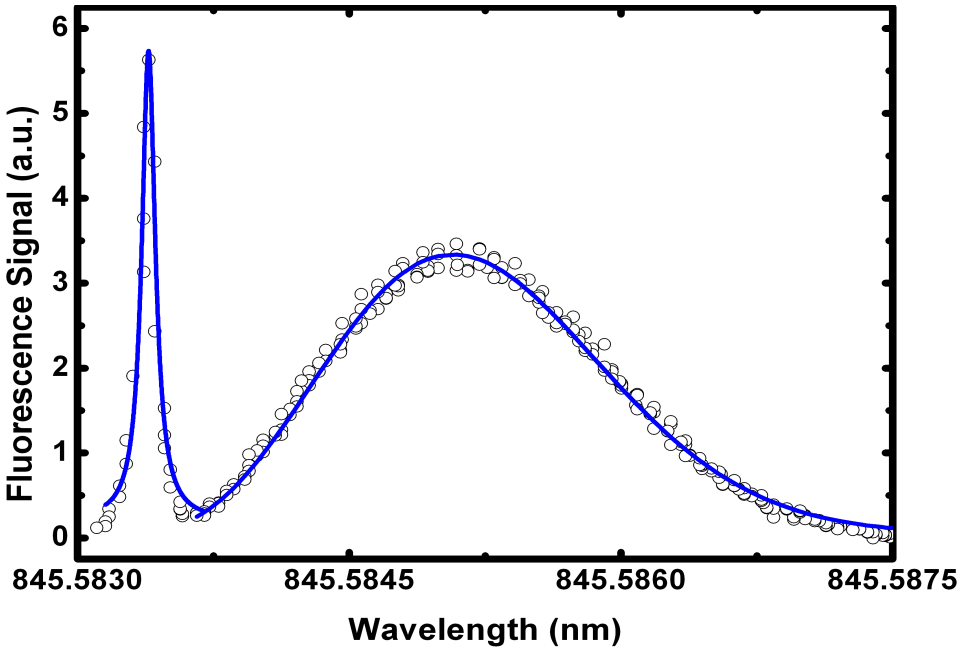

Figure 7.11: The calcium atomic fluorescence as a function of the wavelength of the frequency doubled first stage photo-ionisation laser. A Voigt profile is fit to the orthogonal peak and a Maxwell-Boltzmann distribution is fit to the counter-propagating profile. The temperature of the oven is determined from the fit.

7.5.5 Calcium flux

We have used two methods for measuring the calcium atomic flux. The first method is a calculation of the flux based on the experimentally measured temperature of the oven. The second method is a direct measurement of the flux using a quartz crystal microbalance.

Immediately following the charge exchange rate measurements, the calcium oven is removed from the ion trap chamber and installed in a separate test chamber. A schematic of the test chamber is shown in Fig. 7.10. The set-up consists of a five-way-cross that contains the oven, the atomic beam collimator and a quartz crystal microbalance. The separation of the collimator and quartz crystal microbalance matches the separation of the collimator and ion crystal in the ion trap set-up. A chamber pressure of around 10^{-7} mbar is maintained with a turbomolecular pump backed by a rotary pump. A pair of windows allow laser access and an additional window on top of the cross allows optical access for a PMT. The quartz crystal microbalance is mounted on an in-house designed mechanical feedthrough. The crystal may be positioned in the path of the atomic beam or may be moved out of the atomic beam path to allow laser access without the need to open the chamber.

The oven is characterised following the procedure described in Sec. 3.3. The first stage photo-ionisation laser is split with a polarising beam splitter so that one beam

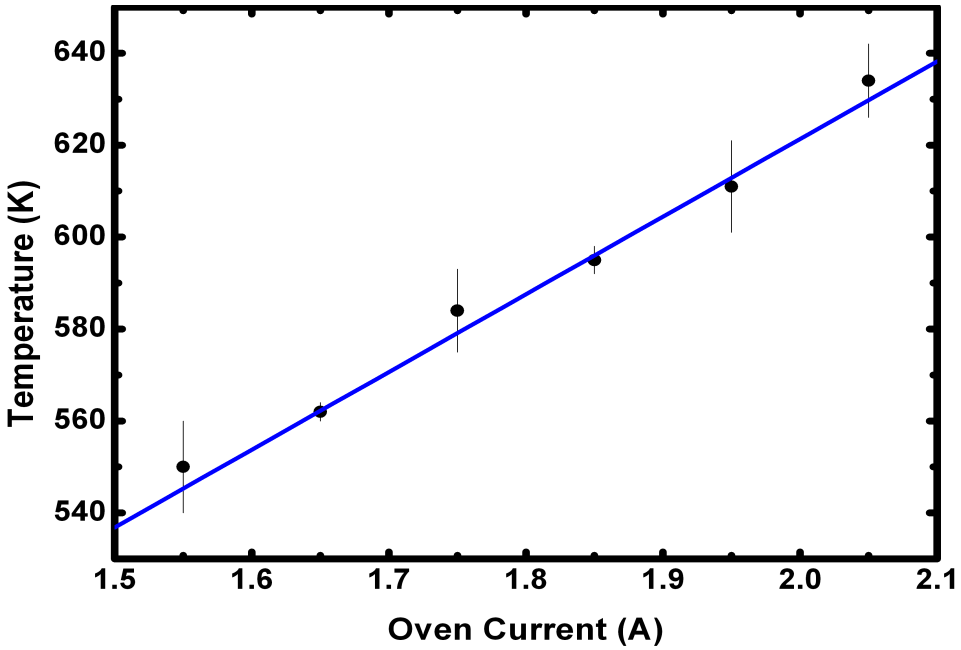

Figure 7.12: The oven temperature as a function of current. The relationship is linear for the range of currents used in this experiment.

can be aligned orthogonal with respect to the atomic beam and the other beam can be aligned counter-propagating with respect to the atomic beam. Fig. 7.11 shows an atomic fluorescence spectrum collected by scanning the wavelength of the laser for an oven current of 1.65 A, corresponding to a power of 2.1 W. A Maxwell-Boltzmann distribution has been fit to the counterpropagating fluorescence peak and a Voigt function has been fit to the orthogonal fluorescence peak. Fig. 7.12 shows the relationship between the oven current and the temperature for a range of currents. The fluorescence profile is measured ten times with a current of 1.65 A and a mean temperature of 562(2) K is calculated from the data set. The error bar is the standard deviation of the data set. This oven temperature corresponds to a most probable velocity of 341(1) m/s. For the other oven currents, the temperature is measured once in order to establish the linear relationship between temperature and current. The temperature extracted from the atomic beam profile is a high estimate of the oven temperature, since hotter atoms have a higher probability of escaping from the oven.

The flux of atoms from an idealised oven with a thin walled aperture of area A can be expressed as:

$$\Phi = 8.386 \times 10^{21} \frac{pA}{l^2\sqrt{MT}} \text{ atoms/cm}^2 \cdot \text{s} \tag{7.10}$$

where p is the oven source pressure in mbar, l is the distance from the oven aperture to the detector, M is the molecular weight, T is the oven temperature and the pre-factor includes

the Boltzmann constant and unit conversion constants [83]. The oven source pressure can be expressed as a function of the oven temperature by [84]:

$$p(T) = (7.5 \cdot 10^{-5}) 10^{(-\frac{10{,}170}{T} + 9.73)} \text{ mbar}. \tag{7.11}$$

The atomic beam intensity given by Equ. 7.10 is, in general, reduced by the inclusion of a collimator in the path between the source and the detector. A collimator is included in the experimental set-up, however, the data in Fig. 7.7 establishes that an unobstructed line of sight exists between the source aperture and the ion crystal. Therefore, an addition term is not required in Equ. 7.10. Inserting the measured oven temperature and the geometry factors from the experimental set-up into Equ. 7.10 gives an atomic flux of $2.1(4) \times 10^9$ atoms/(cm^2·s). From the measured charge exchange rate this gives a cross section of $1.8(3) \times 10^{-12}$ cm^2.

The atomic flux can also be estimated from the neutral atom fluorescence at 423 nm. The area of the resonance peak collected with a laser aligned orthogonal with respect to the calcium atomic beam is proportional to the flux of calcium atoms passing through the laser beam. In order to convert the area of the resonance peak into an absolute atomic flux, the spatial distribution of the laser intensity must be known in addition to the photon collection and detection efficiency. This method was not attempted due to the highly non-Gaussian spatial mode of the 423 nm light provided by the frequency doubling system used during these experiments (see Sec. 4.2). However, the technique can provide precise measurements of the atomic flux [110] and has been employed in commercially available flux monitors [1].

In order to directly measure the atomic flux, we have employed a quartz crystal oscillator[2] which we have placed at a distance of 18.9(5) mm from the atomic oven within the test set-up (see Fig. 7.10). The frequency of the oscillator is monitored while calcium effusing from the oven source is deposited onto the surface. By approximating the calcium deposition layer as an extension of the quartz crystal surface and assuming that the calcium is deposited uniformly over the surface, the increased mass of the crystal can be considered to be proportional to the change in the oscillation frequency. The change in frequency as a function of the change in mass is given by the Sauerbrey equation:

$$\Delta f = -\frac{2 f_0^2}{A\sqrt{\rho_q \mu_q}} \Delta m, \tag{7.12}$$

where f_0 is the resonance frequency of the oscillator, A is the surface area of the crystal, ρ_q is the density of quartz and μ_q is the shear modulus of quartz[111].

[1] SVT Associates, Inc. AccuFlux Deposition Flux Monitor

[2] Vishay Dale X0-52 half-size clock oscillator

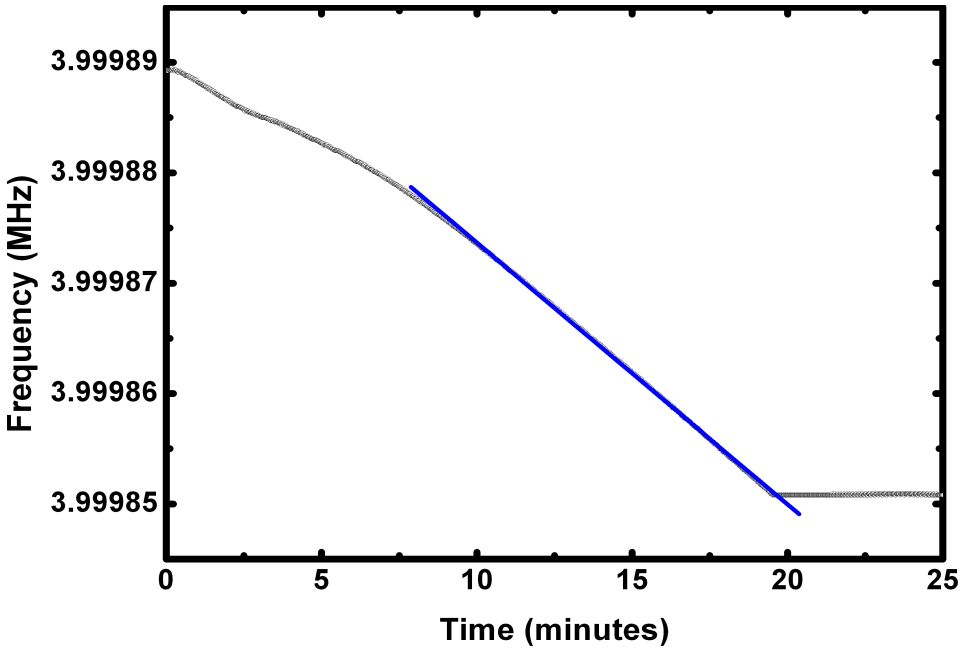

Figure 7.13: The oscillation frequency of a quartz crystal oscillator during exposure to the neutral calcium atomic beam. The oven is operated at a current of 1.65 A, corresponding to a power of 2.1 W. As calcium is deposited onto the crystal surface, the oscillation frequency changes according to Equ. 7.12. The oven is switched off after around 20 minutes and the oscillation frequency of the crystal stabilises. The total frequency change during the 671 second linear region (solid line) is -26.52 Hz.

The quartz crystal oscillator is coated with calcium by operating the oven at a current of 1.65 A, corresponding to a power of 2.1 W, while continuously measuring the crystal frequency. After the oven warm-up time has elapsed, the quartz crystal is positioned in the path of the atomic flux and the crystal frequency decreases with time as calcium is deposited onto the surface. The crystal frequency is measured at ten second intervals and Fig. 7.13 shows the relationship between frequency and time. After around ten minutes of deposition the change in frequency becomes nearly linear with time. The oven is switched off after around twenty minutes and subsequently the crystal frequency stabilises.

We have fit a linear function (solid line in Fig. 7.13) to the data between around ten minutes and twenty minutes. The frequency shift and time duration for the linear region are recorded. Inserting the frequency shift into Equ. 7.12 gives the mass of deposited calcium for a crystal resonance frequency of 4 MHz and a measured crystal surface area of 0.07(1) cm^2. From the duration of the linear region, this mass shift can be converted to a flux in units of atoms/(cm^2·s). The measurement is repeated five times with five different quartz crystal oscillators. The mean frequency shift of the crystal as a function of time is -0.04(2) Hz/s, where the error is the standard deviation of the data set. In principle, we would now use Equ. 7.12 to calculate the atomic flux. However, Equ. 7.12 makes naive

assumptions about the deposition process. We cannot assume that the deposited calcium layer is an extension of the quartz crystal surface, nor can we assume that the deposition is uniform over the large crystal area.

Instead of using the Sauerbrey equation to calculate the atomic flux, we have attempted to calibrate the quartz crystal oscillator for calcium deposition by independently measuring the absolute mass of a deposited calcium layer. If the frequency shift of the crystal as a function of absolute mass can be determined, the slope of the linear fits in the previous measurements can be converted to give the deposited mass as a function of time and thus the calcium flux.

We have measured the approximately linear frequency shift of an oscillator after depositing calcium for longer than two hours. The oven is operated at 2.5 A, corresponding to a power of 6.25 W, throughout the measurement. The total frequency shift of the crystal following deposition is -1045 Hz. After the experiment, the crystal is removed from vacuum and immediately placed into a 5 ml solution of 5% nitric acid. The solution removes the deposited calcium from the surface of the quartz crystal. The concentration of calcium in the solution is analysed using an inductively coupled plasma mass spectrometer (ICP-MS)[3]. Within the spectrometer, a precisely measured volume of the solution is injected into an argon plasma and guided by an rf-octopole guide. The concentration of individual ions within the plasma is measured by guiding them toward a detector while scanning the stability of the guide as a function of the charge-to-mass ratio of the ions.

The results of the measurement showed a concentration of calcium below the sensitivity of the spectrometer. This is primarily due to the fact that the spectrometer uses an argon plasma. The mass of ^{40}Ar (atomic weight 39.948 a.m.u.) and ^{40}Ca (atomic weight 40.078 a.m.u.) are similar enough to preclude the direct detection of the $^{40}Ca^{+}$ concentration in the plasma. ^{44}Ca, the next most abundant naturally occurring isotope, is detected instead and this reduces the calcium detection efficiency by a factor of around 100. However, the result places an upper limit of 100(10) ng on the total mass of the calcium deposited onto the crystal surface. From this, we can place an upper limit of 0.09(1) ng/Hz on the mass of deposited calcium as a function of the crystal frequency shift. Using the measured linear crystal frequency change as a function of time for an oven current of 1.65 A, this limits the calcium flux to less than $6(3) \times 10^{10}$ atoms/(cm^2·s). From this result, the charge exchange cross section must be greater than $6(3) \times 10^{-14}$ cm^2. The measured limit on the cross section is in agreement with the Langevin approximation, which predicts a cross section of

[3]Agilent 7500 Series ICP-MS

approximately $1.2 \times 10^{-11}/v$ cm^2,where v is in m/s [112]. However, due to the large error on the measurement and the lack of a complete calibration of the quartz crystal oscillator, the measurement does not confirm the Langevin approximation or properly qualify the calculation of the flux from Equ. 7.10.

7.6 Summary

In order to demonstrate the potential of the ion crystal weighing technique for applications in cold chemical reaction studies and charge exchange experiments, we have observed the charge exchange between two calcium isotopes. Due to the high measurement resolution, single events can be detected from the change in the COM-mode frequency and the results of individual reactions can be precisely identified. Depending on the reaction rate and the type of reaction being studied, this method can be used to measure 1 a.m.u. changes in the crystal composition for an ion number of up to a few hundred ions, limited by the magnitude of the trap secular frequency.

Finally, we have shown how the ion crystal weighing technique can be used to measure the time evolution of the population ratio of ions in a two-species ion crystal in a context where single event resolution is not available. We have measured the charge exchange cross section for the $^{44}\mathrm{Ca}^+ + {}^{40}\mathrm{Ca} \rightarrow {}^{40}\mathrm{Ca}^+ + {}^{44}\mathrm{Ca}$ reaction and described a technique where a flux can be directly measured using a quartz crystal oscillator. The experiment should be repeated with a proper calibration. This would involve the construction of a calcium source that can deposit significantly more than 100 ng onto the surface of the crystal oscillator. In the measurements described here, the crystal oscillator frequency was linearly dependent on the deposition layer. However, it is uncertain if this linear relationship will continue for the large frequency shifts expected to result from deposition layers significantly larger than 100 ng.

Measurements of the flux of neutral atoms/molecules are inherently challenging, and they typically cause the majority of the uncertainty in ion-neutral collision cross section experiments. With an accurate calibration, we have shown that quartz crystal oscillators can be a valuable tool for measuring flux in neutral atomic and molecular beam experiments.

Chapter 8

All-optical broadband excitation of trapped ions

8.1 Introduction

Alternatively to the electronic excitation discussed in the previous two chapters, the COM-mode frequency of trapped ions can be excited optically using the Doppler cooling laser. The optical excitation of the secular motion of trapped ions is an invaluable tool in modern quantum information processing [88, 113, 90], high resolution spectroscopy [7] and quantum optics [114]. Precisely tailored laser pulses are employed to transfer the state of one ion to another [115], entangle several ions [89, 116], investigate the behavior of coupled systems [117] and generate coherent phonon fields [67]. Employing laser pulses on the motional sidebands, several quantum gates have been demonstrated [95] and ions have been entangled though their joint motion in the trapping potential [118]. Laser induced dipole forces have been utilised to excite the coherent motion of ions which in turn has been exploited to demonstrate quantum phase gates and entangle multiple ions [48, 119]. Recently, the laser induced coupling between the internal and external degrees of freedom of trapped ions has been applied to high resolution spectroscopy of ions which are not suitable for electron shelving [49].

In all these applications, precise control and measurement of the ion's secular motion is required. Several schemes based on the electric excitation of the ion's motion have been developed to precisely measure the secular frequency [42, 97, 120, 46]. In addition, the ion's secular motion can be excited and measured using narrowband excitation through the modulation of the interaction laser intensity [45]. In this chapter we describe a novel

scheme to optically excite and control the amplitude of the ion's secular motion through broadband excitation. Employing a fast change in radiation pressure, an oscillation of the trapped ion around the new, shifted equilibrium position is induced which in turn is amplified by blue detuning the interaction laser. Subsequently, the ion's oscillation is measured through Doppler velocimetry [41, 43, 44]. The scheme is fast and does not require stringent control of the laser parameters. Furthermore, since a coherent excitation of the ion's motion is not required, the method is well suited for situations in which the secular frequency is unknown or rapidly changing.

In the first section of this chapter, the principle of the measurement scheme is discussed. This is followed by a description of the experimental methodology and set-up. Measurements, which have been performed to demonstrate and characterise the optical excitation and amplification of the ion using intensity switching excitation, are presented. A molecular dynamics simulation, which takes into account all of the relevant parameters of the system, is used to generate fitting curves for the experimental data. Finally, the application of frequency switching excitation to precision measurement of the ion's time varying secular frequency is discussed.

8.2 Measurement principle

Our technique is based on a rapid change in the magnitude of the laser induced radiation pressure on the ion. Starting with the laser cooled ion in equilibrium, a fast change in the laser intensity, or detuning, associated with a change in the ion's fluorescence rate results in an axial displacement of the ion in the trapping potential due to the altered radiation pressure. Consequently, the ion oscillates at its COM-mode frequency around the new equilibrium position. To detect the ion's oscillation, Doppler velocimetry is utilised and the ion's oscillatory motion is mapped onto its fluorescence. Doppler velocimetry has been described in Sec. 2.2.6. After the rapid change in radiation pressure, the initial oscillation of the ion is amplified by blue detuning the cooling laser [51, 67]. The oscillation amplitude increases exponentially with time according to Equ. 2.63 and the fluorescence modulation amplitude as a function of time during amplification is given by Equ. 2.64. By collecting the ion's fluorescence during amplification the ion's oscillation amplitude can be measured.

Following amplification, the interaction with a red detuned laser results in a damping of the coherent oscillation accompanied by a cooling of the ion's thermal motion. Consequently, the coherent motion ceases and the ion's kinetic energy approaches the Doppler cooling limit.

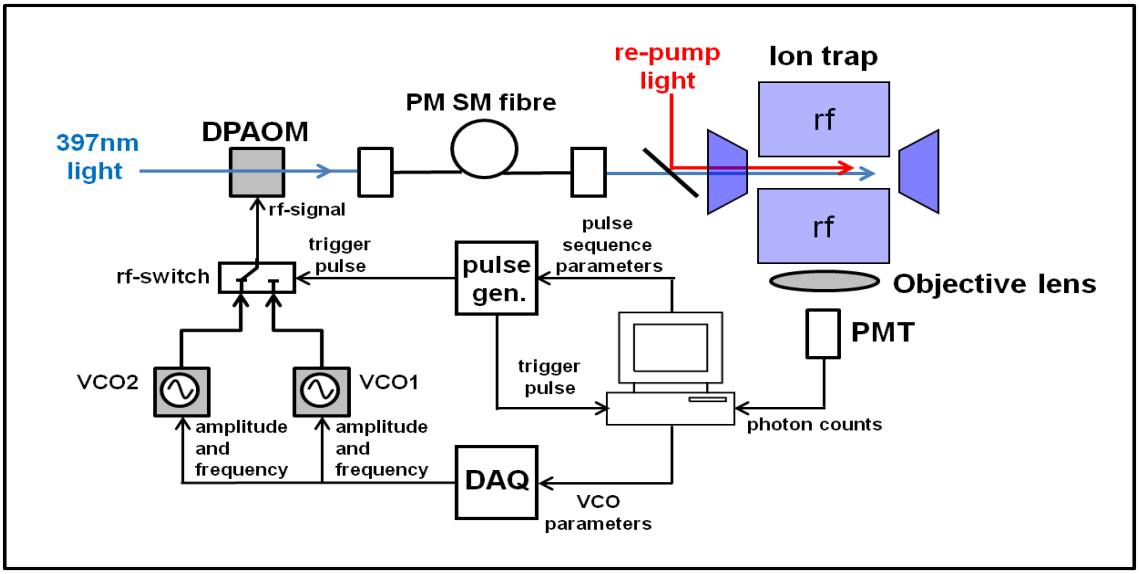

Figure 8.1: Schematic of the experimental set-up. The 397 nm light is coupled through a double-pass AOM (DPAOM) set-up before it is sent to the ion trap through a single-mode (SM) polarisation maintaining (PM) optical fibre. The rf-signal is supplied to the AOM by either of two VCOs connected through an rf-switch. Switching between the two VCOs is determined by a pulse generator. The ion's fluorescence is collected with a PMT and correlated with the trigger pulse from the pulse generator.

In order to measure the ion's time dependant fluorescence rate (fluorescence profile), the photon detection times are continuously recorded and correlated with the excitation pulse. To analyse the measurements, we fit the results of a molecular dynamics simulation to the experimentally obtained fluorescence profile. From the fit we can determine the oscillation amplitude of the ion and the induced heating.

8.3 Experimental set-up

The ^{40}Ca-ion is Doppler-cooled by two laser beams, one aligned radially and one aligned along the trap axis. Consequently, all directions of the ion's motion are cooled. The powers of the two cooling lasers are adjusted such that the majority of fluorescence is due to the ion's interaction with the axial laser. The ion is re-pumped using the 850 nm and 854 nm lasers.

Fig. 8.1 shows a schematic of the experimental set-up. Since the cooling and re-pump laser beams are individually controlled by AOMs in double pass configuration, the set-up allows for precise experimental control of the frequency as well as the intensity of each laser beam. As discussed in Chapter 5, the axial cooling laser AOM is controlled by either of two computer controlled VCOs which are connected to the AOM through an rf-switch.

Additionally, a computer controlled pulse generator determines the timing sequences for switching the laser intensity and for switching between the two VCOs via the rf-switch. In this way, the frequency and intensity of the 397 nm laser may be rapidly shifted to pre-selected values whenever required. During a measurement, the photon detection times are recorded with a TDC[1] and correlated with a trigger pulse occurring at the beginning of each measurement sequence. After the chosen measurement duration, the photon counts are binned according to arrival time and the counts for all measurement sequences are summed. A fitting curve is generated from the molecular dynamics simulation and the ion's peak oscillation amplitude and induced temperature increase are determined. The motional spectrum of the ion is obtained by taking the FFT of the fluorescence profile allowing the COM-mode frequency to be measured with high precision.

8.4 Laser intensity switching

The experimental sequence we employ begins with red detuned lasers for Doppler cooling the ion. This prepares the ion in a motional state close to the Doppler cooling limit. After this initial cooling period, the ion's equilibrium position in the trapping potential is shifted by a change in the laser induced radiation pressure. When the laser is switched off to impart the motional excitation, the ion undergoes undamped oscillations at the axial secular frequency. Subsequently applying a blue detuned laser, the ion's motion is coherently amplified. Then, switching the laser back to red detuning damps the ion's motion. This sequence is repeated at a rate of 1 kHz. To obtain a fluorescence profile during the measurement, a histogram of the photon arrival times with respect to each trigger pulse is generated. The photon arrival times for each sequence are summed to form a total fluorescence profile.

A typical fluorescence profile for a measurement time of ten seconds is shown in Fig. 8.2. In the initial 355 μs, the laser is red detuned to cool the ion's motion. This is followed by a 35 μs interruption in the laser intensity giving a drop in the ion's fluorescence signal and a corresponding change in the laser induced radiation pressure. The ion's oscillation, resulting from the sudden shift in equilibrium position, is then amplified by switching the laser on with blue detuning. The increase in the amplitude of coherent oscillatory motion due to the interaction with the blue detuned laser is clearly visible. In addition, a decrease in the mean signal level is observed. The change in the mean signal level is a measure of the increased linewidth of the heated ion's fluorescence spectrum and therefore an indicator

[1] FastComtec P7888

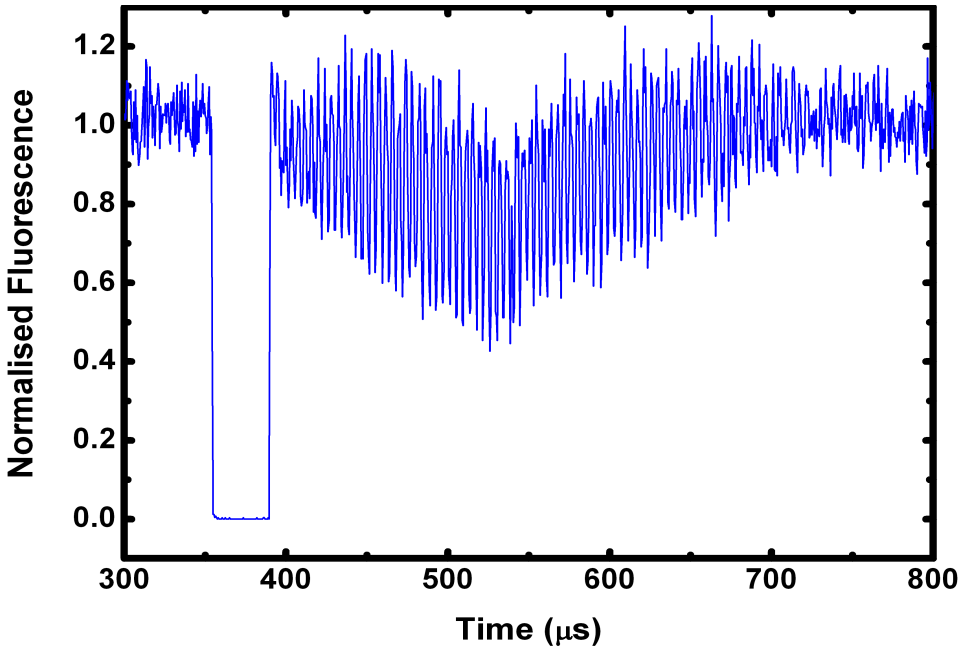

Figure 8.2: Fluorescence profile produced using the laser intensity switching technique as a function of time elapsed since the experimental trigger. The laser detuning is +10 MHz during amplification and -10 MHz during re-cooling. The laser intensity is $2I_{sat}$.

of the measurement induced temperature increase (see Sec. 8.4.2). After an amplification time of 150 μs, the laser is red detuned in order to re-cool the ion. This results in a damping of the coherent motion which ceases after a further 150 μs. In addition, the mean signal level and the temperature of the ion return to their equilibrium values during the re-cooling period.

8.4.1 Molecular dynamics simulation

We can reproduce the behavior of this system well with a molecular dynamics simulation which we have developed[2]. The simulation takes into account all of the relevant parameters of the system. For each step in the simulation, the ion's interaction with the laser is used to determine the steady state population of the excited state in the two-level approximation. The probability of photon absorption and subsequent spontaneous emission is calculated from this, and used to determine the time between spontaneous emission events. The momentum imparted to the ion by absorption and spontaneous emission is used to calculate and update its position and velocity. Finally, photons emitted by the ion are counted to form a fluorescence profile. The laser pulse sequence is chosen to match the experiment with corresponding excitation, amplification and re-cooling timing. Fig. 8.3

[2]The molecular dynamics simulation was developed by Dr. Nicolas Seymour-Smith

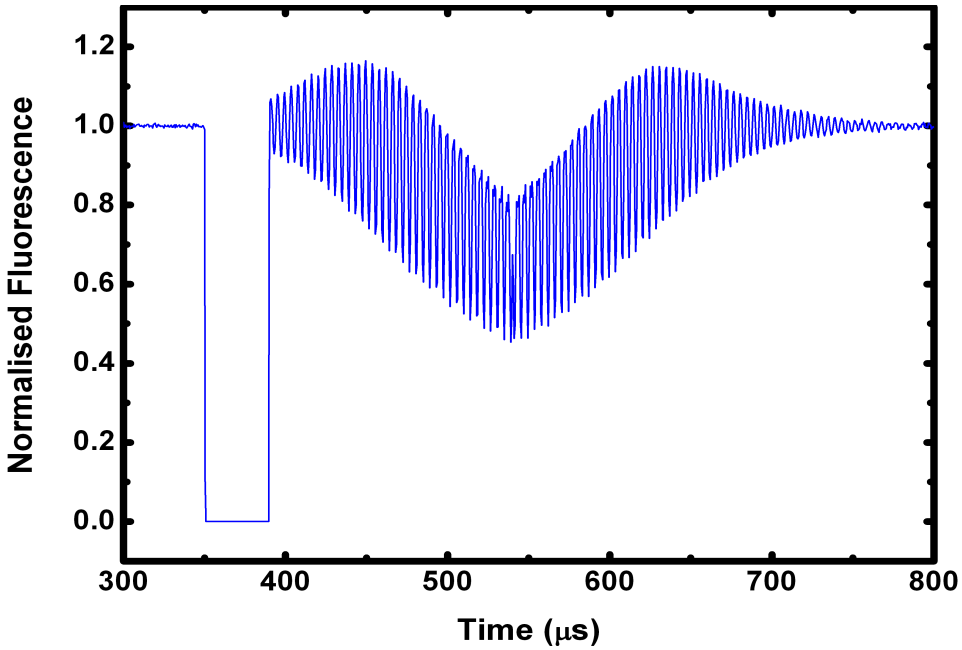

Figure 8.3: Numerical simulation of the experimentally measured fluorescence profile shown in Fig. 8.2 using the same parameters as those used in the experiment.

shows the fluorescence profile produced by the simulation for the same parameters used to produce the experimental data in Fig. 8.2. The agreement between the fluorescence profile created by the simulation and the experimental result is very good.

8.4.2 Amplification time

Fig. 8.4 shows the ion oscillation amplitude as a function of the duration of laser amplification. For each amplification time, a simulated fluorescence profile is fit to the experimental data. The oscillation amplitude is then determined from the simulation using the best fit parameters. For small amplification times, the relationship between the ion oscillation amplitude and the amplification time is approximately exponential, as described by Equ. 2.63. However, for longer amplification times the relationship becomes nearly linear. This is due to the heating of the ion and associated broadening of the ion's spectral line. The increased linewidth of the heated ion decreases the slope of the spectral lineshape and in turn decreases the amplification efficiency.

From the measured fluorescence profile it is possible to unambiguously distinguish between the ion's thermal motion and its coherent oscillatory motion. During amplification of the ion's motion, Doppler broadening leads to an increase in the inhomogeneous component of the ion's spectral line. For an ion with a temperature of T, the inhomogeneous

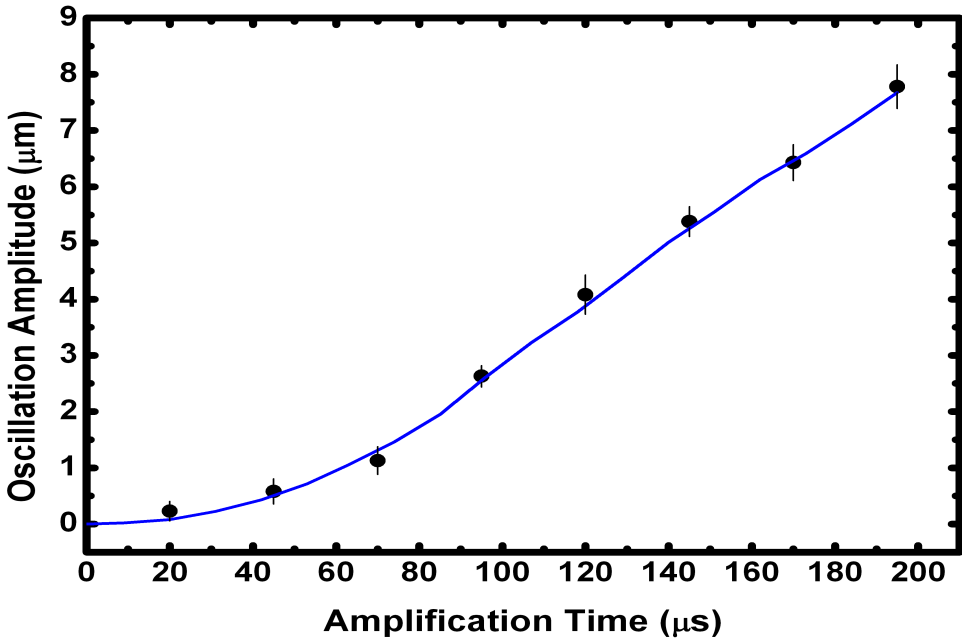

Figure 8.4: The ion's oscillation amplitude as a function of the amplification time. For each measurement The laser detuning is +10 MHz during amplification and -10 MHz during re-cooling. The laser intensity is $2I_{sat}$. A molecular dynamics simulation has been fit to the data (solid line). The relationship is initially exponential but becomes approximately linear for larger amplification times.

linewidth contribution is given by

$$\sigma = \frac{2\pi}{\lambda}\sqrt{\frac{k_B T}{m}}. \tag{8.1}$$

The heated ion's fluorescence spectrum can be described by a Voigt profile. For a fixed laser detuning and small amplitude oscillation, the discrepancy between the mean fluorescence level at the start of amplification and at the end is caused by the increased inhomogeneous contribution to the ion's linewidth. For small blue detuning, the increasing linewidth results in a decreasing mean fluorescence level, as is demonstrated in Fig. 8.2. However, for large blue detuning, the increasing linewidth will result in an increase in the fluorescence level (see, for example, the slight increase in mean signal level during the amplification in Fig. 8.9).

We measure the fluorescence spectrum of the Doppler cooled ion prior to each measurement in order to determine the homogeneous linewidth. The fluorescence spectrum of the cooled ion is a Lorentzian function and the ion's temperature is estimated to be on the order of the Doppler cooling limit. From the change in mean signal level following amplification we can then determine the measurement induced inhomogeneous contribution to the total linewidth. The increase in the ion temperature relative to its initial state is then calculated from the inverted Equ. 8.1 [86, 85].

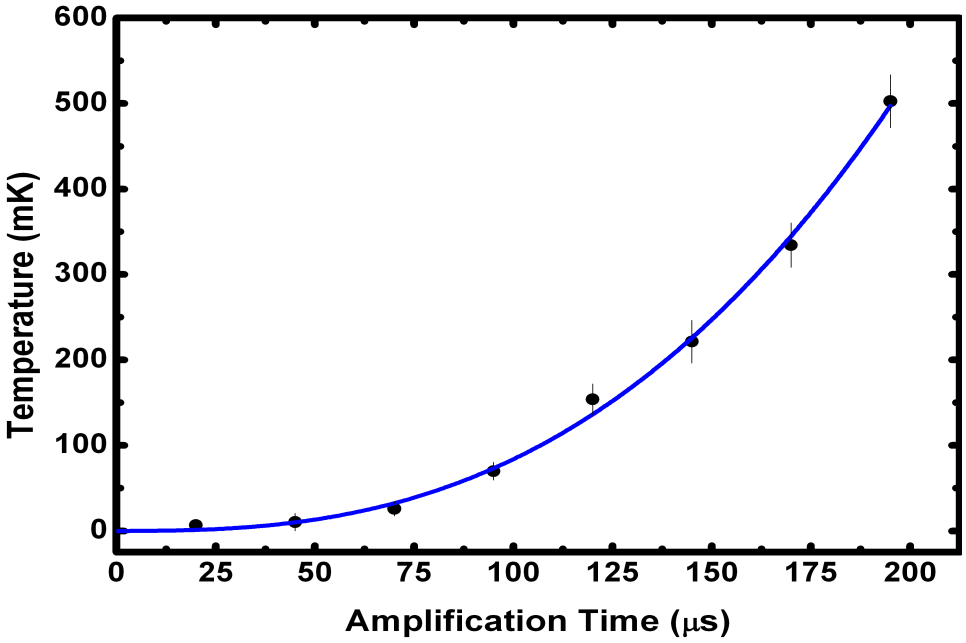

Figure 8.5: The measurement induced temperature increase of the ion as a function of the amplification time. Each data point corresponds to a point in Fig. 8.4. The expected quadratic function has been fit to the data.

The ion temperature at the end of amplification as a function of the amplification time is shown in Fig. 8.5. The relationship is approximately quadratic which reflects the approximately linear change in linewidth for increasing amplification time and the quadratic relationship between linewidth and temperature given by Equ. 8.1. For amplification times beyond around 100 μs the measurement induced temperature increase exceeds 100 mK, which is on the order of the temperature required to form ion Coulomb crystals [103]. For amplification times below 50 μs the measurement induced temperature increase remains below 10 mK which is low enough to allow for the stable trapping of large three-dimensional Coulomb crystals.

8.4.3 Laser intensity

The laser intensity determines the excited state population of the ion, the width of the spectral line and the magnitude of the optical excitation. At low laser intensities, the ion's oscillation amplitude increases linearly with the magnitude of the change in the fluorescence rate ΔR resulting from excitation (see Equ. 2.64). As the intensity is increased further, saturation occurs resulting in a saturation of the fluorescence modulation signal and thus a decrease of the amplification gain.

We have measured the dependence of the ion's oscillation amplitude on the laser intensity while keeping all other parameters constant. In order to determine the amplitude of

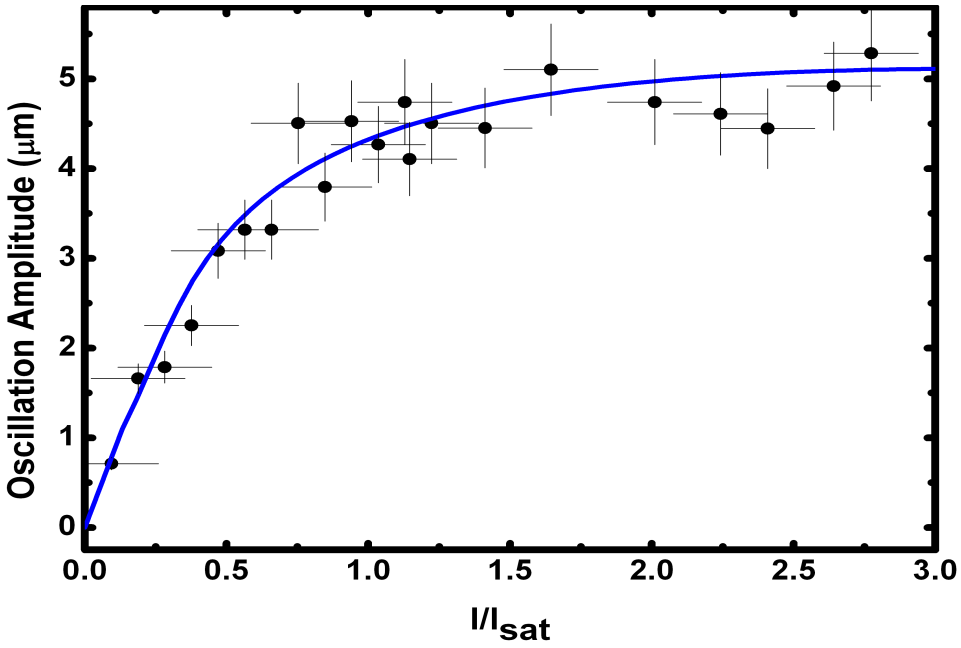

Figure 8.6: The ion's oscillation amplitude as a function of the laser intensity in units of the saturation intensity. For each measurement the laser detuning is +10 MHz during amplification and -10 MHz during re-cooling. The amplification time is 150 μs. A molecular dynamics simulation has been fit to the data (solid line).

the coherent motion, the ion's motional spectrum has been employed. The motional spectrum amplitude is measured by taking the FFT of the fluorescence profile. The oscillation amplitude is determined by fitting a simulated fluorescence profile to one experimental data point. A calibration coefficient relating the amplitude of the motional spectrum to the oscillation amplitude is then determined. A fitting curve for the experimentally measured motional spectrum amplitude as a function of the laser intensity is generated by the molecular dynamics simulation and the result is converted into units of oscillation amplitude using the calibration coefficient. The results are shown in Fig. 8.6.

8.4.4 Laser detuning

We have measured the ion's oscillation amplitude as a function of the laser detuning. The laser blue and red detuning are equal with respect to the center of the spectral line for each of the measurements. This ensures that a difference in laser detuning does not contribute to the optical excitation amplitude. The results are shown in Fig. 8.7. A curve generated by the molecular dynamics simulation has been fit to the data.

The effect of the laser detuning on the fluorescence modulation signal is partly determined by the slope of the ion's spectral line. The most efficient amplification of the ion's

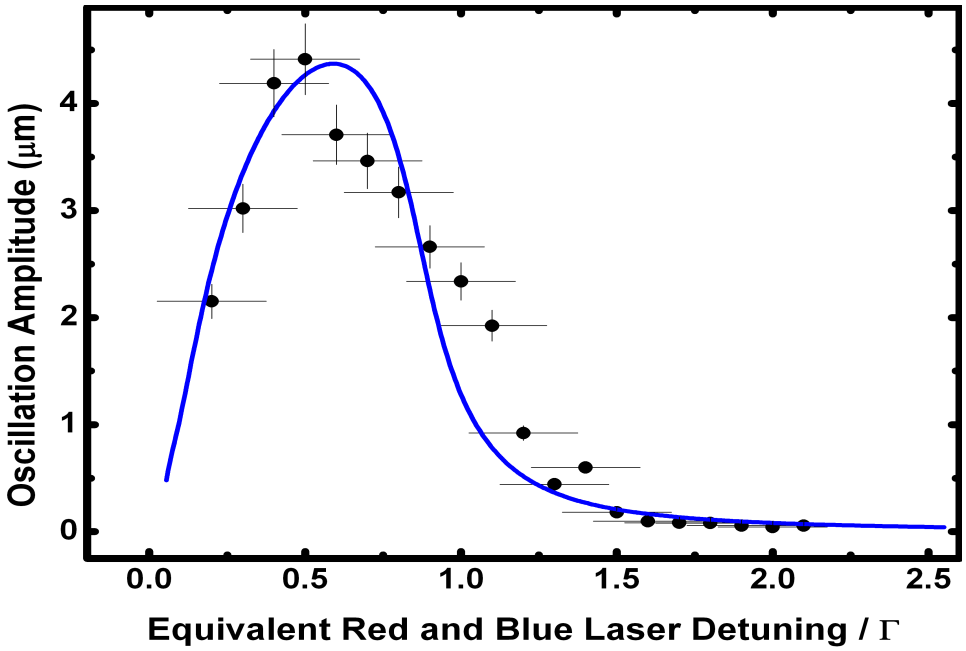

Figure 8.7: The ion's oscillation amplitude as a function of the laser detuning in units of the natural linewidth Γ. The x-axis is the equivalent blue and red laser detuning used during amplification and re-cooling respectively. For each measurement the laser intensity is $2I_{sat}$ and the amplification time is 150 μs. A molecular dynamics simulation has been fit to the data (solid line).

oscillatory motion is achieved for the laser tuning corresponding to the point of steepest slope. For detunings closer to the spectral line centre the amplification decreases due to the decrease in the gradient. However, at the same time, the increase in total fluorescence, and corresponding increase in radiation pressure, for smaller laser detuning results in a shift of the optimum detuning towards the line center.

8.4.5 Laser off-time

When the interaction laser is switched off, the ion behaves as an undamped harmonic oscillator with oscillation amplitude determined by its displacement from the equilibrium position in the trap potential. For laser off-times equal to $n \cdot T$, where T is the period of the ion's oscillation and n is an integer, the ion's motion is exactly out-of-phase with the force from the laser switching back on. In this case, when the laser is reintroduced the ion will be located in the equilibrium position of the combined ion trap and light pressure potential, therefore the ion's oscillatory motion will cease. If, however, the laser off-time is equal to $(\mathrm{n}+\frac{1}{2}) \cdot T$, the ion's motion will be in-phase with the laser and the momentum imparted through the optical excitation will enhance the coherent motion of the ion. We have measured this effect by varying the laser off-time while keeping all other parameters

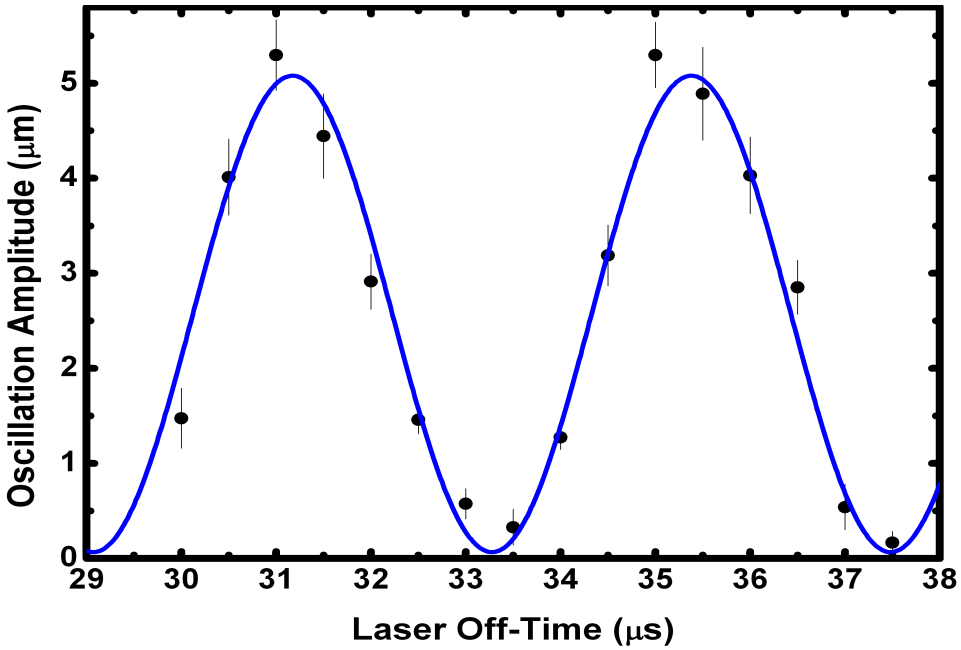

Figure 8.8: The ion's oscillation amplitude as a function of the laser off-time. For each measurement the laser detuning is +10 MHz during amplification and -10 MHz during re-cooling. The laser intensity is $2I_{sat}$ and the amplification time is 150 μs. A sine-squared function has been fit to the data.

fixed. The result is shown in Fig. 8.8 where the ion's oscillation amplitude is plotted as a function of the laser off-time. The expected sine-squared function has been fit to the data. Each data point is the mean of three measurements. The error bars are the standard deviation of each data set. Each measurement is 10 s in duration at a pulse repetition rate of 1 kHz.

8.5 Laser frequency switching

The dependance of the excitation amplitude on the switching time can be avoided through excitation by laser frequency switching while keeping the laser intensity constant. An optical kick can be imparted to the ion by switching between two laser detunings provided that there is a difference in the magnitude of the radiation pressure. When the laser is rapidly shifted from red to blue detuning, the ion's equilibrium position in the trapping potential is shifted and the resulting oscillatory motion is coherently amplified through interaction with the laser. The phase of the ion's motion at the switching time becomes negligible since the amplified oscillation is large compared to the oscillation induced by the light pressure shift. Thus, restrictions on the timing of the laser sequence are removed.

The excitation in this scheme can be modeled by a step function where the excitation amplitude is proportional to the inverse secular frequency. This technique is particularly

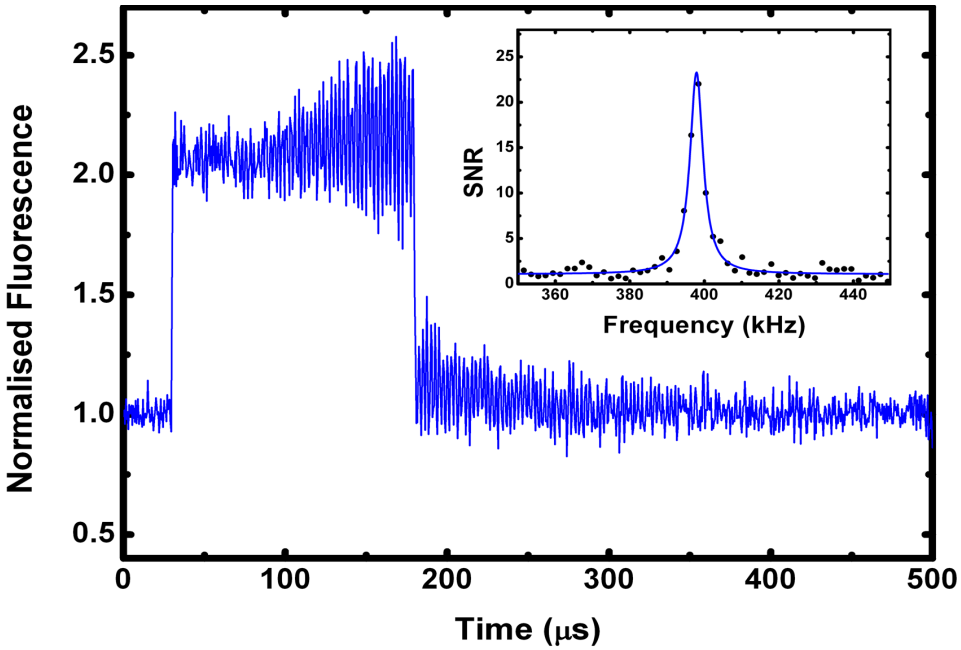

Figure 8.9: Fluorescence as a function of time elapsed since the experimental trigger produced using the laser frequency switching technique. The inset shows the FFT of the fluorescence profile with high contrast resonance peak at the COM-mode frequency. A Lorentzian function has been fit to the data.

suited for situations where the secular frequency is unknown or the frequency is expected to experience large changes during the course of an experiment. However, due to the relatively large difference between red and blue detunings necessary for supplying the optical excitation, the overall fluorescence signal level may be lower than for the laser intensity switching procedure described in Sec. 8.4.

Fig. 8.9 shows a fluorescence profile for a laser sequence where the optical excitation is delivered through a shift in the laser detuning. The laser is initially red detuned for 30 μs to cool the ion's motion. The laser frequency is then suddenly shifted to small blue detuning ($\delta = +10$ MHz) with respect to the red detuning ($\delta = -40$ MHz) and the ion's oscillatory motion is amplified for 150 μs. The difference in radiation pressure between the red and blue detunings determines the magnitude of the excitation ΔR (see Equ. 2.64). Following amplification, the laser is once again red detuned leading to damping of the ion's motion and restoring its temperature to the equilibrium value. This sequence is repeated at a rate of 1 kHz. The inset shows the ion's motional spectrum obtained by taking the FFT of the fluorescence profile. The motional spectrum contains a high contrast peak centered at the COM-mode frequency.

We have measured the ion's oscillation amplitude for the entire range of available axial confinements while keeping the frequency switching parameters constant. The result is

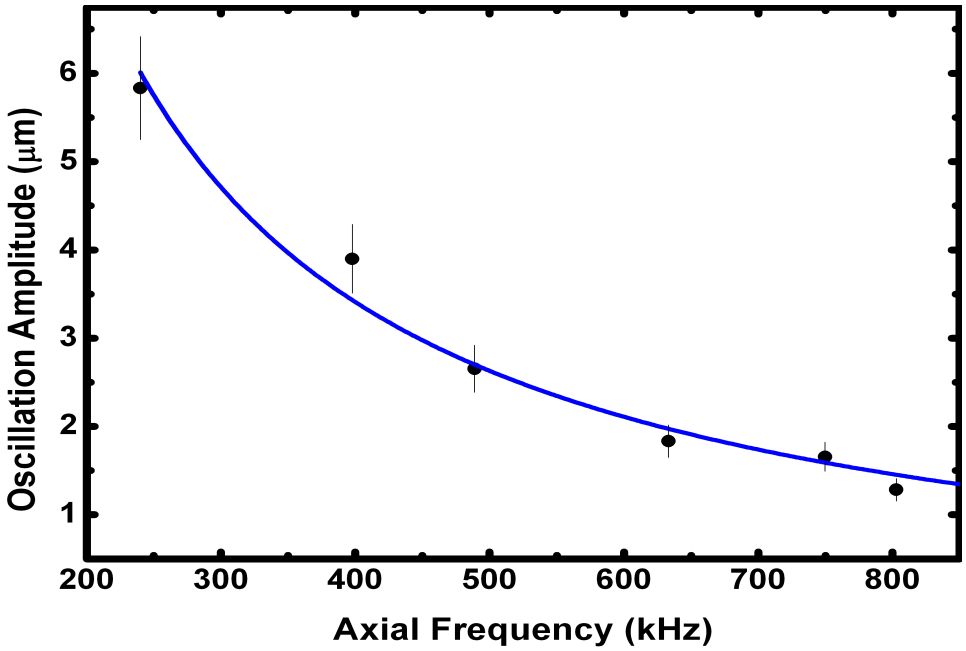

Figure 8.10: The ion's oscillation amplitude as a function of the axial confinement. For each measurement the laser detuning is +10 MHz during amplification and -40 MHz during re-cooling. The laser intensity is I_{sat} and the amplification time is 100 μs. The x-error bars are smaller than the data points. The expected reciprocal function has been fit to the data.

shown in Fig. 8.10 and the expected reciprocal function has been fit to the data with good agreement.

8.6 Summary

In this chapter we have demonstrated and characterised a novel technique for the optical broadband excitation of the secular motion of trapped ions. Employing a blue detuned laser, small light pressure forces are coherently amplified until the ion achieves the desired amplitude of oscillatory motion. We have used a molecular dynamics simulation to model the system and characterize its parameters. We have determined the measurement induced temperature increase of the ion as a function of the laser amplification and demonstrated that it can be kept below 10 mK making the scheme well-suited for the interrogation of large three-dimensional ion crystals.

This technique is a valuable tool for experimental applications where an electronic excitation of the secular motion is undesirable or inconvenient. High precision frequency measurements can be achieved within interrogation times on the order of seconds where the only requirement is laser line-of-sight. In addition, since the excitation has a reciprocal

dependence on the secular frequency, the ion's COM-mode motion can be excited and amplified over a broad range of confinement potentials.

Chapter 9

Conclusion

9.1 Summary

Throughout this thesis experimental techniques which can be applied to reaction studies between ionic and neutral atoms/molecules and high resolution molecular spectroscopy experiments have been presented.

A novel ion trap loading technique using pulsed laser ablation was discussed in Chapter 3. We showed that ground state calcium atoms are produced when the ablation laser fluence is kept below 315(16) mJ/cm^2. Each laser pulse produces a flux of ground state atoms with a thermal energy distribution on the order of hundreds of meV, allowing the application of the loading scheme in macroscopic ion traps with typical trap depths on the order of eV. Since the atoms are produced in the ground state, they may be loaded isotope selectively using the photo-ionisation technique. The ablation laser is operated with a repetition rate on the order of tens of kHz, therefore, the ion trap may be loaded at a precisely controlled high rate. High repetition rate ion trap loading can be applied to experiments requiring rapid turn-around times. Furthermore, the cleanliness of the loading technique is ideally suited for ion traps that incorporate optical cavities. Several novel experiments have been proposed for cooling and probing trapped molecular ions that are coupled to high finesse optical cavities [121].

Chapter 5 described a technique for collecting the entire fluorescence spectrum of trapped ions rapidly and with high precision while maintaining a low ion temperature and good ion localisation throughout interrogation. Measurements of the ion's transition lineshape allow for the precise determination of the central frequency of the spectral line as well as the Lorentzian and Gaussian contributions to the lineshape. We have used the technique to measure the saturation intensity of the calcium ion $4S_{1/2} \rightarrow 4P_{1/2}$ transition and

the results were compared with the theoretical description of the Doppler cooling scheme developed in chapter 2. The spectroscopy technique we have developed is a powerful complement to the experimental methods presented in chapters 6 and 8. By rapidly collecting fluorescence spectra, the relative detuning of the Doppler cooling lasers as well as the slope of the fluorescence spectrum can be determined. This allows the optimal parameters for Doppler velocimetry and optical amplification to be selected.

Chapter 6 described a novel technique for measuring the COM-mode frequency of single trapped ions and large ion crystals. We employed the Fourier transform of the auto-correlation of the ions' fluorescence intensity while exciting their motion by a pulsed electric field. The measurement scheme provides a measurement resolution of better than 100 Hz with an interrogation time on the order of seconds. The increase in the ion's average temperature during interrogation was shown to be less than 3 mK for single ions and around 60 mK for large three-dimensional ion crystals. We demonstrated the precision and non-invasive nature of the technique by measuring the COM-mode frequency shift as a function of the location of a molecular ion in a five-ion string. As described in the introduction, a diverse range of cold collision reaction experiments and high resolution spectroscopy experiments with ion crystals rely upon the ability to precisely measure small changes in the crystal composition following reactions or dissociations. The technique we present is unique in the fact that it provides an accurate and fast real-time secular frequency measurement without the need for modifications to the standard laser cooling scheme. In effect, only the fluorescence collected during Doppler cooling is analysed. Owing to its non-invasive nature, it can be employed in many novel applications.

The ion crystal weighing technique introduced in chapter 6 was used to measure charge exchange reactions between trapped calcium ions and neutral calcium atoms. This was demonstrated by continuously measuring the COM-mode frequency of a small ion crystal containing seven Doppler cooled ^{40}Ca-ions and seven sympathetically cooled ^{44}Ca-ions exposed to a beam of naturally abundant neutral calcium atoms. Despite the fact that the change in total mass of the ion crystal was less than 4% for each charge exchange reaction, large (greater than 1 kHz) steps in the COM-mode frequency of the crystal were observed. We were able to determine the change in mass of the crystal following each reaction with a measurement precision better than 1 a.m.u. We showed that by increasing the secular frequency the experiment can be scaled to accommodate large ion crystals containing several hundred ions. For a secular frequency of 1 MHz, a 1 a.m.u. change in the total mass of the crystal following a reaction can be unambiguously detected for crystals containing up to 250 ions. In addition, we measured the time evolution of the population

ratio of ions in a two-species ion crystal in a context where single event resolution is not available. We measured the charge exchange cross section for the $^{44}Ca^{+} + {}^{40}Ca \rightarrow {}^{40}Ca^{+} + {}^{44}Ca$ reaction. We also described a technique where the atomic flux can be directly measured using a quartz crystal oscillator. We determine the cross section to be greater than $6(3) \times 10^{-14}$ cm^2, which is in agreement with the Langevin approximation. The error on the experimentally measured value comes from the lack of a complete calibration of the quartz crystal oscillator.

Finally, chapter 8 described an all-optical technique for exciting and amplifying the secular motion of trapped ions. The technique is based on a rapid change in the magnitude of the laser induced radiation pressure on the ion. Starting with the laser cooled ion in equilibrium, a fast change in the laser intensity, or detuning, results in an axial displacement of the ion in the trapping potential due to the altered radiation pressure. Consequently, the ion oscillates at its COM-mode frequency around the new equilibrium position. After the rapid change in radiation pressure, the initial oscillation of the ion is amplified by blue detuning the cooling laser. Doppler velocimetry is then used to re-cool the ion and measure the amplitude of its oscillatory motion. We have measured the temperature increase of the ion as a function of the laser amplification and demonstrated that it can be kept below 10 mK making the scheme well-suited for the interrogation of large three-dimensional ion crystals. We have shown that a broadband excitation of the ion is achieved if a rapid change in laser detuning is used to excite the ion. In this case, the excitation is inversely proportional to the ion's secular frequency and a broad range of frequencies can be measured for a fixed set of excitation parameters. The scheme is applicable to experiments were the secular frequency of the ion crystal is unknown or experiencing large changes throughout the course of the experiment. In addition, the technique can be used in an experimental set-up where electronic excitation is not available or desirable.

9.2 Outlook

The automation and repeatability of measurement processes are important aspects of cold chemistry and molecular spectroscopy experiments. Each of the experimental techniques described in this thesis is modular and can be combined to form compound experimental routines. The atomic and/or molecular ions can be loaded into the trap by combining the pulsed laser ablation technique with resonant photo-ionisation. After the initial preparation of the ion crystal, the fluorescence spectrum can be collected and the optimum laser parameters for Doppler velocimetry and/or laser amplification applied. The composition

of the crystal, including the number and species of the sympathetically cooled molecular ions it contains, can then be determined rapidly and with high precision using either the ion crystal weighing technique or the optical excitation technique. The time evolution of the molecular ion populations within the crystal can then be monitored using either of the two methods for precisely measuring the crystal's COM-mode frequency. Throughout this thesis we have shown that all of these measurements can be performed rapidly and with high precision without compromising the structure of the ion crystal.

The optical amplification technique discussed in chapter 8 has a further potential application in the non-destructive molecular ion state detection scheme described by Koelemeij et al. [52]. The scheme relies upon the detection of small amplitude oscillations induced by an optical dipole force that is dependent on the state of one or more molecular ions that are sympathetically cooled by one or more laser cooled atomic ions. The dipole force is modulated so that it drives a normal mode of the ion string provided that the molecular ion(s) occupies the state being probed. The increase in motional quanta can then be detected by probing the laser cooled atomic ion(s). It has been proposed that sideband spectroscopy of the atomic ion can be used to measure the motional quanta acquired as a result of the driving dipole force [49, 51]. However, this requires a narrow linewidth laser. It may also be possible to amplify the small amplitude oscillation that has been seeded by the state dependant dipole force and detect the resulting relatively large amplitude oscillation with Doppler velocimetry. The advantage of this scheme is the simplicity of the experimental set-up. As with the ion crystal weighing technique, only the standard Doppler cooling lasers are required. For amplification and Doppler velocimetry, the only requirement is a laser line-of-sight.

We plan to implement a non-destructive state detection scheme using a two-ion string consisting of a sympathetically cooled N_2^+ and a laser cooled ^{40}Ca-ion. The dipole force on the N_2^+ will be provided by a laser at 785 nm detuned by order GHz from an electronic transition. It is essential that the interaction time between the dipole force laser and the molecular ion is minimised in order to minimise the probability of spontaneous emission and subsequent destruction of the internal state of the molecular ion. We estimate that the laser can interact with the molecular ion for approximately 1 ms giving an acceptably low spontaneous emission probability of approximately 1%. The total force on the ion from the dipole force laser is estimated to be on the order of zN (10^{-21} N). In the current experimental setup, a 1 zN force on the ion results in a displacement of around 200 nm at an axial frequency of 300 kHz. With the current imaging set-up, each pixel on the EMCCD image has a width of about 250 nm. In effect, the displacement caused by the dipole force

will not be detectable using the EMCCD camera. The best chance for detecting this force is by amplifying the small amplitude oscillatory motion resulting from the displacement of the ion using a technique like the one described in chapter 8.

Cold chemistry and high resolution molecular spectroscopy are rapidly expanding interdisciplinary fields of study with many exciting results on the horizon. The experimental techniques presented in this thesis can have an important role to play in many of the forthcoming and fascinating experiments with sympathetically cooled molecular ions.

Bibliography

[1] S. Willitsch. Coulomb-crystallised molecular ions in traps: methods, applications, prospects. *Int. Rev. Phys. Chem.*, 31:175–199, 2012. 1, 93

[2] M.T. Bell and T.P. Softley. Ultracold molecules and ultracold chemistry. *Mol. Phys.*, 107:99–132, 2009. 1, 2, 93

[3] D. Skouteris, D.E. Manolopoulos, W. Bian, L.H. Werner, H.J. Lai, and K. Liu. van der Waals Interactions in the Cl + HD Reaction. *Science*, 286:1713–1716, 1999. 1

[4] N. Balakrishnan. On the role of van der Waals interaction in chemical reactions at low temperatures. *J. Chem. Phys.*, 121:5563, 2004. 1

[5] R.V. Krems. Molecules near absolute zero and external field control of atomic and molecular dynamics. *Int. Rev. Phys. Chem.*, 24:99, 2005. 1

[6] R.V. Krems. Cold controlled chemistry. *Phys. Chem. Chem. Phys.*, 10:4079–4092, 2008. 1

[7] J.C.J. Koelemeij, B. Roth, A. Wicht, I. Ernsting, and S. Schiller. Vibrational Spectroscopy of HD^+ with 2-ppb Accuracy. *Phys. Rev. Lett.*, 98:173002, 2007. 1, 73, 114

[8] U. Bressel, A. Borodin, J. Shen, M. Hansen, I. Ernsting, and S. Schiller. Manipulation of Individual Hyperfine States in Cold Trapped Molecular Ions and Application to HD^+ Frequency Metrology. *Phys. Rev. Lett.*, 108:183003, 2012. 1, 73

[9] B.E. Sauer, J.J. Hudson, M.R. Tarbutt, and E.A. Hinds. Cold molecules as a laboratory for particle physics. *Cool Interactions*, pages 359–369, 2005. 1

[10] D.I. Schuster, L.S. Bishop, I.L. Chuang, D. DeMille, and R.J. Schoelkopf. Cavity QED in a molecular ion trap. *Phys. Rev. A*, 83:012311, 2011. 1

[11] H. Müller, S. Herrmann, A. Saenz, A. Peters, and C. Lämmerzahl. Precision Test of Mass-Ratio Variations with Lattice-Confined Ultracold Molecules. *Phys. Rev. D*, 70:076004, 2004. 1

[12] D. DeMille, S.B. Cahn, D. Murphree, D.A. Rahmlow, and M.G. Kozlov. Using Molecules to Measure Nuclear Spin-Dependent Parity Violation. *Phys. Rev. Lett.*, 100:023003, 2008. 1

[13] S. Schiller and V. Korobov. Tests of time-independence of the electron and nuclear masses with ultracold molecules. *Phys. Rev. A*, 71:032505, 2005. 1

[14] T. Zelevinsky, S. Kotochigova, and J. Ye. Precision Test of Mass-Ratio Variations with Lattice-Confined Ultracold Molecules. *Phys. Rev. Lett.*, 100:043201, 2008. 1

[15] D. DeMille, S. Sainis, J. Sage, T. Bergeman, S. Kotochigova, and E. Tiesinga. Enhanced Sensitivity to Variation of m_e/m_p in Molecular Spectra. *Phys. Rev. Lett.*, 100:043202, 2008. 1

[16] A.E. Leanhardt, J.L. Bohn, H. Loh, P. Maletinsky, E.R. Meyer, L.C. Sinclair, R.P. Stutz, and E.A. Cornell. High-resolution spectroscopy on trapped molecular ions in rotating electric fields: A new approach for measuring the electron electric dipole moment. *J. Mol. Spec.*, 270:1–25, 2011. 1

[17] A. Bertelsen, S. Jørgensen, and M. Drewsen. The rotational temperature of polar molecular ions in Coulomb crystals. *J. Phys. B: At. Mol. Opt. Phys.*, 39:L83, 2006. 2

[18] B. Roth, J.C.J. Koelemeij, H. Daerr, and S. Schiller. Rovibrational spectroscopy of trapped molecular hydrogen ions at millikelvin temperatures. *Phys. Rev. A*, 74:040501, 2006. 2, 73

[19] J.C.J. Koelemeij, D.W.E. Noom, D. de Jong, M.A. Haddad, and W. Ubachs. Observation of the $\nu' = 8 \leftarrow \nu' = 0$ vibrational overtone in cold trapped HD^+. *Appl. Phys. B*, 107:1075–1085, 2012. 2

[20] E.S. Shuman, J.F. Barry, and D. DeMille. Laser cooling of a diatomic molecule. *Nature*, 467:820–823, 2010. 2

[21] J.H.V. Nguyen, C.R. Viteri, E.G. Hohenstein, C.D. Sherrill, K.R. Brown, and B. Odom. Challenges of laser-cooling molecular ions. *New J. Phys.*, 13:063023, 2011. 2

[22] M. Zeppenfeld, B.G.U. Englert, R. Glöckner, A. Prehn, M. Mielenz, C. Sommer, L.D. van Buuren, M. Motsch, and G. Rempe. Sisyphus cooling of electrically trapped polyatomic molecules. *Nature*, 491:570–573, 2012. 2

[23] D.J. Wineland, R.E. Drullinger, and F.L. Walls. Radiation-Pressure Cooling of Bound Resonant Absorbers. *Phys. Rev. Lett.*, 40:1639–1642, 1978. 2

[24] W. Neuhauser, M. Hohenstatt, and P. Toschek. Optical-Sideband Cooling of Visible Atom Cloud Confined in Parabolic Well. *Phys. Rev. Lett.*, 41:233–236, 1978. 2

[25] R.E. Drullinger, D.J. Wineland, and J.C. Bergquist. High-Resolution Optical Spectra of Laser Cooled Ions. *Appl. Phys.*, 22:365–368, 1980. 2

[26] D.J. Larson, J.C. Bergquist, J.J. Bollinger, W.M. Itano, and D.J. Wineland. Sympathetic cooling of trapped ions: A laser-cooled two-species nonneutral ion plasma. *Phys. Rev. Lett.*, 57:70–73, 1986. 2

[27] T. Baba and I. Waki. Cooling and mass-analysis of molecules using laser-cooled atoms. *Jpn. J. Appl. Phys.*, 35:1134–1137, 1996. 2, 73

[28] K. Molhave and M. Drewsen. Formation of translationally cold MgH+ and MgD+ molecules in an ion trap. *Phys. Rev. A*, 62:011401(R), 2000. 2

[29] B. Roth, P. Blythe, H. Wenz, H. Daerr, and S. Schiller. Ion-neutral chemical reactions between ultracold localized ions and neutral molecules with single-particle resolution. *Phys. Rev. A*, 73:042712, 2006. 2

[30] M.T. Bell, A.D. Gingell, J.M. Oldham, T.P. Softley, and S. Willitsch. Ion-molecule chemistry at very low temperatures: cold chemical reactions between Coulomb-crystallized ions and velocity-selected neutral molecules. *Faraday Discuss.*, 142:73–91, 2009. 2, 93

[31] X. Tong, A.H. Winney, and S. Willitsch. Sympathetic Cooling of Molecular Ions in Selected Rotational and Vibrational States Produced by Threshold Photoionization. *Phys. Rev. Lett.*, 105:143001, 2010. 2

[32] A. Ostendorf, C.B. Zhang, M.A. Wilson, D. Offenberg, B. Roth, and S. Schiller. Sympathetic Cooling of Complex Molecular Ions to Millikelvin Temperatures. *Phys. Rev. Lett.*, 97:243005, 2006. 2

[33] T. Baba and I. Waki. Chemical reaction of sympathetically laser-cooled molecular ions. *J. Chem. Phys.*, 116:1858, 2002. 2

[34] B. Roth, P. Blythe, H. Daerr, L. Patacchini, and S. Schiller. Production of ultracold diatomic and triatomic molecular ions of spectroscopic and astrophysical interest. *J. Phys. B: At. Mol. Opt. Phys.*, 39:S1241, 2006. 2

[35] A.D. Gingell, M.T. Bell, J.M. Oldham, T.P. Softley, and J.N. Harvey. Cold chemistry with electronically excited Ca^+ Coulomb crystals. *J. Chem. Phys.*, 133:194302, 2010. 2, 94

[36] S. Willitsch, M.T. Bell, A.D. Gingell, S.R. Procter, and T.P. Softley. Cold Reactive Collisions between Laser-Cooled Ions and Velocity-Selected Neutral Molecules. *Phys. Rev. Lett.*, 100:043203, 2008. 2, 94

[37] B. Gao. Universal Properties in Ultracold Ion-Atom Interactions. *Phys. Rev. Lett.*, 104:213201, 2010. 2

[38] X. Tong, T. Nagy, J. Yosa Reyes, M. Germann, M. Meuwly, and S. Willitsch. State-selected ion-molecule reactions with Coulomb-crystallized molecular ions in traps. *Chem. Phys. Lett.*, 547:1–8, 2012. 2

[39] F.H.J. Hall and S. Willitsch. Millikelvin Reactive Collisions between Sympathetically-Cooled Molecular Ions and Laser-Cooled Atoms in an Ion-Atom Hybrid Trap. *Phys. Rev. Lett.*, 109:233202, 2012. 2

[40] C.B. Zhang, D. Offenberg, B. Roth, M.A. Wilson, and S. Schiller. Molecular-dynamics simulations of cold single-species and multispecies ion ensembles in a linear Paul trap. *Phys. Rev. A*, 76:012719, 2007. 2, 93

[41] R. Blümel, C. Kappler, W. Quint, and H. Walther. Chaos and order of laser-cooled ions in a Paul trap. *Phys. Rev. A*, 40:2, 1989. 2, 20, 74, 115

[42] K. Dholakia, G.Zs.K. Horvath, D.M. Segal, R.C. Thompson, D.M. Warrington, and D.C. Wilson. Photon-correlation detection of ion-oscillation frequencies in quadrupole ion traps. *Phys. Rev. A*, 47:1, 1993. 2, 74, 114

[43] D.J. Berkeland, J.D. Miller, J.C. Bergquist, W.M. Itano, and D.J. Wineland. Minimization of ion micromotion in a Paul trap. *J. Appl. Phys.*, 83:10, 1998. 2, 20, 55, 74, 115

[44] M.J. Biercuk, H. Uys, J.W. Britton, A.P. VanDevender, and J.J. Bollinger. Ultrasensitive detection of force and displacement using trapped ions. *Nature Nano.*, 5:646–650, 2010. 2, 20, 74, 115

[45] M. Drewsen, A. Mortensen, R. Martinussen, P. Staanum, and J.L. Sørensen. Nondestructive Identification of Cold and Extremely Localized Single Molecular Ions. *Phys. Rev. Lett.*, 93:243201, 2004. 2, 73, 87, 93, 114

[46] K. Sheridan and M. Keller. Weighing of trapped ion crystals and its applications. *New J. Phys.*, 13:123002, 2011. 2, 93, 114

[47] D.J. Wineland, C. Monroe, W.M. Itano, D. Leibfried, B.E. King, and D.M. Meekhof. Experimental issues in coherent quantum-state manipulation of trapped atomic ions. *J. Res. Natl. Inst. Stand. Tech.*, 103:259, 1998. 3

[48] D. Leibfried, B. DeMarco, V. Meyer, D. Lucas, M. Barrett, J. Britton, W.M. Itano, B. Jelenković, C. Langer, T. Rosenband, and D.J. Wineland. Experimental demonstration of a robust, high-fidelity geometric two ion-qubit phase gate. *Nature*, 422:412–415, 2003. 3, 73, 114

[49] P.O. Schmidt, T. Rosenband, C. Langer, W.M. Itano, J.C. Bergquist, and D.J. Wineland. Spectroscopy using quantum logic. *Science*, 309:749–752, 2005. 3, 114, 131

[50] P.O. Schmidt, T. Rosenband, J.C.J. Koelemeij, D.B. Hume, W.M. Itano, J.C. Berquist, and D.J. Wineland. Spectroscopy of atomic and molecular ions using quantum logic. *AIP Conference Proceedings*, 862:305–312, 2006. 3

[51] D.B. Hume, C.W. Chou, D.R. Leibrandt, M.J. Thorpe, D.J. Wineland, and T. Rosenband. Trapped-Ion State Detection through Coherent Motion. *Phys. Rev. Lett.*, 107:243902, 2011. 3, 21, 115, 131

[52] J.C.J. Koelemeij, B. Roth, and S. Schiller. Blackbody thermometry with cold molecular ions and application to ion-based frequency standards. *Phys. Rev. A*, 76:023413, 2007. 3, 131

[53] K. Sheridan, N. Seymour-Smith, A. Gardner, and M. Keller. All-optical broadband excitation of the motional state of trapped ions. *Eur. Phys. J. D*, 66:289, 2012. 3

[54] Y.-W. Lin, S. Williams, and B.C. Odom. Resonant Few-Photon Excitation of a Single-Ion Oscillator. *Phys. Rev. A*, 87:011402(R), 2013. 3

[55] K. Sheridan, W. Lange, and M. Keller. All-optical ion generation for ion trap loading. *Appl. Phys. B*, 104:755–761, 2011. 3

[56] Pradip K. Ghosh. *Ion Traps.* Oxford Science Publications, 1995. 7

[57] Harold J. Metcalf and Peter van der Straten. *Laser Cooling and Trapping.* Springer, 1999. 11

[58] John Weiner and P.-T. Ho. *Light-Matter Interaction, Vol. 1.* Wiley, 2003. 11

[59] Fam Le Kien and K. Hakuta. *Density Operator and Applications in Nonlinear Optics.* Lecture Notes, University of Electro-Communications, Japan, 2004. 11

[60] D.M. Lucas, A. Ramos, J.P. Home, M.J. McDonnell, S. Nakayama, J.-P. Stacey, S.C. Webster, D.N. Stacey, and A.M. Steane. Isotope-selective photionization for calcium ion trapping. *Phys. Rev. A*, 69:012711, 2004. 11, 26, 97

[61] Mark Alexander Wilson. *Quantum State Control of a Single Trapped Strontium Ion.* PhD Thesis, The University of Strathclyde, 2001. 11

[62] David Szwer. *High Fidelity Readout and Protection of a $^{43}Ca^{+}$ Trapped Ion Qubit.* PhD Thesis, St. Catherine's College Oxford, 2009. 13, 15, 17, 71

[63] G. Janik, W. Nagourney, and H. Dehmelt. Doppler-free optical spectroscopy on the Ba^{+} mono-ion oscillator. *J. Opt. Soc. Am. B*, 2:1251–1257, 1985. 14

[64] R.M. Whitley and C.R. Stroud. Double optical resonance. *Phys. Rev. A*, 14:1498–1513, 1976. 14

[65] R. Gerritsma, G. Kirchmair, F. Zähringer, J. Benhelm, R. Blatt, and C.F. Roos. Precision measurement of the branching fractions of the 4p $^2P_{3/2}$ decay of Ca II. *Eur. Phys. J. D*, 50:13–19, 2008. 17

[66] D.T.C. Allcock, J.A. Sherman, D.N. Stacey, A.H. Burrell, M.J. Curtis, G. Imreh, N.M. Linke, D.J. Szwer, S.C. Webster, A.M. Steane, and D.M. Lucas. Implementation of a symmetric surface-electrode ion trap with field compensation using a modulated Raman effect. *New J. Phys.*, 12:053026, 2010. 15

[67] K. Vahala, M. Herrmann, S. Knünz, V. Batteiger, G. Saathoff, T.W. Hansch, and Th. Udem. A phonon laser. *Nature Physics*, 5:682–686, 2009. 21, 114, 115

[68] R.G. DeVoe and C. Kurtsiefer. Experimental study of anomalous heating and trap instabilities in a microscopic ^{137}Ba ion trap. *Phys. Rev. A*, 65:063407, 2002. 23

[69] N. Daniilidis, S. Narayanan, S.A. Möller, R. Clark, T.E. Lee, P.J. Leek, A. Wallraff, St. Schulz, F. Schmidt-Kaler, and H. Häffner. Fabrication and heating rate study of microscopic surface electrode ion traps. *New J. Phys.*, 13:013032, 2011. 23

[70] D. Kielpinski, C. Monroe, and D.J. Wineland. Architecture for a large-scale ion-trap quantum computer. *Nature*, 417:709–711, 2002. 23

[71] D. Stick, W.K. Hensinger, S. Olmschenk, M.J. Madsen, K. Schwab, and C. Monroe. Ion trap in a semiconductor chip. *Nature Physics*, 2:36–39, 2006. 23

[72] M. Brownnutt, G. Wilpers, R.C. Thompson, and A.G. Sinclair. Monolithic microfabricated ion trap chip design for scalable quantum processors. *New J. Phys.*, 8:232, 2006. 23

[73] M. Keller, B. Lange, K. Hayasaka, W. Lange, and H. Walther. Stable long-term coupling of a single ion to a cavity mode. *J. Mod. Opt.*, 54:1607–1617, 2007. 23

[74] M. Keller, B. Lange, K. Hayasaka, W. Lange, and H. Walther. A calcium ion in a cavity as a controlled single-photon source. *New J. Phys.*, 6:95, 2004. 23

[75] C. Russo and et al. Raman spectroscopy of a single ion coupled to a high-finesse cavity. *Appl. Phys. B*, 95:205–211, 2009. 23

[76] M. Ashfold, F. Claeyssens, G. Fuge, and S. Henley. Pulsed laser ablation and deposition of thin films. *Chem. Soc. Rev.*, 33:23–31, 2004. 24

[77] R.F. Haglund. *Mechanisms of Laser-Induced Desorption and Ablation.* Academic Press, 1998. 24

[78] R.J. Hendricks, D.M. Grant, P.F. Herskind, A. Dante, and M. Drewson. An all-optical ion-loading technique for scalable microtrap architectures. *Appl. Phys. B*, 88:507, 2007. 24, 30, 33

[79] D.R. Leibrandt, R.J. Clark, J. Labaziewicz, P. Antohi, W. Bakr, K.R. Brown, and I.L. Chuang. Laser ablation loading of a surface-electrode ion trap. *Phys. Rev. A*, 76:055403, 2007. 24

[80] N. Kjaergaard, L. Hornekaer, A.M. Thommesen, Z. Videsen, and M. Drewsen. Isotope selective loading of an ion trap using resonance-enhanced two-photon ionization. *Appl. Phys. B*, 71:207–210, 2000. 26

[81] S. Gulde, D. Rotter, P. Barton, F. Schmidt-Kaler, R. Blatt, and W. Hogervorst. Simple and efficient photo-ionization loading of ions for precision ion-trapping experiments. *Appl. Phys. B*, 73:861–863, 2001. 26

[82] Durham Atomic and Molecular Physics Group. *Open Access Experimentalist Resources.* Durham University, Department of Physics, United Kingdom, 2005. 29

[83] N.F. Ramsey. *Molecular Beams.* Oxford Science Publications, 1963. 32, 110

[84] N.B. Pilling. Vapor pressure of metallic calcium. *Phys. Rev.*, 18:362–368, 1921. 32, 33, 110

[85] J.H. Wesenberg, R.J. Epstein, D. Leibfried, R.B. Blakestad, J. Britton, J.P. Home, W.M. Itano, J.D. Jost, E. Knill, C. Langer, R. Ozeri, S. Seidelin, and D.J. Wineland. Fluorescence during Doppler cooling of a single trapped atom. *Phys. Rev. A*, 76:053416, 2007. 59, 120

[86] E. Brama, M. Mortensen, M. Keller, and W. Lange. Heating rates in a thin ion trap for microcavity experiments. *Appl. Phys. B*, 107:945–954, 2012. 59, 120

[87] A.L. Wolf, S.A. van den Berg, C. Gohle, E.J. Salumbides, W. Ubachs, and K.S.E. Eikema. Frequency metrology on the 4s $^2S_{1/2}$→4p $^2P_{1/2}$ transition in $^{40}Ca^+$ for a comparison with quasar data. *Phys. Rev. A*, 78:032511, 2008. 60

[88] A. Barenco, D. Deutsch, R. Jozsa, and A. Ekert. Conditional Quantum Dynamics and Logic Gates. *Phys. Rev. Lett.*, 74:4083–4086, 1995. 73, 114

[89] H. Häffner, W. Hänsel, C.F. Roos, J. Benhelm, D. Chek-al kar, M. Chwalla, T. Körber, U.D. Rapol, M. Riebe, P.O. Schmidt, C. Becher, O. Gühne, W. Dür, and R. Blatt. Scalable multiparticle entangement of trapped ions. *Nature*, 438:643–646, 2005. 73, 114

[90] D. Leibfried, E. Knill, S. Seidelin, J. Britton, R.B. Blakestad, J. Chiaverini, D.B. Hume, W.M. Itano, J.D. Jost, C. Langer, R. Ozeri, Reichle R., and D.J. Wineland. Creation of a six-atom 'Schrödinger cat' state. *Nature*, 438:639–642, 2005. 73, 114

[91] C.F. Roos, M. Chwalla, K. Kim, M. Riebe, and R. Blatt. 'Designer atoms' for quantum metrology. *Nature*, 443:316–319, 2006. 73

[92] T. Rosenband, D.B. Hume, P.O. Schmidt, C.W. Chou, A. Brusch, L. Lorini, W.H. Oskay, R.E. Drullinger, T.M. Fortier, J.E. Stalnaker, S.A. Diddams, W.C. Swann,

N.R. Newbury, W.M. Itano, D.J. Wineland, and J.C. Bergquist. Frequency ratio of Al^+ and Hg^+ single-ion optical clocks; Metrology at the 17th decimal place. *Science*, 319:1808–1812, 2008. 73

[93] H.S. Margolis, G.P. Barwood, G. Huang, H.A. Klein, S.N. Lea, K. Szymaniec, and P. Gill. Hertz-level measurement of the optical clock frequency in a single $^{88}Sr^+$ ion. *Science*, 306:1255–1358, 2004. 73

[94] J. Stenger, Chr. Tamm, N. Haverkamp, S. Weyers, and H.R. Telle. Absolute frequency measurement of the 435.5-nm $^{171}Yb^+$-clock transition with a Kerr-lens mode-locked femtosecond laser. *Opt. Lett.*, 26:1589, 2001. 73

[95] J.J. García, P. Zoller, and J.I. Cirac. Speed Optimized Two-Qubit Gates with Laser Coherent Control Techniques for Ion Trap Quantum Computing. *Phys. Rev. Lett.*, 91:157901, 2003. 73, 114

[96] D. Offenberg, Ch. Wellers, C.B. Zhang, B. Roth, and S. Schiller. Measurement of small photodestruction rates of cold, charged biomolecules in an ion trap. *J. Phys. B: At. Mol. Opt. Phys.*, 42:035101, 2009. 73

[97] M. Welling, H.A. Schuessler, R.I Thompson, and H. Walther. Ion/molecule reactions, mass spectrometry and optical spectroscopy in a linear ion trap. *Int. J. Mass Spec. and Ion Processes*, 172:95–114, 1998. 73, 114

[98] B. Roth and S. Schiller. *Cold Molecules: Theory, Experiment, Applications.* CRC Press, 2009. 73, 93

[99] C. Raab, J. Eschner, J. Bolle, H. Oberst, F. Schmidt-Kaler, and R. Blatt. Motional sidebands and direct measurement of the cooling rate in the resonance flourescence of a single trapped ion. *Phys. Rev. Lett.*, 35:538, 2000. 73

[100] C. Monroe, D.M. Meekhof, B.E. King, S.R. Jefferts, W.M. Itano, P. Gould, and D.J. Wineland. Raman sideband cooling in the presence of multiple decay channels. *Phys. Rev. Lett.*, 75:4011, 1995. 73

[101] F. Diedrich and H. Walther. Nonclassical Radiation of a Single Stored Ion. *Phys. Rev. Lett.*, 53:3, 1987. 74

[102] D. Rotter, M. Mukherjee, F. Dubin, and R. Blatt. Monitoring a single ion's motion by second-order photon correlations. *New J. Phys.*, 10:043011, 2008. 74

[103] L. Hornekaer and M. Drewsen. Formation process of large ion Coulomb crystals in linear Paul traps. *Phys. Rev. A*, 66:013412, 2002. 85, 121

[104] J. Emsley. *The Elements (Oxford Chemistry Guides)*. Oxford University Press, 1995. 87

[105] G. Morigi and H. Walther. Two-species Coulomb chains for quantum information. *Eur. Phys. J. D*, 13:261–269, 2001. 88

[106] R. Côté and A. Dalgarno. Ultracold atom ion collisions. *Phys. Rev. A*, 62:012709, 2000. 94

[107] Z. Idziaszek, T. Calarco, P.S. Julienne, and A. Simoni. Quantum theory of ultracold atom ion collisions. *Phys. Rev. A*, 79:010702, 2009. 94

[108] A.T. Grier, M. Cetina, F. Oručević, and V. Vuletić. Observation of cold collisions between trapped ions and trapped atoms. *Phys. Rev. Lett.*, 102:223201, 2009. 94

[109] W. Nörtershäuser, N. Trautmann, K. Wendt, and B.A. Bushaw. Isotope shifts and hyperfine structure in the $4s^2\,{}^1S_0 \rightarrow 4s4p\,{}^1P_1 \rightarrow 4s4d\,{}^1D_2$ transitions of stable calcium isotopes and calcium-41. *Spectro. Acta Part B*, 53:709, 1998. 97

[110] Y. Kasai and S. Sakai. Atomic absorption spectroscopy system for flux monitoring and atomic-layer control of molecular beam epitaxial growth of BiSrCaCuO. *Rev. Sci. Inst.*, 68:7, 1997. 110

[111] Stanford Research Systems. *Quartz Crystal Microbalance Theory and Calibration*. Stanford Research Systems, Inc., Sunnyvale, CA 94089, 2005. 110

[112] Anders Mortensen. *Aspects of Ion Coulomb Crystal based Quantum Memory for Light*. PhD Thesis, The University of Aarhus, 2005. 113

[113] H.J. Kimble. The quantum internet. *Nature*, 453:1023–1030, 2008. 114

[114] I. Bloch. Quantum coherence and entanglement with ultracold atoms in optical lattices. *Nature*, 453:1016–1022, 2008. 114

[115] Q.A. Turchette, C.S. Wood, B.E. King, C.J. Myatt, D. Leibfried, W.M. Itano, C. Monroe, and D.J. Wineland. Deterministic Entanglement of Two Trapped Ions. *Phys. Rev. Lett.*, 81:3636–3634, 1998. 114

[116] R. Blatt and D.J. Wineland. Entangled states of trapped atomic ions. *Nature*, 453:1008–1015, 2008. 114

[117] M. Riebe, K. Kim, P. Schindler, T. Monz, P.O. Schmidt, T.K. Körber, W. Hänsel, H. Häffner, C.F. Roos, and R. Blatt. Process Tomography of Ion Trap Quantum Gates. *Phys. Rev. Lett.*, 97:220407, 2006. 114

[118] K. Kim, M.-S. Chang, R. Islam, S. Korenblit, L.-M. Duan, and C. Monroe. Entanglement and Tunable Spin-Spin Couplings between Trapped Ions Using Multiple Transverse Modes. *Phys. Rev. Lett.*, 103:120502, 2009. 114

[119] M.J. Biercuk, H. Uys, J.W. Britton, A.P. VanDevender, and J.J. Bollinger. Phase-coherent detection of an optical dipole force by Doppler velocimetry. *Optics Express*, 19:10304–10316, 2011. 114

[120] S. Schlemmer, J. Illemann, S. Wellert, and D. Gerlich. Nondestructive high-resolution and absolute mass determination of single, charged particles in a three dimensional quadrupole trap. *J. Appl. Phys.*, 90:5410–8, 2001. 114

[121] G. Morigi, P.W.H. Pinkse, M. Kowalewski, and R. de Vivie-Riedle. Cavity Cooling of Internal Molecular Motion. *Phys. Rev. Lett.*, 99:073001, 2007. 128

Appendix A

Abbreviations

AOM: acousto-optic modulator

a.u.: arbitrary units

COM: centre-of-mass

cps: counts per second

DAQ: data acquisition device

EMCCD: electron multiplied charge coupled device

FFT: fast Fourier transform

kcps: kilo counts per second

PBS: polarisation beam splitter

PLA: pulsed laser ablation

PMT: photomultiplier tube

rf: radio frequency

SHG: second harmonic generation

SNR: signal-to-noise ratio

TDC: time-to-digital converter

TTL: transistor-transistor logic

UHV: ultra-high vacuum

VCO: voltage-controlled oscillator